Structural studies of two metallo-enzymes: methyl-coenzyme M reductase and hydroxylamine oxidoreductase

A DISSERTATION
SUBMITTED TO THE FACULTY OF THE GRADUATE SCHOOL
OF THE UNIVERSITY OF MINNESOTA
BY

Peder E. Cedervall

IN PARTIAL FULFILLMENT OF THE REQUIREMENTS
FOR THE DEGREE OF
DOCTOR OF PHILOSOPHY

Adviser: Dr. Carrie M. Wilmot

July 2012

Acknowledgements

First and foremost I would like to thank my adviser Dr. Carrie Wilmot for making this thesis possible and for all of her great support. I also appreciate the guidance and support from my thesis committee members. I would also like to thank past and present members of the Wilmot lab for making it such a great place to work. All of my studies where done in collaboration with other labs and I greatly appreciate the hard work of the collaborating graduate students and post-docs, and the great patience shown by the collaborating P.I.s. Many thanks goes to the members of the Lipscomb, Walters and Matsuo labs for lending me their equipment as well as their valuable time. I would also like to thank the beamline scientists at beamlines 14, 19 and 23 at the Advanced Photon Source for their assistance in X-ray diffraction data collection. I would also like to extend my gratitude to Ed Hoeffner at the Kahlert Structural Biology Laboratory and the personel at the Super Computing Institute, both at the University of Minnesota. Last but not least I would like to thank my friends and family for their support during my time in graduate school.

Dedication

I would like to dedicate this thesis to my parents and grandparents.

Abstract

The use of nickel by enzymes is unusual as evidenced by the fact that there are only eight nickel-based enzyme systems currently known, one of which is methyl-coenzyme M reductase (MCR). The site of catalysis in MCR is a highly reduced nickel-containing prosthetic group named coenzyme F_{430}. In the catalytic reaction of MCR, the substrates methyl-coenzyme M and coenzyme B are converted to methane and a heterodisulfide. Although MCR has been studied for decades, it is not clear how it carries out the difficult chemistry of methane formation. The length of the alkanoyl chain in coenzyme B is apparently important for enzymatic turnover. This thesis describes the X-ray crystallographic characterization of the MCR enzyme in complex with four different coenzyme B analogues. Structure analysis suggests why the coenzyme B analogues range from poor substrates to inhibitors. This thesis also describes a crystal structure of a putative catalytic intermediate of MCR with a methyl group bound to the nickel atom. This is the first crystal structure of MCR that resembles a proposed catalytic intermediate.

In contrast to nickel, iron is much more widely used in enzymatic systems. A common iron-containing prosthetic group is known as heme. The enzyme hydroxylamine oxidoreductase (HAO) contains 24 hemes and is therefore one of the most complex heme proteins known. The site of catalysis in HAO is a heme with unusual properties proposed to have a single covalent crosslink to a tyrosine residue of the protein. This thesis describes a HAO crystal structure that suggests a different model for this heme: an unprecedented double crosslink between the heme porphyrin and tyrosine. The crystal structure also revealed that HAO is complexed to a protein identified as a hypothetical protein of unknown function in the *Nitrosomonas europaea* genome. As the HAO sample was purified from *N. europaea* this interaction is likely of biological relevance. A crystal structure of HAO in complex with hydroxylamine substrate is also reported. The closing chapter of the thesis describes the cloning and transformation of the *N. europaea hao* gene into *Shewanella oneidensis* that potentially could support recombinant expression of HAO.

Table of Contents

List of Tables

List of Figures

List of Schemes

Chapter 1

Methyl-coenzyme M reductase

The contents of this chapter are reprinted (adapted) with permission from:

Cedervall, P. E., Dey, M., Pearson, A. R., Ragsdale, S. W., and Wilmot, C. M. (2010) "Structural insight into methyl-coenzyme M reductase chemistry using coenzyme B analogues", *Biochemistry 49*, 7683-7693.

Cedervall, P. E., Dey, M., Li, X., Sarangi, R., Hedman, B., Ragsdale, S. W., and Wilmot, C. M. (2011) "Structural analysis of a Ni-methyl species in methyl-coenzyme M reductase from *Methanothermobacter marburgensis*", *J. Am. Chem. Soc. 133*, 5626-5628.

1.1 Introduction

Enzymes often contain metal atoms required for activity, many of which are inserted into an organic prosthetic group prior to protein incorporation. The use of nickel by enzymes is unusual, and to date there are only eight Ni-based enzyme systems known (*1*). These systems are: glyoxylase I (Glx I), acireductone dioxygenase (ARD), Ni-superoxide dismutase (Ni-SOD), urease, Ni-Fe hydrogenase, carbon monoxide dehydrogenase (CODH), acetyl-coenzyme A synthase (ACS) and methyl-coenzyme M reductase (MCR). All but glyoxylase I catalyze a reaction that involves the use and/or production of gases central to the global carbon, nitrogen, and oxygen cycles in their catalysis (Table 1.1). Only trace amounts of soluble Ni^{2+} are present in the environment, signifying the requirement of a high affinity Ni uptake system(s) in the organisms that utilize Ni based enzymology. On the other hand, free Ni is harmful to the cell so a tightly coordinated array of chaperone-, sensor- and regulator proteins involved in Ni homeostasis are also essential. The MCR enzyme is found in the methanogenic archaea.

Table 1.1 Nickel containing enzyme systems

Enzyme	**Reaction**
Glx I	methylglyoxal → lactate + H_2O
ARD	1,2-dihydroxy-3-oxo-5-(methylthio)pent-1-ene + O_2 → 3HCOOH + methylthiopropionate + CO
Ni-SOD	$2H^+ + 2O_2 \rightarrow 3H_2O_2 + O_2$
Urease	$H_2N\text{-}CO\text{-}NH_2 + 2H_2O \rightarrow 2NH_3 + H_2CO_3$
Hydrogenase	$2H^+ + 2e^- \leftrightarrow H_2$
CODH	$2e^- + 2H^+ + CO_2 \leftrightarrow CO + H_2O$
ACS	$CH_3\text{-}CFeSP + CoASH + CO \rightarrow CH_3\text{-}CO\text{-}SCoA + CFeSP$
MCR	$CH_3\text{-}CoM + CoBSH \rightarrow CH_4 + CoM\text{-}SS\text{-}CoB$

Methanogenic archaea are organisms that under strict anaerobic conditions derive energy by reducing compounds, such as carbon dioxide, methylamine, acetate and methanol to methane (*2, 3*). This is the major source of methane produced in nature and the global production is estimated at one billion tons annually (*2*). Microbially produced methane is not only a potential source of renewable energy but also a potent greenhouse gas (20 times more potent than CO_2) and as such, study of this process has environmental ramifications. In these microorganisms MCR catalyzes the final step in methanogenesis, in which the substrates methyl-coenzyme M (methyl-SCoM, 2-(methylthio)ethanesulfonate) and coenzyme B (CoBSH, *N*-7-mercaptoheptanoylthreonine phosphate) are converted to methane and a heterodisulfide (CoBS-SCoM) (Scheme 1.1) (*4*).

Scheme 1.1 Reaction catalyzed by methyl-coenzyme M reductase.

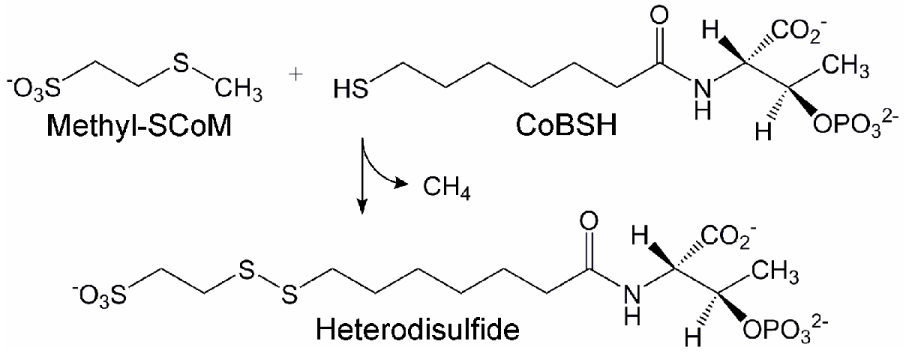

MCR is a 273 kDa protein with six subunits arranged in a $\alpha_2\beta_2\gamma_2$ oligomer (Figure 1.1A) (*5*). The known crystal structures show that MCR has two active sites approximately 50 Å apart that are deeply buried within the enzyme (*6-9*). Five of the

residues that outline the substrate channel are modified amino acids: 1-*N*-methylhistidine (α257), 5-(*S*)- methylarginine (α271), 2-(*S*)-methylglutamine (α400), *S*-methylcysteine (α452) and a glycine that has the peptide oxygen substituted with sulfur (α445). It has

Figure 1.1 MCR molecule, substrate channel and F_{430} drawing. (A) Cartoon representation of MCR $\alpha_2\beta_2\gamma_2$ molecule with one αβγ trimer colored in pale green (α), light blue (β) and light pink (γ) and the second αβγ trimer is colored in gray. (B) Active site and substrate channel in the $MCR_{ox1\text{-}silent}$ crystal structure (PDB ID 1HBN) (*9*). Coenzyme F_{430}, CoBSH and HSCoM are drawn as stick colored by atom (carbon: dark grey). The nickel is displayed as a green sphere and water as a red sphere. Interactions are drawn as dashed lines, and the corresponding distance is indicted in Angstroms (Å). The path of the substrate channel was defined in the absence of F_{430}, CoBSH, HSCoM and water, with the surface closest to the viewer cut away. (C) Drawing of cofactor F430.

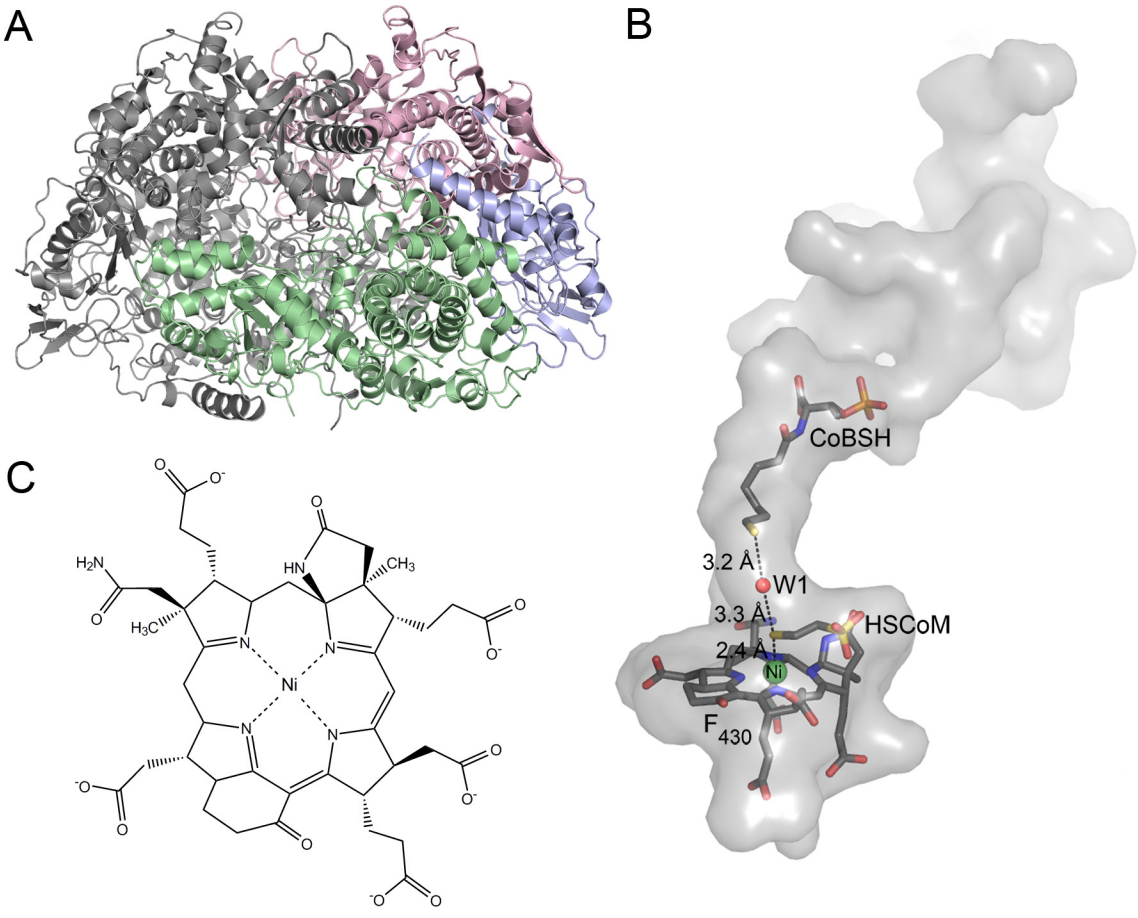

been shown that the four side chain methylations are derived from the methyl group of methionine, most likely via *S*-adenosylmethionine (*10*). The purpose of these modifications has yet to be determined. The active site pocket is comprised of residues from subunits α, α', β and γ, with a 30 Å long substrate channel leading to the enzyme surface (Figure 1.1B). At the heart of the active site pocket is coenzyme F_{430} (F_{430}), which is a highly reduced nickel-containing tetrapyrrole (Figure 1.1C) (*11-13*). Currently sixteen distinct enzymatic and complexed states of MCR have been spectroscopically characterized making this a challenging system to study (Scheme 1.2) (*14-35*). In the resting active state of the enzyme, denoted MCR_{red1}, the redox-active nickel of F_{430} is present in the Ni(I) state (*14, 21, 36*). MCR is extremely oxygen sensitive and upon oxygen exposure the enzyme enters an inactive Ni(II) state, denoted $MCR_{red1\text{-}silent}$ (*11*). In this state it cannot be converted back to the active Ni(I) form by any known reducing

Scheme 1.2 Scheme of the characterized forms of MCR.

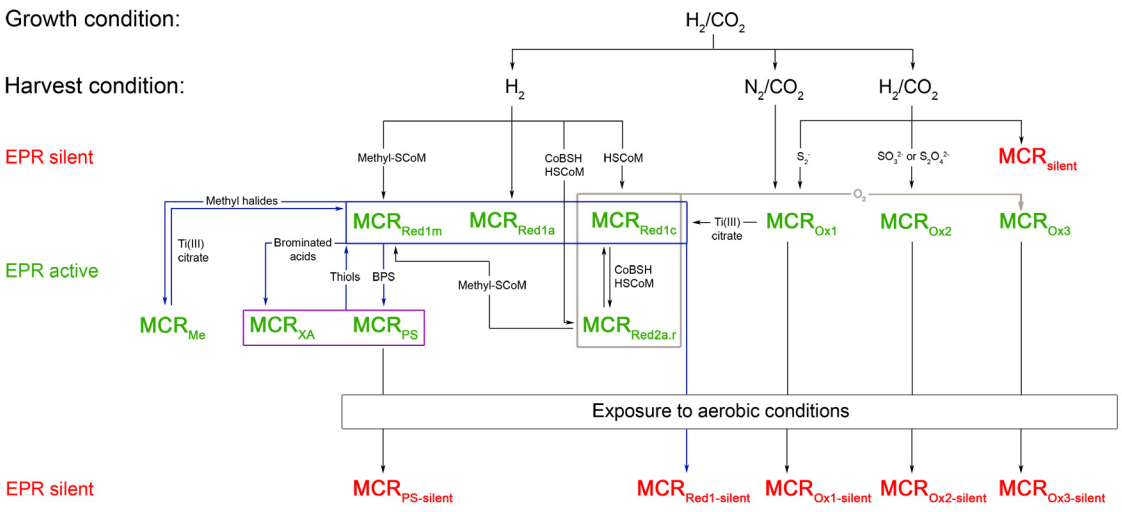

agent. This makes studying the MCR mechanism experimentally difficult, with the additional complication that kinetic and X-ray crystallographic studies demonstrate that purified MCR has coenzyme-derived species already bound to the enzyme that are difficult to displace (*6-9*).

Despite the fact that MCR has been studied for decades, no true catalytic intermediate has been observed, and the actual mechanism remains elusive. Currently three general mechanistic schemes for the enzymatic reaction have been proposed, each of which posit different chemistry to initiate catalysis. In mechanism I, Ni(I) acts as a nucleophile and attacks the methyl carbon of methyl-SCoM in an S_N2-type reaction, which generates a methyl-Ni(III) and HSCoM (Scheme 1.3A) (*9, 37-39*). The methyl-Ni(III) accepts an electron from HSCoM to generate methyl-Ni(II), which undergoes protonation and cleavage to generate methane. The resulting $^{\bullet}$SCoM radical combines with $CoBS^{-}$ to form a disulfide radical anion. This highly reducing species, donates an electron to Ni(II) to regenerate the active Ni(I) resting state and the heterodisulfide product, CoBS-SCoM. A stable MCR-Ni(III)-methyl (MCR_{Me}) state can be artificially produced by treating MCR_{red1} with methyl halide (*16, 31*). In support of mechanism I, treatment of methyl halide produced MCR_{Me} with HSCoM generates MCR_{red1} along with the substrate methyl-SCoM (reverse of step 1 in mechanism I). The geometric and electronic structure of MCR_{Me} was recently characterized in solution by X-ray absorption spectroscopy (XAS) and density functional theory (DFT) (*28*). In mechanism II, CoBSH does not directly participate in the first step of the reaction, where it is proposed that Ni(I) attacks at the sulfur atom of methyl-SCoM to generate a methyl radical and a Ni(II)-

SCoM species (Scheme 1.3B) (*40-42*). Hydrogen atom abstraction from CoBSH by the methyl radical generates methane and a thiyl radical, $CoBS^{\bullet}$, which combines with the Ni(II)-SCoM species to generate the disulfide radical anion as in mechanism I, which donates an electron to Ni(II) to regenerate Ni(I) and CoBS-SCoM. A more recently proposed mechanism III suggests protonation of F_{430} promotes reductive cleavage of the methyl-SCoM thioether bond (*43*).

Scheme 1.3 Two of the proposed catalytic mechanisms for methyl-coenzyme M reductase. (A) mechanism I and (B) mechanism II.

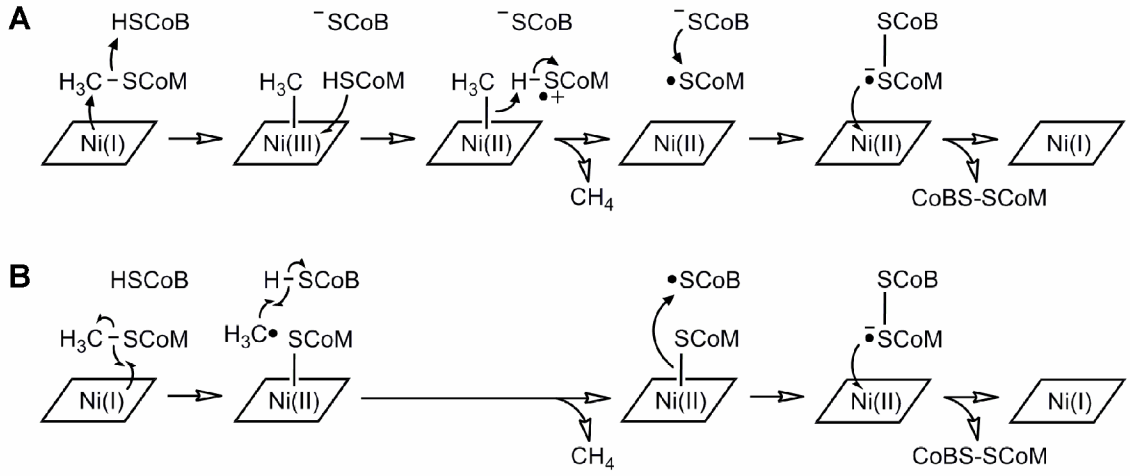

Due to the stringent requirement to exclude dioxygen (O_2), the available MCR crystal structures are all in the inactive Ni(II) state. All but one contain CoBSH and HSCoM (demethylated methyl-SCoM, an inhibitor and substrate analogue) in the active site ($MCR_{ox1\text{-}silent}$ and $MCR_{red1\text{-}silent}$, PDB IDs 1HBN, 1HBO, 1HBU, 1E6Y and 1E6V, Scheme 1.2) (*6-8*). The final crystal structure contains the heterodisulfide product, CoBS-SCoM (MCR_{silent}, PDB ID 1HBM, Scheme 1.1 and 1.2) (*6, 7*). All these structures

reveal that both substrates access the active site through the same channel (Figure 1B). The binding site of HSCoM (and presumably methyl-SCoM) is more deeply buried within the enzyme, and so it must enter prior to CoBSH for productive chemistry to occur. As binding of CoBSH in the absence of co-substrate would be inhibitory, it was suggested that a conformational change upon methyl-SCoM binding might lower the K_d for CoBSH, and thus promote an ordered mechanism. Perplexingly, the sulfur of the CoBSH substrate is 8.8 Å from the Ni(II) in the $MCR_{ox1\text{-}silent}$ and the $MCR_{red1\text{-}silent}$ crystal structures, and 6.4 Å from the thiol of the inhibitor HSCoM (Figure 1.1) (*6, 7*). Therefore, a conformational change has been postulated that would enable CoBSH to penetrate deeper into the substrate channel, and thus approach closer to any nickel-bound species. The heterodisulfide product in the MCR_{silent} crystal structure has the CoBSH portion in virtually the same place as in $MCR_{ox1\text{-}silent}$, giving no clue to possible structural changes that might occur to facilitate CoBSH reacting with nickel-associated intermediates (*6, 7*).

To investigate the structural role of the number of carbon atoms in the alkanoyl moiety of CoBSH, we have solved the X-ray crystal structures of MCR in complex with four different CoBSH analogues (Chapter 1.2). CoBSH has a heptanoyl moiety linked to the thiol group, and the analogues are pentanoyl-, hexanoyl-, octanoyl- or nonanoyl-containing derivatives of CoBSH (CoB_5SH, CoB_6SH, CoB_8SH and CoB_9SH respectively) (Figure 1.2) (*4, 9, 44-48*). In addition, we present a structure in complex with the heterodisulfide product and a structure in which the substrate channel predominantly lacks either CoBSH or heterodisulfide. This thesis also describes a crystal

structure of a MCR reacted with methyl iodide. The goal of this study was to generate the first crystal structure of a putative catalytic intermediate: MCR with a methyl group bound to the F_{430} nickel atom (Chapter 1.3).

Figure 1.2 Drawing of CoBSH analogues. (A) *N*-5-mercaptopentanoylthreonine phosphate (CoB_5SH), (B) *N*-6-mercaptohexanoylthreonine phosphate (CoB_6SH), (C) *N*-8-mercaptooctanoylthreonine phosphate (CoB_8SH), (D) *N*-9-mercaptononanoylthreonine phosphate (CoB_9SH).

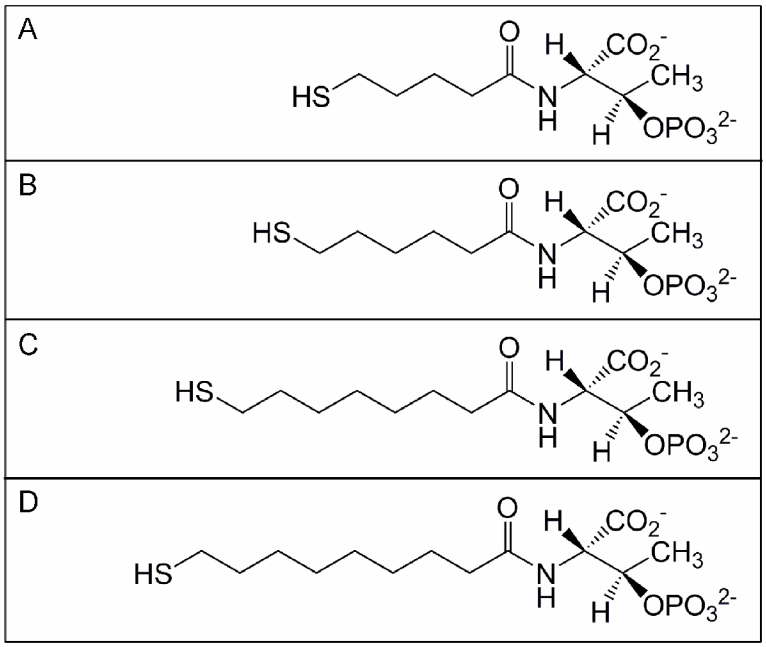

1.2 Structural insight into methyl-coenzyme M reductase chemistry using coenzyme B analogues

Methyl-coenzyme M reductase (MCR) catalyzes the final and rate-limiting step in methane biogenesis: the reduction of methyl-coenzyme M (methyl-SCoM) by coenzyme B (CoBSH) to methane and a heterodisulfide (CoBS-SCoM). Crystallographic studies show that the active site is deeply buried within the enzyme, and contains a highly reduced nickel-tetrapyrrole, coenzyme F_{430} (F_{430}). Methyl-SCoM must enter the active site prior to CoBSH, as methyl-SCoM reacts with the F_{430} nickel in the deepest part of the 30 Å long substrate channel that leads from the protein surface to the active site. The seven-carbon mercaptoalkanoyl chain of CoBSH binds within a 16 Å predominantly hydrophobic part of the channel, with the CoBSH thiolate lying closest to the nickel at a distance of 8.8 Å. It has been suggested that binding of CoBSH initiates catalysis by inducing a conformational change. In order to better understand the structural role of CoBSH early in the MCR mechanism, we have determined crystal structures of MCR in complex with four different CoBSH analogues: pentanoyl-, hexanoyl-, octanoyl- and nonanoyl- derivatives of CoBSH (CoB_5SH, CoB_6SH, CoB_8SH and CoB_9SH respectively). The data presented here reveal that the shorter CoB_5SH mercaptoalkanoyl chain overlays with that of CoBSH, but terminates two units short of the CoBSH thiolate position. In contrast, the mercaptoalkanoyl chain of CoB_6SH adopts a different conformation, such that its thiolate is coincident with the position of the CoBSH thiolate. This is consistent with the observation that CoB_6SH is a slow substrate. A labile water in

the substrate channel was found to be a sensitive indicator for the presence of CoBSH and HSCoM. The longer CoB_8SH and CoB_9SH analogues can be accommodated in the active site through exclusion of this water. The CoB_8SH thiolate is 2.6 Å closer to the nickel than that of CoBSH, but the additional carbon of CoB_9SH only decreases the nickel thiolate distance a further 0.3 Å. Although the analogues do not induce any structural changes in the substrate channel, the thiolates appear to preferentially bind at two distinct positions in the channel, one being the previously observed CoBSH thiolate position and the other being at a hydrophobic annulus of residues that lines the channel proximal to the nickel.

1.2.1 Methods

Materials. The organism *Methanothemobacter marburgensis* (catalog OCM82) was obtained from the Oregon Collection of Methanogens. All buffers and media reagents were obtained from Sigma-Aldrich. The gases N_2 (99.98%), H_2/CO_2 (80%/20%), and ultra high purity H_2 (99.999%) were obtained from Cryogenic Gases. Titanium (III) citrate solutions were prepared from a stock solution of 246 mM Ti(III) citrate, which was synthesized by adding sodium citrate to Ti(III) trichloride (30 wt % solution in 2 N hydrochloric acid) (Acros Organics) under anaerobic conditions and adjusting pH to 7.0 with sodium bicarbonate (*49*). The concentration of Ti(III) citrate was determined by titrating against a solution of methyl viologen.

Synthesis of methyl-SCoM, CoB_5SH, CoB_6SH, CoBSH, CoB_8SH, and CoB_9SH. Methyl-SCoM was prepared from HSCoM and methyl iodide (*50*). The homodisulfides, CoB_5S-$SCoB_5$, CoB_6S-$SCoB_6$, CoBS-SCoB, CoB_8S-$SCoB_8$, CoB_9S-$SCoB_9$ were prepared as described from 5-bromovaleric acid, 6-bromohexanoic acid (Sigma-Aldrich), 7-bromoheptanoic acid (Karl Industries), 8-bromooctanoic acid, and 9-bromononanoic acid (Matrix Scientific), respectively (*44, 47*). The free thiol forms of CoB_5SH, CoB_6SH, CoBSH, CoB_8SH, and CoB_9SH were generated by the reduction of the homodisulfides as previously described (*46*). The purity of the CoBSH analogues was determined by ^1H nuclear magnetic resonance (NMR) spectroscopy. All compounds synthesized were stored in a Vacuum Atmospheres chamber maintained at a dioxygen level below 1 ppm,

as monitored continually with an oxygen analyzer (model 317, Teledyne Analytical Instruments) until use.

M. marburgensis growth and MCR_{red1} purification. Buffer preparations and all manipulations were performed under strict anaerobic conditions in a Vacuum Atmospheres chamber maintained at a dioxygen level below 1 ppm, as monitored continually with an oxygen analyzer (model 317, Teledyne Analytical Instruments). MCR_{red1} was isolated from *M. marburgensis* cultured on H_2/CO_2 (80%/20%) at 65°C in a 14 L fermentor (New Brunswick Scientific Co). Culture media were prepared as previously described (*25, 28*). MCR_{red1} was generated *in vivo* and purified as described previously (*25*). The purification procedure routinely generates 65-75% MCR_{red1} as determined by UV-visible absorption and electron paramagnetic resonance (EPR) spectroscopy.

Spectroscopy of MCR. UV-visible absorption spectra of the Ni(I)-containing MCR_{red1} were recorded in the anaerobic chamber using a spectrophotometer (Model USB4000-UV-VIS). EPR spectra were recorded on a Bruker EMX spectrometer (Bruker Biospin Corp.), equipped with an Oxford ITC4 temperature controller, a Hewlett-Packard Model 5340 automatic frequency counter and Bruker gaussmeter. The EPR spectroscopic parameters included: temperature, 70°K; microwave power, 10 mW; microwave frequency, 9.43 GHz; receiver gain, 2×10^4; modulation amplitude, 10.0 G; modulation frequency, 100 kHz. Double integrations of the EPR spectra were performed and

referenced to a 1 mM copper perchlorate standard. The NMR data were acquired at 298°K on a Bruker Avance DRX 500 MHz instrument equipped with a TXI cryoprobe.

Preparation of MCR_{red1} for crystallization. All crystallization experiments were performed in the anaerobic chamber in which *M. marburgensis* was grown and MCR purified unless otherwise noted. MCR_{red1} was prepared in 50 mM Tris pH 7.6 and excess HSCoM was removed by buffer exchange using an Amicon Ultra centrifuge filter with a 50 kDa cut-off membrane (Millipore). Typically, 2-3 ml of MCR_{red1} was exchanged with 10-15 ml of 50 mM Tris pH 7.6. The enzyme was concentrated to 500-600 µl, and this process was repeated three times. The fraction of MCR_{red1} in the purified MCR sample was calculated from the UV-visible absorption spectrum using extinction coefficients of 27.0 mM^{-1} cm^{-1} at 385 nm for Ni(I)-MCR_{red1}, and 9.15 mM^{-1} cm^{-1} at 420 nm for Ni(II)-$MCR_{red1\text{-}silent}$ (*25*). The amount of MCR_{red1} in the sample used for crystallization was determined to be ~80% and the concentration of total enzyme used was in the range of about 120-150 µM (32-40 mg/ml). All crystallization experiments were performed anaerobically by incubating 2 µl of enzyme solution in 50 mM Tris pH 7.5 and 2 µl of reservoir solution (100 mM Hepes-Na pH 7.3/7.5/8.0, 150 mM magnesium acetate ($Mg(CH_3COO)_2$), 20/22% (w/v) PEG 400) in a sitting drop over 1 ml reservoir solution at 9ºC. Triangular and rectangular prismatic crystals with a bright yellowish green color confirmed the presence of nickel coenzyme F_{430}. The crystals grew to a size of approximately 0.1-0.2 mm in 4-5 days. CoBSH-depleted crystal was obtained by incubating 2 µl of a reaction mixture containing 139 µM MCR_{red1} and 13 mM HSCoM

with 2 µl of reservoir solution (100 mM Hepes-Na pH 7.5, 150 mM $Mg(CH_3COO)_2$, 22% PEG 400). Crystals of MCR complexed with the CoBSH analogues were grown by co-crystallization. The CoB_5SH co-crystal was obtained by incubating 2 µl enzyme solution containing 124 µM MCR_{red1}, 10 mM methyl-SCoM and 1 mM CoB_5SH with 2 µl of reservoir solution (100 mM Hepes-Na pH 7.5, 150 mM $Mg(CH_3COO)_2$, 22 % PEG 400). The crystals with bound CoB_6SH and CoB_9SH were obtained by co-crystallization of 1 mM of analogue with 142 µM MCR_{red1} and equilibrated with 2 µl of reservoir solution (100 mM Hepes-Na pH 7.5, 150 mM $Mg(CH_3COO)_2$, 20 % PEG 400 for CoB_6SH and 100 mM Hepes-Na pH 7.3, 150 mM $Mg(CH_3COO)_2$, 22 % PEG 400 for CoB_9SH). The product complex crystal was obtained through co-crystallization of 2 µl enzyme solution containing 124 µM MCR_{red1}, 10 mM methyl-SCoM and 0.93 mM CoBSH incubated with 2 µl of reservoir solution (100 mM Hepes-Na pH 7.5, 150 mM $Mg(CH_3COO)_2$, 22 % PEG 400). Crystals were cryoprotected in reservoir solution containing 25 % (v/v) PEG 400 by soaking for 2-5 minutes before flash frozen in liquid nitrogen in the anaerobic chamber. Crystal with CoB_8SH bound to MCR was obtained by incubating 2 µl of a mixture of 119 µM MCR_{red1} and 1 mM CoB_8SH with 2 µl of reservoir solution (100 mM Hepes-Na pH 7.3, 150 mM $Mg(CH_3COO)_2$, 20 % PEG 400). Before cryoprotection, the crystal was soaked for 5-10 minutes in a 100 mM solution of methyl iodide[1]. The methyl iodide solution used for soaking was prepared by adding a concentrated stock of methanolic solution of methyl iodide to the reservoir solution. The soaked crystal was

[1] Methyl iodide was added with the intention of creating a Ni(III)-methyl species. This was not achieved, but the diffraction quality of this crystal was significantly better than crystals co-crystallized with CoB_8SH alone, and so has been included in this study.

quickly cryoprotected as described above and flash frozen in liquid nitrogen in the anaerobic chamber.

X-ray diffraction data collection, processing and refinement. X-ray diffraction data were collected at 100°K on a ADSC Quantum-315 detector at beamline 14-BM-C (BioCARS) at the Advanced Photon Source, Argonne National Laboratory. The wavelength of X-rays was 0.979 Å. Data were processed using HKL2000 (*51*). As in the previous X-ray crystallographic studies, the crystals belong to the monoclinic space group $P2_1$ (a = 82 Å, b = 118 Å , c = 122 Å, β = 92°), with one MCR molecule (two active sites) per asymmetric unit (ASU) (*6, 7*). For refinement, REFMAC in the Collaborative Computational Project Number 4 (CCP4) program suite was used (*52*). A random sample of 5 % of the data across all resolution shells was chosen to check refinement progress through calculation of an R_{free}. The same reflections were used to calculate R_{free} for all structures, thus preventing bias due to high structural identity. The remaining reflections were used in refinement (R_{work}). Model building was done using the Crystallographic Object-Oriented Toolkit (COOT) (*53*). The diffraction data and their models are designated as MCR_{CoBXSH}, where *X* is the number of carbons in the alkanoyl portion of the analogue. The data and model of MCR in complex with heterodisulfide product is designated $MCR_{CoBSH + methyl\text{-}SCoM}$. Library files in CCP4 for F_{430}, CoBSH and heterodisulfide were incorrect, and these were modified in Monomer Library Sketcher in the CCP4 program suite by comparison with schematic drawings from Grabarse *et al*. (*7*). Coordinate and CCP4 library files for the different CoBSH analogues were created in

Monomer Library Sketcher. The general model building and refinement strategy for all structures was as follows. It was clear from the electron density in the substrate channel and at the active site that mixtures of species were present in all datasets. These could be visualized with Fo-Fc and Fo-Fo difference electron density maps (Figure 1.3). The known positions of CoBSH, HSCoM and heterodisulfide product from the published Ni(II)-MCR crystal structures (PDB IDs 1HBN, 1HBO, 1HBU and 1HBM (*7*)) were used

Figure 1.3 Example using the MCR_{CoB8SH} data to show how the Fo-Fc difference electron density map was used to elucidate the occupancy of CoBSH and the analogue. (A) Initial map before refinement fits well with CoB_8SH. (B) Positive and negative Fo-Fc difference electron density peaks after refinement with 100 % CoB_8SH as a model. (C) In final model with 50% CoB_8SH and 50% CoBSH there is no Fo-Fc difference electron density present at a contour of 4σ. 2Fo-Fc electron density map (contoured at 1σ) is shown as a blue mesh. Positive and negative peaks in the Fo-Fc difference electron density map (contoured at 4σ) are shown as a green and red mesh, respectively. The protein is drawn as cartoon. Coenzyme F_{430}, HSCoM, CoB_8SH and CoBSH are drawn as stick and colored by atom (carbon: F_{430}, dark grey; HSCoM, medium grey; CoB_8SH, light blue; CoBSH, pale green). The nickel is displayed as a green sphere.

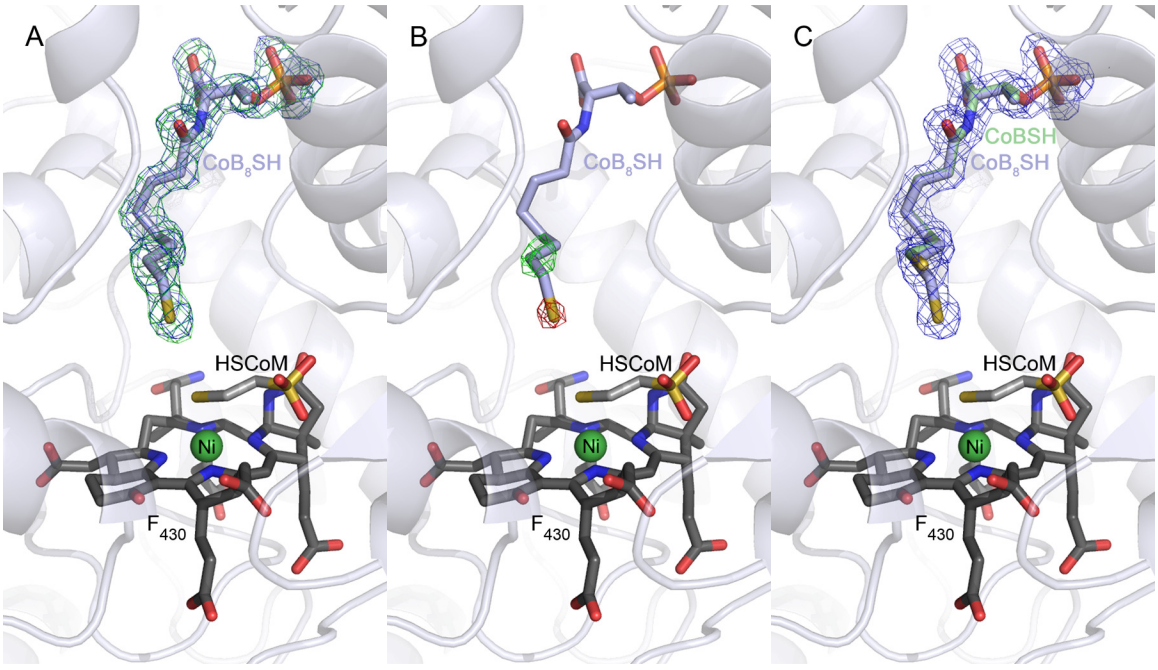

as guides to determine which species could be present in each data set, and these were then simultaneously modeled into the electron density. By alteration of their relative occupancies followed by refinement, the ratio of occupancy between different species was determined using the assumption that the average B-factors for all molecular species bound should be similar to that of F_{430} and adjacent well-ordered protein atoms within the active site and substrate channel. The combinations of modeled ligands were constantly reassessed throughout refinement based on the remaining difference electron density. This included test refinements of different ligand combinations during the latter stages, thus using the optimized phases to check whether a different combination of ligands could also explain the electron density. Sensible chemical structures and interactions, along with keeping the combined occupancies of sterically mutually exclusive species ≤100%, were maintained throughout refinement. The model was finally accepted when the difference electron density map was minimal and the B-factors for the models converged.

The first structure refined was that of MCR_{CoB5SH}. Initial phases were generated by difference Fourier using a previously determined crystal structure (PDB ID 1MRO (*6*)) but with all non-bonded molecules, except F_{430}, removed from the model. Initial rigid body refinement followed by restrained refinement of MCR_{CoB5SH} reduced the R_{work} to 26.5%. After model building and subsequent rounds of restrained refinement the R_{work} was 14.3% (R_{free} 16.6%). Of the five structures only the CoB_5SH analogue is completely coincident with CoBSH, and so particular care had to be used in teasing apart the ratios of the two species in modeling the MCR_{CoB5SH} electron density. This was done by

initially refining 100% CoBSH in the substrate channel. Positive Fo-Fc difference density located at the carbon where the shorter CoB_5SH thiol might be expected to sit indicated the presence of a more electron-rich atom than carbon, which is consistent with the presence of the CoB_5SH sulfur. The refinement converged at a model containing a 50/50 mix of CoBSH and the analogue. However, positive Fo-Fc difference density was still present at the position of the CoBSH thiol, therefore a water molecule was added to the CoB_5SH model at 50% occupancy and upon refinement this accounted for the electron density. An illustration of the electron density quality from this structure is shown in Figure 1.4. An HSCoM-, CoBSH- and CoBSH-analogue-free version of the refined MCR_{CoB5SH} structure was used as the starting model to generate initial phases for the five other structures. After the initial round of restrained refinement the R_{work} for

Figure 1.4 Stereo image of 2Fo-Fc electron density quality for the MCR_{CoB5SH} data. 2Fo-Fc electron density (contoured at 1σ) is shown as a mesh, colored green (F_{430}), red (HSCoM) and blue (amino acids). Models are drawn as stick and colored by atom (carbon: F_{430}, dark grey; HSCoM, medium grey; amino acids, white). The nickel is displayed as a green sphere.

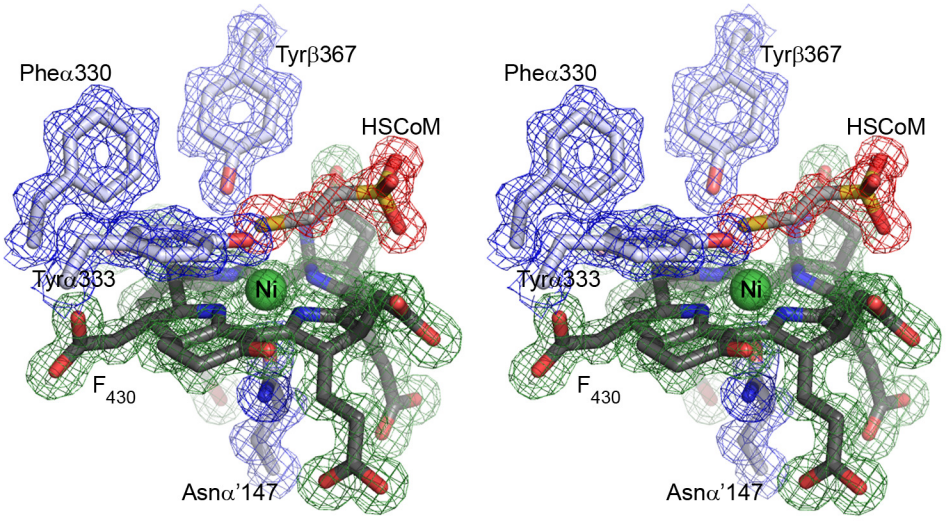

these structures were reduced to 14.5-15.6%.

Single crystal UV-visible microspectrophotometry. Data were collected on a microspectrophotometer from 4DX Systems AB, with a Zeiss CLX500 xenon lamp light source, spectrograph (Thermo-Oriel) and a DV401A CCD detector (Andor Technology). For the photoreduction studies spectra were collected off-line at the synchrotron beamline following X-ray data collection, i.e. the microspectrophotometer was set up adjacent to the beamline rather than integrated into the X-ray data collection hardware. An Oxford Instruments Cryojet was used for crystals at 100°K, and those at room temperature were mounted in quartz capillaries (*54*). For crystals used in structure determination, the UV-visible spectra were collected in the Kahlert Structural Biology Laboratory, University of Minnesota, after returning from X-ray diffraction data collection at the synchrotron. An Oxford Instruments Cryojet set to 100°K was used cool the mounted crystal.

X-ray photoreduction. In a separate set of experiments, crystals in the Ni(II)-MCR_{silent} (Scheme 1.2) state were subjected to X-ray irradiation at beamline 14-ID-B (BioCARS) at the Advanced Photon Source, Argonne National Laboratory. The Ni(II)-MCR_{silent} crystals were obtained by sitting drop vapor diffusion anaerobically at 4ºC by using the crystallization conditions described above. For comparative single crystal UV-visible microspectrophotometry, green Ni(I)-MCR_{red1} crystals were moved out of the anaerobic chamber and exposed to oxygen. The change in color to yellow confirmed formation of the Ni(II) state in the crystals, and the crystals were cryoprotected in reservoir solution

containing 25% (v/v) PEG 400 by soaking for 2-5 minutes before flash freezing in liquid nitrogen in the anaerobic chamber.

Each crystal was irradiated for 1 minute, then a further 4 minutes and then a further 5 minutes (total 10 minutes), and single crystal UV-visible absorption spectra recorded at each of these timepoints. Crystals were subjected to three different conditions: (1) room temperature and (2) 100°K, both with wavelength of 1.608 Å (7.709 keV) and (3) room temperature at the Ni K-edge (8.33 keV, 1.489 Å).

1.2.2 Results and Discussion

Six crystal structures were determined, four of which are in complex with CoBSH analogues differing in the number of carbons atoms in the alkanoyl portion of the molecule. CoBSH is an *N*-7-mercaptoheptanoyl-containing molecule, whereas the four CoBSH analogues contain *N*-5-mercaptopentanoyl-, *N*-6-mercaptohexanoyl-, *N*-8-mercaptooctanoyl- or *N*-9-mercaptononanoyl-moieties (Figure 1.2). The corresponding crystal structures are designated as $MCR_{CoB\mathit{X}SH}$, where *X* is the number of carbons in the alkanoyl portion of the analogue. The other crystal structures are of $MCR_{red1c\text{-}silent}$ (MCR in the Ni(II) state in complex with HSCoM, designated here as MCR_{HSCoM}) that is CoBSH-depleted, and of MCR_{silent} in complex with the heterodisulfide product (designated here as $MCR_{CoBSH + methyl\text{-}SCoM}$). The data sets have resolutions in the range from 1.3-1.8 Å. Overall, the resulting structures are very similar to each other and to the previously published structures of MCR, with differences mainly localized to the active site and substrate channel. The two active sites in the ASU were refined independently. Unless otherwise stated, there was no difference between them. All six datasets contain a mixture of species bound to the enzyme. There is always a background of CoBSH and HSCoM, which co-purify with MCR and cannot be fully removed by extensive buffer exchange or by the addition of a CoBSH analogue. HSCoM is added during purification of MCR, as it stabilizes the resting active Ni(I) state (unpublished data), and this leads to HSCoM occupancies between 50-100% amongst the structures (Table 1.2). In contrast CoBSH which is not added during purification has occupancies ranging from 30-50%.

As these confounding species have all been described at high occupancy in other crystallographic studies, the structural data of interest could be isolated (*6, 7, 55*). In each case, the additional electron density could be explained by inclusion of the appropriate CoB_XSH model used in that experiment, water molecules or heterodisulfide at 50% or higher occupancy. The resulting models, along with 2Fo-Fc electron density, are shown in Figure 1.5. The R_{work} for the final structures range from 13.0 to 15.0% (R_{free} 15.5 to 19.5%). The X-ray data collection, processing, refinement and model building statistics are given in Table 1.2.

By double integration of the EPR spectra, the MCR samples used for crystallization were determined to be ~78% MCR_{red1} (data not shown), which matched that determined by UV-visible absorption spectroscopy. At the time the MCR crystals were mounted for X-ray data collection and cryocooled in liquid nitrogen in the anaerobic chamber, their color (as assessed by eye) still appeared green, suggesting that a significant proportion of the Ni(I)-MCR_{red1} state remained. Furthermore, MCR samples were incubated in EPR tubes under conditions identical to those used for crystallization and then frozen at the time the crystals were mounted. EPR spectroscopy demonstrated that only 10-20% of the spin had been lost during the time of crystallization (data not shown). However, by the time crystals were transferred to the goniometer at the synchrotron prior to X-ray diffraction data collection they appeared yellow, suggesting that a significant conversion of Ni(I) to the inactive Ni(II) state had occurred during the course of storage, transport and transfer. This was confirmed following X-ray data collection by single crystal UV-visible microspectrophotometry. The post-X-ray UV-

Figure 1.5 The active sites and substrate channels of the MCR crystal structures. (A) $MCR_{CoBSH + methyl\text{-}SCoM}$ (B) MCR_{CoB5SH}, (C) MCR_{CoB6SH}, (D) MCR_{HSCoM}, (E) MCR_{CoB8SH} and (F) MCR_{CoB9SH}. 2Fo-Fc electron density map (contoured at 1σ) is shown as a blue mesh. The protein is drawn as cartoon. Heterodisulfide, CoB_XSH and acetate are drawn as stick and colored by atom (carbon: heterodisulfide, purple; CoB_5SH, orange; CoB_6SH, pale yellow; CoB_8SH, light blue; CoB_9SH, magenta; acetate, white). Coenzyme F_{430} and HSCoM are drawn as stick colored by atom (carbon: F_{430}, dark grey; HSCoM, medium grey). The nickel is displayed as a green sphere and water molecules as red spheres.

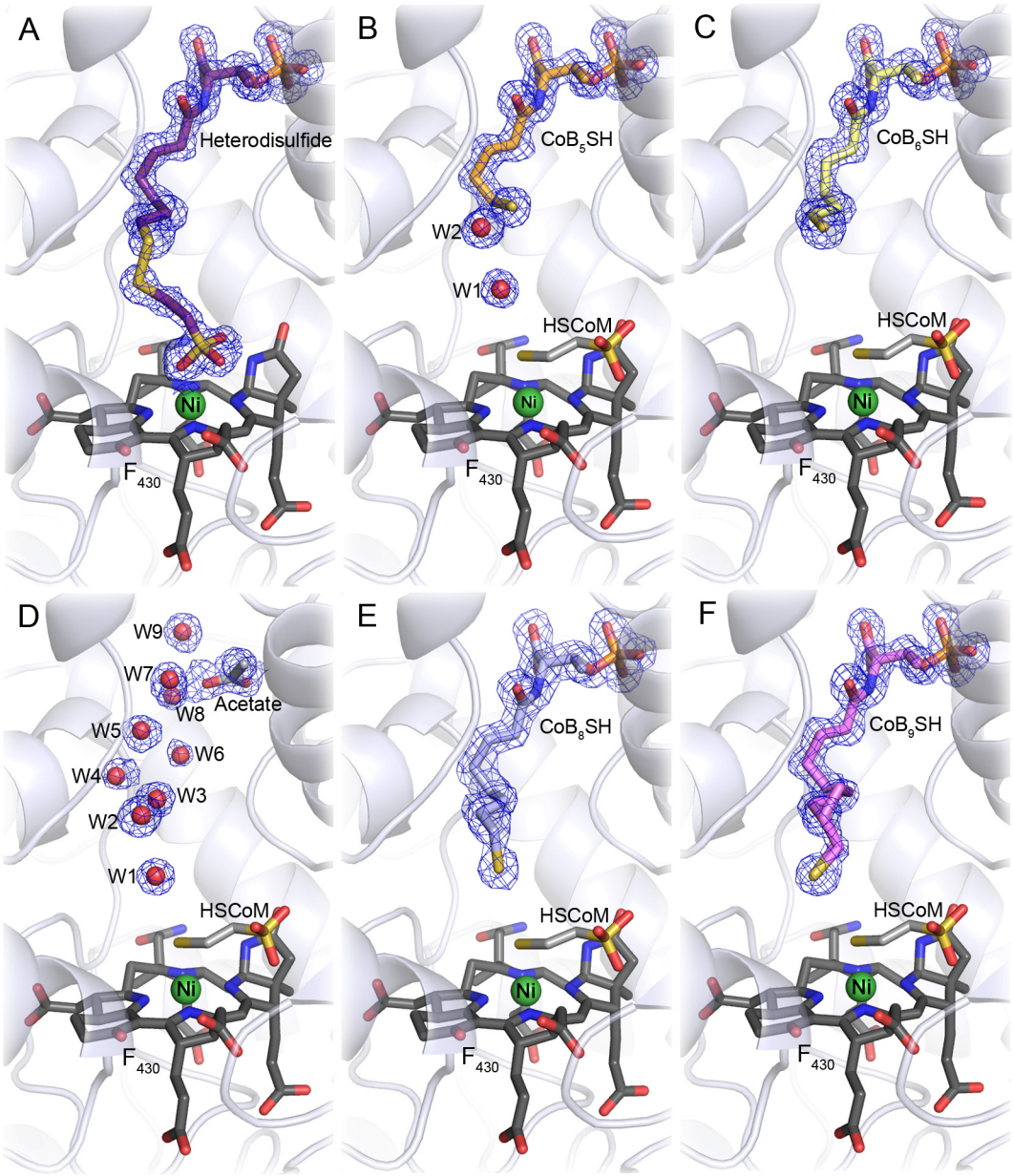

Table 1.2 X-ray diffraction data collection, processing and refinement statistics (part 1)

Data collection and processing statistics			
name of data set	$MCR_{CoBSH+methyl-CoM}$	MCR_{CoB5SH}	MCR_{CoB6SH}
measured reflections	2443766	1969388	2427498
unique reflections	474767	553755	446253
resolution (Å) [a]	50.0-1.35 (1.40-1.35)	50.0-1.30 (1.35-1.30)	50.0-1.40 (1.45-1.40)
completeness (%) [a]	93.2 (81.2)	97.1 (78.1)	99.9 (100.0)
R_{merge} (%) [a, b]	6.3 (27.6)	5.5 (32.9)	7.3 (44.7)
I/σI [a]	21.1 (5.5)	22.3 (3.6)	20.4 (4.0)
space group	$P2_1$	$P2_1$	$P2_1$
Refinement and model building statistics			
resolution (Å) [a]	20.28-1.35 (1.38-1.35)	20.49-1.30 (1.33-1.30)	19.89-1.40 (1.44-1.40)
no. of reflections in working set [a]	450864 (24362)	525817 (30239)	423854 (25833)
no. of reflections in test set [a]	23861 (1353)	27777 (1576)	22348 (1331)
R_{work} (%) [c]	14.0	14.3	13.0
R_{work} (%) [d]	15.7	16.6	15.5
ESU (Å) R_{work}/R_{free}	0.049/0.049	0.044/0.046	0.049/0.051
no. protein atoms	19913	20087	19960
no. coenzyme atoms	236	218	220
no. ligand atoms	41	37	62
no. water molecules	2475	2443	2352
RMS			
bond length (Å)	0.034	0.033	0.033
bond angle (deg.)	2.775	2.693	2.625
Ramachandran plot (%)			
favored	97.8	97.8	97.5
allowed	2.1	2.1	2.4
disallowed	0.1	0.1	0.1
average B-factor ($Å^2$)			
protein	13.2	12.4	13.4
coenzyme	8.3	8.2	9.2
ligands	32.5	32.0	35.4
waters	24.1	23.0	24.9
overall	14.4	13.5	14.6
occupancy per active site of HSCoM (%) [e]	50/50	90/90	50/50
occupancy per active site of CoBSH (%) [e]	50/50	50/50	50/50
CoBSH analogue, occupancy per active site (%) [e]		CoB_5SH, 50/50	CoB_6SH, 50/50
other molecule, occupancy per active site (%) [e]	heterodisulfide, 50/50		

[a] Values in parentheses correspond to the highest resolution shell.

[b] $R_{merge} = \Sigma_{hkl}\Sigma^{N}_{j=1}|I_{hkl}-I_{hkl}(j)|/\Sigma_{hkl}N*I_{hkl}$, sum over all reflections and all observations N, with $I_{hkl}(j)$ intensity of the j^{th} observation of reflection hkl and I_{hkl} mean intensity of the reflection hkl.

[c] $R_{work} = \Sigma||F_o| - |F_c||/ \Sigma|F_o|$, where $|F_o|$ = observed structure factor amplitude and $|F_c|$ = calculated structure factor amplitude.

[d] R_{free}, R-factor based on 5% of the data excluded from refinement.

[e] Occupancy of model in each of the two crystallographically independent active sites in the ASU

Table 1.2 X-ray diffraction data collection, processing and refinement statistics (part 2)

Data collection and processing statistics			
name of data set	MCR_{HSCoM}	MCR_{CoB8SH}	MCR_{CoB9SH}
measured reflections	1440665	1160543	1425506
unique reflections	405349	211803	401701
resolution (Å) [a]	50.0-1.45 (1.50-1.45)	50.0-1.80 (1.86-1.80)	50.0-1.45 (1.50-1.45)
completeness (%) [a]	99.5 (99.7)	99.8 (100.0)	98.1 (95.4)
R_{merge} (%) [a, b]	6.2 (44.0)	8.4 (47.7)	5.6 (42.5)
I/σI [a]	20.2 (3.2)	21.8 (3.9)	24.3 (3.2)
space group	$P2_1$	$P2_1$	$P2_1$
Refinement and model building statistics			
resolution (Å) [a]	20.15-1.45 (1.49-1.45)	19.93-1.80 (1.84-1.80)	20.07-1.45 (1.48-1.45)
no. of reflections in working set [a]	384868 (25791)	201128 (11193)	381474 (23611)
no. of reflections in test set [a]	20362 (1319)	10625 (557)	20163 (1210)
R_{work} (%) [c]	13.5	15.0	13.58
R_{work} (%) [d]	16.2	19.5	16.44
ESU (Å) R_{work}/R_{free}	0.056/0.059	0.121/0.119	0.057/0.060
no. protein atoms	20265	19750	20036
no. coenzyme atoms	180	224	272
no. ligand atoms	52	26	49
no. water molecules	2516	1893	2432
RMS			
bond length (Å)	0.032	0.028	0.032
bond angle (deg.)	2.468	2.059	2.549
Ramachandran plot (%)			
favored	97.6	97.2	97.8
allowed	2.3	2.7	2.1
disallowed	0.1	0.1	0.1
average B-factor ($Å^2$)			
protein	12.1	17.2	12.7
coenzyme	7.3	11.2	8.3
ligands	28.3	33.8	33.0
waters	23.9	26.8	24.1
overall	13.4	18.0	14.0
occupancy per active site of HSCoM (%) [e]	100/100	90/90	90/85
occupancy per active site of CoBSH (%) [e]	30/30	50/50	40/40
CoBSH analogue, occupancy per active site (%) [e]		CoB_8SH, 50/50	CoB_9SH, 60/60
other molecule, occupancy per active site (%) [e]	acetate, 70/70		

[a] Values in parentheses correspond to the highest resolution shell.

[b] $R_{merge} = \Sigma_{hkl}\Sigma^{N}_{j=1}|I_{hkl}-I_{hkl}(j)|/\Sigma_{hkl}N*I_{hkl}$, sum over all reflections and all observations N, with $I_{hkl}(j)$ intensity of the j^{th} observation of reflection hkl and I_{hkl} mean intensity of the reflection hkl.

[c] $R_{work} = \Sigma||F_o| - |F_c||/\Sigma|F_o|$, where $|F_o|$ = observed structure factor amplitude and $|F_c|$ = calculated structure factor amplitude.

[d] R_{free}, R-factor based on 5% of the data excluded from refinement.

[e] Occupancy of model in each of the two crystallographically independent active sites in the ASU

visible absorption spectra for all crystals used in the X-ray diffraction experiments had a dominant peak at 420 nm corresponding to Ni(II)-$MCR_{red1\text{-}silent}$ with very little to almost no evidence of Ni(I)-MCR_{red1} absorption at 385 nm (Figure 1.6).

Figure 1.6 Single crystal UV-visible absorption spectra. (A) Solution spectrum of Ni(I)-MCR_{red1} used in anaerobic crystallization (solid line), and the same solution after being exposed to air and being oxidized to Ni(II) (dotted line). (B) Single crystal spectra (offset for clarity) collected on the crystals in this study following X-ray diffraction data collection. **(1) Oxidized Ni(II)-$MCR_{red1\text{-}silent}$ crystal**, **(2) MCR_{HSCoM}**, **(3) MCR_{CoB5SH}**, **(4) MCR_{CoB6SH}**, **(5) MCR_{CoB8SH}**, **(6) MCR_{CoB9SH}** and **(7) $MCR_{CoBSH + methyl\text{-}SCoM}$**.

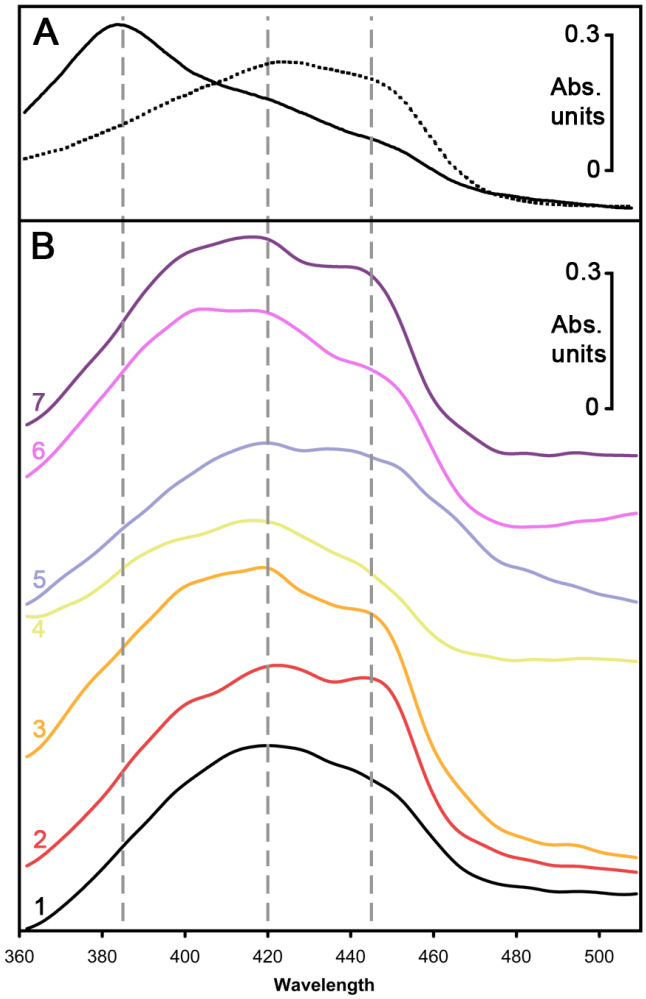

Photoelectrons generated from oxidation of solvent in the intense X-ray beam can often reduce redox centers. Earlier work had demonstrated that the Ni(II)-heterodisulfide complex (MCR_{silent}) could be cryoreduced by γ-irradiation at 77°K, followed by annealing at 262°K to generate Ni(I)-MCR_{red1}, although only at ~15% yield (*30*). At the wavelength of 0.973 Å where the data were collected, there was no evidence of reduction of Ni(II) to Ni(I) in our crystals. However, maximal photoelectrons are known to be generated at longer X-ray wavelengths (>1.5 Å), and this fact was used by Schlichting *et al.* to visualize ferryl heme in cytochrome P450cam crystals through addition of an X-ray generated photoelectron to a cytochrome P450-camphor-O_2 ternary complex (*56*). Therefore, crystals not used for X-ray diffraction data collection were exposed to high intensity X-ray irradiation at longer wavelengths, including at the Ni K-edge (8.33 keV, 1.489Å), to see if reduction of Ni(II)-MCR_{silent} to Ni(I)-MCR_{red1} could be achieved. However, there was no noticeable effect on the single crystal UV-visible absorption spectra indicating that the X-ray irradiation did not convert the Ni(II)-MCR_{silent} form to the Ni(I)-MCR_{red1} state (data not shown). Even at room temperature, where photoelectrons and radicals can propagate easily through the sample, there was no evidence of conversion of Ni(II) to Ni(I).

$MCR_{CoBSH + methyl\text{-}SCoM}$ crystal structure. The 1.35 Å resolution electron density was most consistent with 50% heterodisulfide product (CoBS-SCoM) (Figure 1.6A) and a background of 50% CoBSH and HSCoM (Table 1.1). Although the nickel had been oxidized to Ni(II) by the time X-ray data were collected, this crystal was the result of co-

crystallization of a predominantly Ni(I)-MCR_{red1} solution with CoBSH and methyl-SCoM substrates. This indicates that at least 50% of the enzyme was in the active Ni(I) state at the start of crystallization, as confirmed by the EPR data. A previous MCR crystal structure to 1.8 Å resolution also contained the heterodisulfide product at high yield (*7*). This was of the MCR_{silent} state, which is generated by growing and harvesting the protein in an H_2/CO_2 (80%/20%) atmosphere (Scheme 1.2). MCR purified anaerobically from these conditions contains the inactive Ni(II) state with the heterodisulfide bound in the substrate channel. The heterodisulfides from the previously deposited structure (PDB ID 1HBM) and the $MCR_{CoBSH + methyl\text{-}SCoM}$ structure presented here overlay well (root mean square deviation (r.m.s.d.) 0.125 Å) showing that the binding modes of heterodisulfide product generated *in vivo* and *in vitro* are the same. As in the previously described MCR_{silent} structure, we also observed that the CoB-portion of the product remains in an almost identical position to CoBSH (as observed in the $MCR_{ox1\text{-}silent}$ and $MCR_{red1\text{-}silent}$ structures (*6, 7*)), while the CoM-portion has moved so that one oxygen of the sulfonate group interacts with the Ni(II) at a distance of 2.1 Å.

Analogues shorter than CoBSH: CoB_5SH and CoB_6SH. CoB_5SH is two methylene groups shorter than CoBSH, the MCR substrate. The MCR_{CoB5SH} structure is to 1.3 Å resolution. As expected the pentanoyl chain follows the path of the CoBSH heptanoyl carbons down the substrate channel, and thus its thiol is positioned in the same place as the second carbon preceding the CoBSH thiol (Figure 1.5B and 1.7). There are no

published MCR kinetic studies using CoB_5SH, but as it binds in the substrate channel, it is likely to be an inhibitor.

Figure 1.7 Overlay of CoBSH (from PDB ID 1HBN) and the different CoBSH analogues. CoB_XSH are drawn as stick with the thiol represented by a sphere, and colored: CoB_5SH, orange; CoB_6SH, pale yellow; CoBSH, pale green; CoB_8SH, light blue; CoB_9SH, magenta. The protein is drawn as cartoon. Coenzyme F_{430} and HSCoM are drawn as stick colored by atom (carbon: F_{430}, dark grey; HSCoM, medium grey). The nickel is displayed as a green sphere.

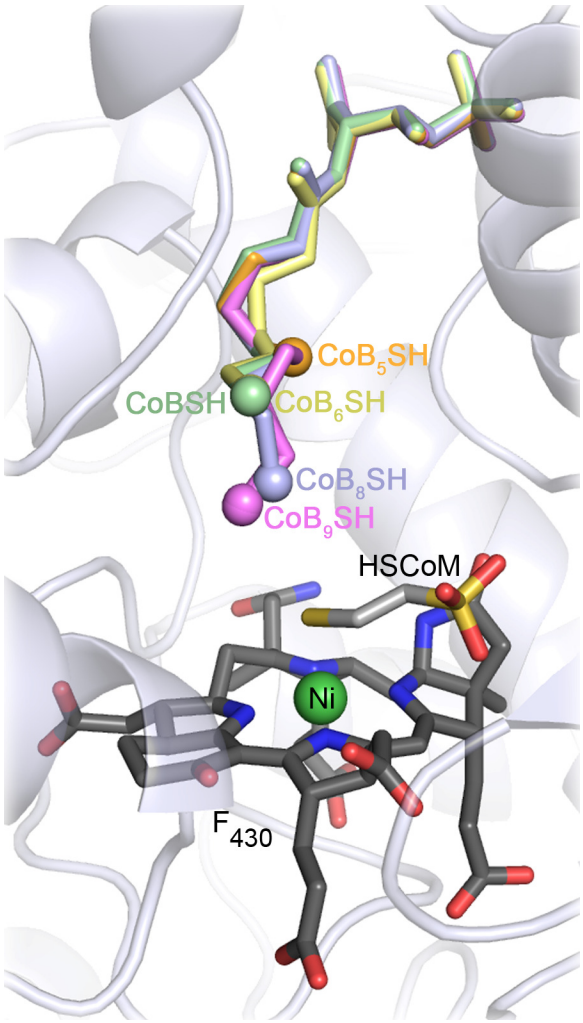

CoB_6SH is one methylene shorter than CoBSH, and is a slow substrate of MCR. In this case the 1.4 Å resolution electron density of MCR_{CoB6SH} indicates that the analogue binds in the substrate channel such that its thiol is virtually in the same position as the thiol of CoBSH (Figure 1.5C and 1.7). The hexanoyl chain is oriented so that it takes a shorter route down the substrate channel between carbons 2 and 5 (with the carbonyl carbon labeled as carbon 1) than CoBSH. This shortcut is not seen in any of the other CoB_XSH complex crystal structures, but presumably arises because this CoB_6SH binding conformer is energetically more favorable, although it is not clear from the structure why this might be the case.

Water structure in the absence of HSCoM. The electron density for the MCR_{CoB6SH} crystal structure only supported the modeling of 50% bound HSCoM. In the fraction of MCR molecules where HSCoM is absent, the HSCoM binding site is occupied by a network of four water molecules (Figure 1.8). Two water molecules are positioned close to the absent sulfonate oxygen positions of HSCoM. Based on the presence of positive difference electron density, a third water molecule was modeled ligated to the Ni, and refined to a distance of ~2 Å (2.0 Å and 2.1 Å in the two active sites of the ASU) with no distance restraint imposed between the Ni and oxygen atom. This water molecule is in a similar position as the Ni coordinating sulfonate oxygen of the heterodisulfide product in MCR_{silent} (Figure 1.5A and PDB ID 1HBM) (*6, 7*). The fourth water molecule is in the vicinity of the expected position of a "bridging" water molecule (W1) seen in other structures (Figure 1.1B and 1.5B,D).

Figure 1.8 Stereo image of the partially occupied HSCoM (50%) in the MCR_{CoB6SH} data. 2Fo-Fc electron density (contoured at 1σ) is shown as a blue mesh. The coenzymes are drawn in stick and colored by atom (carbon: F_{430}, dark grey; HSCoM, medium grey; CoB_6SH, pale yellow). The nickel is displayed as a green sphere and water molecules are displayed as red spheres.

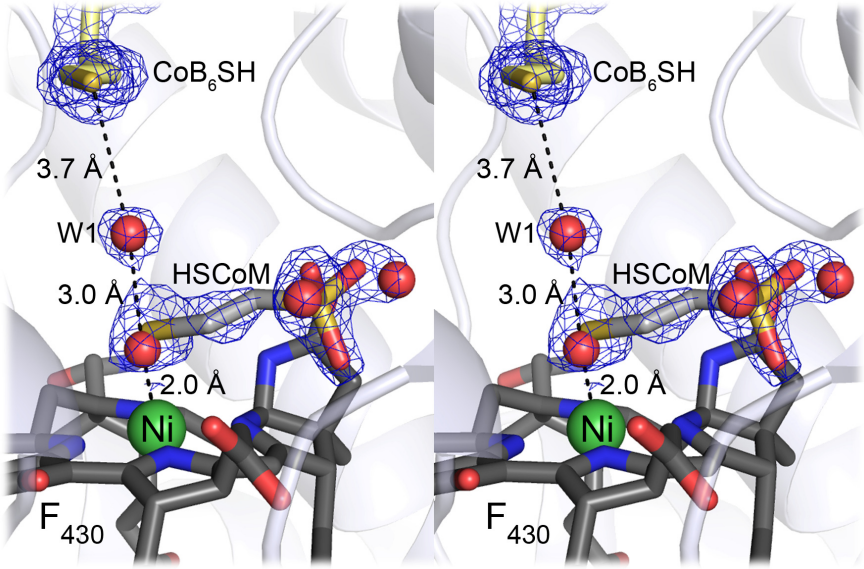

Water structure in the absence of CoBSH. The 1.45 Å resolution electron density obtained for MCR_{HSCoM} indicates that the substrate channel contains only 30% CoBSH. Nine ordered water molecules (W1-W9) occupy the channel, along with an acetate ion from the crystallization solution that binds where the phosphothreonine linkage of CoBSH would be (Figure 1.5D). Other than W3 and W7, the water molecules form hydrogen bonds with protein (Figure 1.9).

Position of the "bridging" water molecule, W1. The equivalent of W1 has previously been observed in $MCR_{red1\text{-}silent}$ and $MCR_{ox1\text{-}silent}$ crystal structures where, in the presence of CoBSH and HSCoM, it is sited equidistant (3.2 Å) between the two coenzyme thiols (PDB IDs: 1HBN, 1HBO, 1HBU) and thus been termed the "bridging water" (Figure

1.1B) (*6, 7*). However, in the MCR_{HSCoM} structure, due to the presence of the more polarized W2 water, W1 is displaced away from HSCoM to maximize the hydrogen bond with W2 (Figure 1.9). In the MCR_{CoB5SH} structure that also contained W2, the electron density indicated that this repositioning of W1 towards W2 also occurred. In contrast, the MCR_{CoB6SH} structure contained 100% thiol at the CoBSH position, but a partial occupancy of HSCoM (50%). In this case the electron density for W1 indicated it had moved towards the nickel to form an optimal hydrogen bond with a Ni-ligating water molecule that was only present in the absence of HSCoM (3.7 Å to $CoB_{(6)}SH$ thiol and

Figure 1.9 Hydrogen bonding diagram for the water structure modeled in MCR_{HSCoM}. The water molecules are named as in Figure 1.5D (W1-W9). WA, WB and WC are water molecules that are present in all structures (i.e. in concert with the substrate CoBSH, the CoBSH analogues presented and the heterodisulfide product). Interactions between surrounding residues and the water molecules are drawn as dashed lines, and the corresponding distance is indicated in Angstroms (Å).

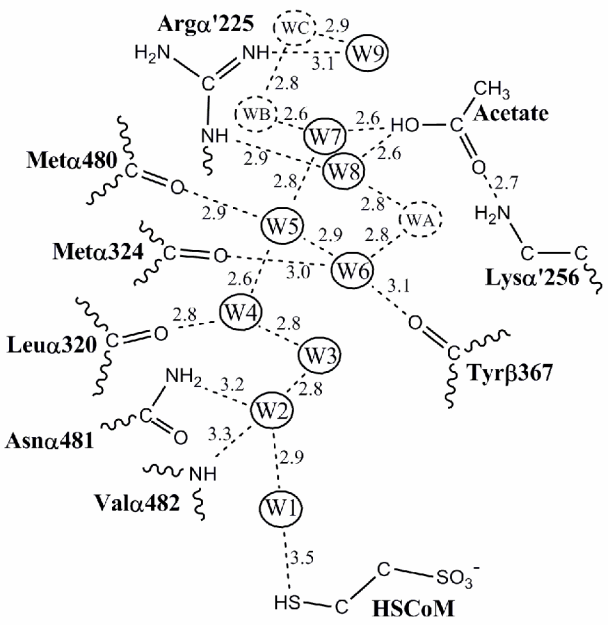

3.0 Å to Ni-ligating water molecule, Figure 1.8). In all structures reported here, W1 (if present) appears to be a sensitive indicator of the relative electronegativity of the Ni-ligated atom to that occupying the position of the CoBSH thiol and was a useful check in the crystallographic modeling and refinement process.

Flexibility in the substrate channel: alternative protein conformers. The binding site of HSCoM (and presumably methyl-SCoM) is deeper within the enzyme than the binding site of CoBSH, and so methyl-SCoM must enter prior to CoBSH for productive chemistry to occur. As binding of CoBSH in the absence of co-substrate would be inhibitory, it was suggested that a conformational change upon methyl-SCoM binding might lower the K_d for CoBSH, and thus promote an ordered mechanism. Compared to the $MCR_{ox1\text{-}silent}$ and $MCR_{red1c\text{-}silent}$ crystal structures (PDB IDs 1HBN and 1HBU, respectively) which both have full occupancy HSCoM, the lower occupancy of HSCoM in the $MCR_{red1\text{-}silent}$ structure (PDB ID 1HBO) was associated with significantly greater flexibility within the channel, and the ability to model a second conformation of a Gly-rich amino acid stretch that formed part of the CoBSH channel. This suggested that methyl-SCoM binding might cause the channel to become more ordered, increasing the affinity of MCR for CoBSH by conformational restriction rather than a switch mechanism where the structure reorganizes from one well-defined conformer to another (*7*). The MCR_{HSCoM} structure was modeled with 30% CoBSH and 100% HSCoM. The Fo-Fc difference electron density map at one of the two independent active sites in the ASU contained positive peaks that suggested the presence of an alternate conformation of

the polypeptide (Figure 1.10A). A second conformation involving seven contiguous amino acid residues of the same Gly-rich amino acid stretch (β366-372) could be modeled and refined at 20% occupancy, leaving no residual difference density. Parts of the α′ subunit (α′111-129 and α′237-242) that are in close proximity to this stretch of amino acids also exhibit second conformations, with the main-chain carbonyl of α′243 in van der Waals contact with the B ring of F_{430} tetrapyrrole (Figure 1.10B). Modeling

Figure 1.10 Conformational changes in MCR. (A) Two conformations of the glycine rich loop seen in the MCR_{HSCoM} data overlaid with the previously published alternative conformation. Models are drawn as stick and colored by atom (carbon: F_{430}, dark grey; HSCoM, medium grey; CoBSH, pale green; main loop conformer, white; alternative conformer, maroon; previously published alternative conformation, faded wheat). 2Fo-Fc electron density (contoured at 1σ) is shown as a blue mesh. Positive peaks in the Fo-Fc difference electron density map (contoured at 4σ), before modeling of the alternative conformation, are shown as a green mesh. The nickel is displayed as a green sphere. (B) Propagation of conformational changes in MCR_{HSCoM}. The overall protein is drawn as cartoon, with the C_α traces for the parts of the protein with alternate conformers drawn as stick (main conformer, white; alternate conformer observed in MCR_{HSCoM} data, maroon). The coenzymes and nickel are illustrated as in (A).

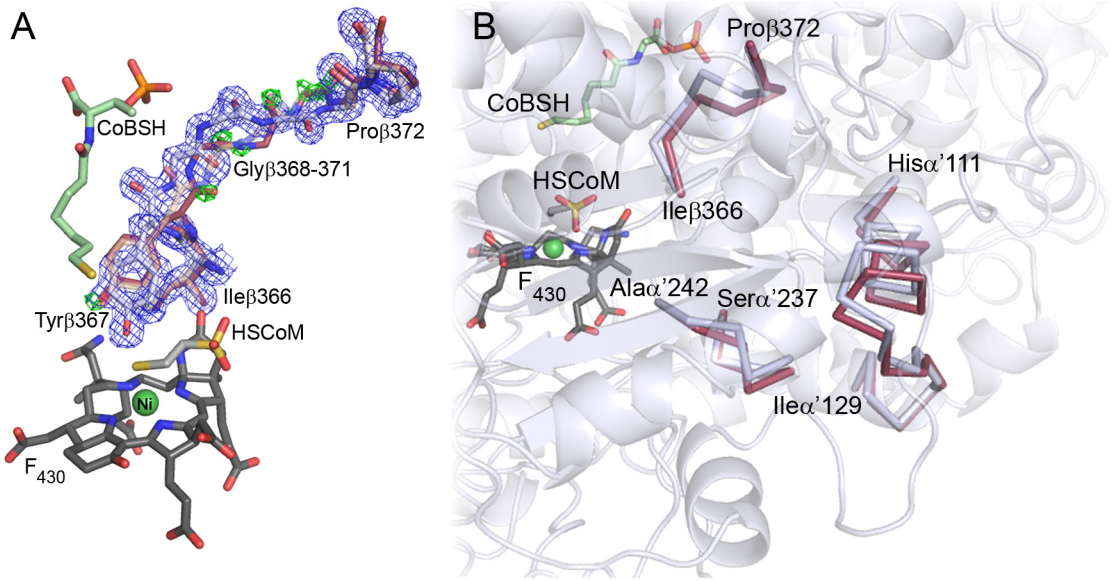

these at 20% occupancy accounted for the weak positive Fo-Fc difference electron density peaks observed in these areas. The evidence of the alternate conformers lends support to the proposal that increased flexibility in the substrate channel propagates through the protein (*7*).

Analogues longer than CoBSH; CoB_8SH and CoB_9SH. Both analogues could be accommodated in the MCR substrate channel (Figure 1.5E,F). The electron density supported final models containing 50% CoB_8SH for MCR_{CoB8SH} (1.8 Å resolution) and 60% CoB_9SH for MCR_{CoB9SH} (1.45 Å resolution). The phosphate head-groups are in identical positions to those of CoBSH, CoB_5SH, CoB_6SH (Figure 1.7) and the heterodisulfide (*6, 7*). Both analogues follow the crystallographically observed carbon chain path of bound CoBSH, with the extra atoms displacing W1 and placing the thiols closer to the nickel (Figure 1.11). CoB_9SH does have a second conformer (modeled at 30% occupancy) that deviates from the CoBSH path, but the thiol position for this conformer and the CoBSH-tracking conformer are identical (Figure 1.5F). Interestingly, the thiol of CoB_8SH is not coincident with the CoB_9SH carbon that precedes the CoB_9SH thiol (Figure 1.11). CoB_8SH is an MCR inhibitor with an apparent K_i of 15 μM (*4*). CoB_9SH has never been tested for inhibition of MCR-catalyzed methane formation, but it is reasonable to assume that it would be an inhibitor.

CoB_XSH thiol-to-nickel spatial relationship. In all the proposed catalytic mechanisms, CoBSH must interact with species generated at the nickel. Trigonometry suggests that if the alkanoyl chain of CoBSH or its analogue is in an extended conformation, each additional unit in the chain would lead to the thiol moving ~1.2 Å towards the Ni. Until this study there have been no crystal structures of CoBSH analogues in complex with MCR, so mechanistic studies using different chain length analogues of CoBSH assumed that shorter analogues would trace the observed path of CoBSH, and longer analogues would penetrate about ~1.2 Å deeper per additional chain unit into the channel. In the case of the shortest analogue CoB_5SH, it does indeed follow the path of CoBSH, with the thiol of CoB_5SH being 2.8 Å away from the thiol position of CoBSH. However, due to the conformation CoBSH adopts when bound in the substrate channel the difference in the S – Ni distance is small: the CoB_5SH thiol being only 0.5 Å farther from the Ni than CoBSH (8.8 Å for CoBSH *vs*. 9.3 Å for CoB_5SH) (Table 1.3). This is due to the alkanoyl chain of CoBSH not being in an extended conformation from carbons 4 to 6 (carbon 1 is the carbonyl carbon). CoB_6SH on the other hand adopts a conformation that places its thiol in virtually the same position as the thiol of CoBSH (Figure 1.7 and Table 1.3). If the positioning of the CoBSH thiol seen in crystal structures of the MCR-Ni(II) state is of catalytic importance, the fact that CoB_6SH is in the same position could explain why CoB_6SH is a substrate. However, the k_{cat} is 1000-fold lower than for CoBSH (*4*) although its K_m value (80 ± 20 μM (*57*)) is similar to that of CoBSH (K_m = 75 μM (*4*)). A explanation to why CoB_6SH is such a poor substrate may be that the shorter alkanoyl

chain cannot enable the analogue thiol to approach the nickel close enough for efficient catalysis.

The sulfur of CoB_8SH is 2.6 Å closer to the Ni ion of F_{430} than that of CoBSH, and 2.5 Å closer to the thiol of HSCoM (Figure 1.11 and Table 1.3). The CoB_9SH molecule follows the path of CoBSH and reaches only a little further into the substrate channel than CoB_8SH, with the CoB_9SH thiol sitting 2.9 Å closer to the Ni than the thiol of CoBSH. This is only 0.3 Å closer than the distance observed for the CoB_8SH thiol, even though they are non-coincident. The distance to the thiol of HSCoM is 2.6 Å closer than that of the substrate, CoBSH (only 0.1 Å closer than the CoB_8SH thiol). The two analogue thiols sit above an annular hydrophobic aromatic environment created by Pheα330, Tyrα333, Pheα443, Pheβ361 and Tyrβ367 that lies between them and F_{430} (Figure 1.11). As a result, penetrating further into the channel may be energetically unfavorable, consistent with the small difference in relative distances between the CoB_8SH / CoB_9SH thiols and the HSCoM thiol or F_{430} nickel (Table 1.3). The annulus is proposed to be catalytically important in positioning methyl-SCoM and stabilizing the methane product, and the tyrosines have been proposed to be proton donors associated with mechanism II (Scheme 1.3) (*6, 7*).

Based on the results above, there appear to be two preferential distances for thiols within the MCR substrate channel: CoB_6SH / CoBSH at 8.7-8.8 Å and CoB_8SH / CoB_9SH at 5.9-6.2 Å from the nickel of F_{430}.

Figure 1.11 Stereo image of the annulus of aromatic amino acids distal of coenzyme F_{430}. The protein is drawn as cartoon with the side-chains of the aromatic residues drawn as white stick. CoBSH, (from PDB ID 1HBN), CoB_8SH and CoB_9SH are drawn as stick with the thiols represented by spheres, and colored: CoBSH, pale green; CoB_8SH, light blue; CoB_9SH, magenta. Coenzyme F_{430} and HSCoM are drawn as stick colored by atom (carbon: F_{430}, dark grey; HSCoM, medium grey). The nickel is displayed as a green sphere.

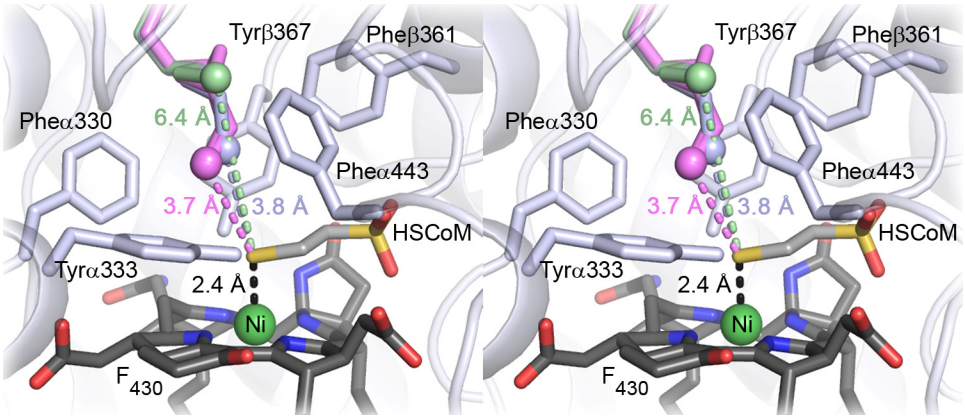

Reaction of MCR Ni(III)-alkyl species with CoB_8SH and CoB_9SH. The two longer CoBSH analogues have been shown to undergo alkylation when reacted with MCR_{PS}, a [Ni(III)-alkyl ↔ Ni(II)-propylsulfonate radical] formed from reaction of Ni(I)-MCR_{red1} with bromopropanesulfonate (BPS) (Scheme 1.2) (*25, 27, 34, 46, 58*). BPS is a substrate of MCR_{red1} in a reaction that involves a rapid CoBSH-independent nucleophilic attack by Ni(I) on BPS to displace bromide and generate MCR_{PS} at a rate ~60-fold faster than generation of methane from CoBSH and methyl-HSCoM (*25, 46*). Certain thiols can eliminate the propylsulfonate to yield a thioether product and regenerate MCR_{red1}, although at a rate 1000-fold slower than methane formation (*46*). Both CoB_8SH and CoB_9SH can react with MCR_{PS} to regenerate MCR_{red1}, but CoBSH cannot. The overall second-order rate constant for the reactivation of MCR by CoB_8SH is 160 M^{-1} s^{-1},

whereas for CoB_9SH the reaction is slower (12 M^{-1} s^{-1}). Since CoB_9SH might be expected to be closer to the distal Ni ligand, it was proposed that this caused steric interference that explained why CoB_9SH was a poorer reactivator of MCR than CoB_8SH. Our study has shown that the thiols of CoB_8SH and CoB_9SH are placed such that they are approximately the same distance (~3.7 Å) from the thiol of HSCoM ligated to the Ni atom (Table 1.3). The Ni(II)-HSCoM bond is 2.4 Å, whereas a Ni(III)-alkyl bond is expected to be ~2 Å (*28*), indicating that a conformational change is required to effect the nucleophilic attack of the CoB_8SH and CoB_9SH thiols on an alkyl-bound species.

Table 1.3 Distances from CoBSH and analogue thiols

	CoB_XS – SCoM distance (Å)	CoB_XS – Ni distance (Å)
CoB_5SH	7.11/7.11[a]	9.30/9.30
CoB_6SH	6.26/6.26	8.70/8.70
CoB_7SH (substrate) [b]	6.37/6.39	8.73/8.77
CoB_8SH	3.75/3.78	6.16/6.17
CoB_9SH	3.71/3.68	5.96/5.91

[a] Distances in the two crystallographically independent active sites in the ASU.
[b] Distances in the 1.16 Å resolution $MCR_{ox1\text{-}silent}$ structure (PDB ID 1HBN) (*7*).

A Ni(III)-alkyl species is akin to the first intermediate in mechanism I of MCR-catalyzed methane formation, Ni(III)-methyl (MCR_{Me}, Scheme 1.2) (*16, 31*). MCR_{Me} has been shown to be capable of generating MCR_{red1} and methyl-SCoM upon addition of HSCoM (which is the reverse of step 1 in mechanism I, Scheme 1.3), similar to the chemistry observed in formation of a CoB_8SH and CoB_9SH thioether product from the Ni(III)-alkyl. Further addition of CoBSH to MCR_{Me} in the presence of HSCoM led to methane and heterodisulfide formation, the natural products of methanogenesis.

Although this lends credence to mechanism I, it should be noted that like MCR_{PS}, MCR_{Me} in these experiments was generated artificially. The MCR_{CoB9SH} crystal structure demonstrates that the two additional methylene units in the alkanoyl chain *c.f.* CoBSH, do not necessarily translate into direct interaction of the thiol with the nickel proximal ligand. However, this could represent the favorable position for a CoBSH thiol interacting with the methyl group of methyl-SCoM. Just as the alkanoyl chain of CoB_6SH has a more extended conformation than CoBSH in the substrate channel, CoBSH could also adopt a more extended conformation so that its thiol was in a similar position as the thiol of CoB_8SH, priming it for reaction with a nickel-bound species.

If a significant conformational change does occur early in MCR-catalyzed chemistry, which would be a requirement of mechanism I, this may well involve a rearrangement of the aromatic amino acid annulus due to the presence of the methyl of methyl-SCoM, and this might enable deeper penetration of CoBSH into MCR (Figure 1.11). All of the crystal structures in this study, and those solved previously, are of the inactive Ni(II)-MCR, which disfavors close approach to the nickel, even in the case of CoB_9SH.

1.2.3 Conclusion

The goal of this study was to induce structural changes within the substrate channel and active site of MCR using analogues of coenzyme CoBSH. It was hoped that this would shed light on the nature of conformational changes that have been proposed to occur in MCR catalysis. We have shown that the CoB_XSH analogues do not lead to any significant conformational changes within the context of inactive Ni(II)-MCR. Therefore, it may be that methyl-SCoM is the key coenzyme, in combination with a nickel oxidation state of +1 (and +3), that triggers a conformational change bringing the thiol of CoBSH closer to the nickel. The crystal structure of the Ni(I)-methyl-SCoM – MCR complex may be the key to structurally define conformational changes required for MCR-mediated chemistry.

The atomic coordinates and structure factors have been deposited in the Protein Data Bank as PDB IDs: 3M2R (MCR_{CoB5SH}), 3M2U (MCR_{CoB6SH}), 3M2V (MCR_{CoB8SH}), 3M30 (MCR_{CoB9SH}), 3M1V (MCR_{HSCoM}) and 3M32 ($MCR_{CoBSH + methyl\text{-}SCoM}$).

1.3 A structural study of a Ni-methyl species in methyl-coenzyme M reductase

In the methanogenic archaea, methyl-coenzyme M reductase (MCR) catalyzes the final and rate-limiting step in methane biogenesis: the reduction of methyl-coenzyme M (methyl-SCoM, 2-(methylthio)ethanesulfonate) by coenzyme B (CoBSH, *N*-7-mercaptoheptanoylthreonine phosphate) to methane and a heterodisulfide. No true catalytic intermediate of MCR has ever been observed, and thus the mechanism of MCR catalyzed methanogenesis remains elusive. One of the proposed mechanisms involves the formation of a MCR-Ni(III)-methyl species (MCR_{Me}). MCR_{Me} can be generated from MCR-Ni(I) (MCR_{red1}) and methyl halide. Treatment of the methyl halide produced MCR_{Me} with coenzyme M (HSCoM, demethylated methyl-SCoM) generates MCR_{red1} along with the substrate methyl-SCoM, supporting this species as a possible catalytic intermediate. Here we describe the 1.2 Å resolution X-ray crystal structure of MCR in the potentially mechanistic relevant MCR_{Me} state generated from MCR_{red1} and methyl iodide. The methyl group is situated 2.1 Å proximal of the Ni atom of the MCR coenzyme F_{430}. A rearrangement of the substrate channel has been proposed to bring together substrate species, but Ni(III)-methyl formation alone does not lead to any observable structural changes in the channel.

The contents of this section are reprinted (adapted) with permission from:

Cedervall, P. E., Dey, M., Li, X., Sarangi, R., Hedman, B., Ragsdale, S. W., and Wilmot, C. M. (2011) "Structural analysis of a Ni-methyl species in methyl-coenzyme M reductase from *Methanothermobacter marburgensis*", *J. Am. Chem. Soc. 133*, 5626-5628.

1.3.1 Methods

Protein expression and purification. MCR_{red1} was isolated from *Methanothermobacter marburgensis* cultured on H_2/CO_2 (80%/20%) at 65 °C and purified as previously described (*28, 55*). The purification procedure routinely generates ~70% MCR_{red1} as determined by UV-visible absorption and EPR spectroscopy (*55*).

Crystallization and crystal treatment. All crystallization experiments and crystal manipulation were performed under N_2 atmosphere in a Vacuum Atmospheres anaerobic chamber. For the single crystal X-ray absorption spectroscopy experiment, a MCR_{red1} crystal was obtained by sitting drop vapor diffusion method over 1 ml reservoir solution at 9°C. 2 µl of enzyme solution containing 322 µM MCR_{red1}, and 1 mM CoBSH analogue (CoB_6SH, Figure 1.2) in 50 mM Tris pH 7.6 and 100 mM Ti(III) citrate was mixed with 2 µl of reservoir solution containing 100 mM Hepes-Na pH 8.0, 150 mM magnesium acetate ($Mg(CH_3COO)_2$) and 22% (v/v) PEG 400. After 2 days of growth the green Ni(I) crystal was harvested and soaked for 1 minute in reservoir solution containing 20 mM methyl iodide. The soaked crystal was quickly cryo-protected in reservoir solution containing 25% (v/v) PEG 400 before being flash-frozen in liquid propane. The liquid propane filled cryo vial was then transferred into liquid nitrogen forming a propane "popsicle". For the X-ray diffraction experiment the MCR crystal was obtained by sitting drop vapor diffusion method at room temperature. 2 µl of enzyme solution containing 300 µM MCR_{red1}, 1 mM methyl iodide and 1 mM CoB_6SH in 50 mM Tris pH 7.6 and

100 mM Ti(III) citrate was mixed with 2 µl of reservoir solution containing 100 mM Hepes-Na pH 7.5, 150 mM $Mg(CH_3COO)_2$ and 20% (v/v) PEG 400. The crystallization drop was micro-seeded and the crystal was allowed to grow for 16 hours after which it was harvested and flash frozen in liquid nitrogen. No additional cryo-protectant was needed.

Single crystal X-ray absorption spectroscopy. Ni K-edge X-ray absorption spectra were measured at the Stanford Synchrotron Radiation Lightsource on the 16-pole, 2.0 T, wiggler beamline 9-3. A liquid nitrogen cooled Si(220) double crystal monochromator was used for energy selection (ϕ=90^o). A Rh-coated harmonic rejection mirror and a cylindrical Rh-coated bent focusing mirror were used. An Oxford Instruments open flow liquid He cryostat was used to maintain the sample temperature at ~30°K throughout the course of data measurement. Near-edge XAS data were measured in fluorescence mode using a Canberra Ge-30 element array detector. Internal energy calibration, monochromator and atomic background subtraction and data normalization were performed as previously described (*28*). The MCR_{Me} data were contaminated with a small amount of background Ni signal, which does not allow for a comparison of the pre-edge region.

X-ray diffraction data collection, processing and refinement. X-ray diffraction data were collected from a single methyl iodide treated MCR crystal at three different wavelengths: 0.98 Å (native), 1.51 Å and 2.29 Å. The data sets at 0.98 Å and 1.51 Å were collected at

beamline 19-ID (SBC) at the Advanced Photon Source, Argonne National Laboratory at 80 and 15°K, respectively. The 2.29 Å data set was collected in-house using a MicroMax-007 chromium source with VariMaxCr optics and a R-AXIS IV++ detector with a helium cone (Rigaku) at 100°K. The native 0.98 Å data were collected first, followed by the 1.51 Å data and then the 2.29 Å data. The X-ray diffraction data were processed using HKL2000 (*51*). As in the previous X-ray crystallographic studies, the crystals belong to the monoclinic space group $P2_1$ (a = 82 Å, b = 118 Å, c = 122 Å, β = 92°), with one MCR molecule (two active sites) per asymmetric unit (*6, 7*). The crystal X-ray diffraction data collection statistics are shown in Table 1.4.

Initial phases for the native X-ray diffraction data collected at wavelength 0.98 Å were generated by difference Fourier using a previously determined crystal structure of MCR (PDB ID 3M2R (*55*)) as a model, but with all water molecules, coenzymes (except F_{430}) and metal ions removed. The initial *R*-values were 22.9% and 24.9% for R_{work} and R_{free}, respectively. Refinement was done in REFMAC (*59*) in the CCP4 suite (*52*). The Ni – methyl distance was restrained to 2.0 Å and the Ni – SCoM distance was restrained to 2.4 Å based on solution XAS distances (*28*). Model building was done in Crystallographic Object-Oriented Toolkit (COOT) (*53*). To assure the best possible phases for the structural data and to avoid model bias, the last things to be added to the model were the species in the active site (i.e. coenzymes, methyl and iodide). The model was deemed to be final when all interpretable areas of electron density (2Fo-Fc and Fo-Fc) were explained and the B-factors for the cofactors converged. In the final round of refinement, the model was refined with anisotropic temperature factors and the matrix weighting term

Table 1.4 X-ray diffraction data collection, processing and refinement statistics

Data collection and processing statistics			
Collected at wavelength (Å)	0.98	1.51	2.29
Unique reflections	721334	246471	83432
Redundancy	3.9	3.8	14.0
Resolution (Å) [a]	50.0-1.20 (1.24-1.20)	50.0-1.72 (1.78-1.72)	50.0-2.44 (2.53-2.44)
Completeness (%) [a]	100 (100)	99.8 (99.1)	96.0 (98.6)
R_{merge} (%) [a, b]	7.5 (43.0)	5.9 (30.4)	9.4 (14.6)
$I/\sigma I$ [a]	19.5 (3.7)	22.4 (4.8)	97.8 (63.7)

Refinement and model building statistics	
Resolution (Å) [a]	50.0-1.20 (1.23-1.20)
No. of reflections in working set [a]	685122 (50103)
R_{work} (%) [c]	13.2
R_{work} (%) [d]	15.6
ESU (Å) R_{work}/R_{free}	0.035 / 0.034
No. protein atoms	19411
No. ligand/ion atoms	241
No. water molecules	2637
RMS	
bond length (Å)	0.020
bond angle (deg.)	1.932
Ramachandran plot (%)	
favored	98.0
allowed	1.9
disallowed	0.1
average B-factor ($Å^2$)	
protein	10.8
ligands	7.5
waters	23.0

[a] Values in parentheses correspond to the highest resolution shell.
[b] $R_{merge} = \Sigma_{hkl}\Sigma^{N}_{j=1}|I_{hkl}-I_{hkl}(j)|/\Sigma_{hkl}N*I_{hkl}$, sum over all reflections and all observations N, with $I_{hkl}(j)$ intensity of the j^{th} observation of reflection hkl and I_{hkl} mean intensity of the reflection hkl.
[c] $R_{work} = \Sigma||F_o| - |F_c||/ \Sigma|F_o|$, where $|F_o|$ = observed structure factor amplitude and $|F_c|$ = calculated structure factor amplitude.
[d] R_{free}, R-factor based on 5% of the data excluded from refinement.

was set to 2.0. As a control, electron density maps were generated with the final structural model but with the methyl taken out. The resulting map shows a positive Fo-Fc electron density peak between the HSCoM thiol and F_{430}-Ni leading to the conclusion that a methyl group is needed to explain the electron density (Figure 1.12). The anomalous electron density maps were generated using the CCP4 suite (*52*). Structural

figures were generated using PyMOL (*60*).

Figure 1.12 Indication of a proximal methyl group. Stereo figure showing positive Fo-Fc electron density (green mesh, contoured at 5σ) when methyl is not included in the structural model. 2Fo-Fc electron density (contoured at 1σ) is shown as blue mesh. Coenzymes are shown in stick colored by atom (carbon: CoB_6SH, pale yellow; CoBSH, pale green; HSCoM, light grey (faded); coenzyme F_{430}, dark grey). The Ni is shown as a green sphere, iodide as a purple sphere and a water molecule as a red sphere. Protein is shown as cartoon.

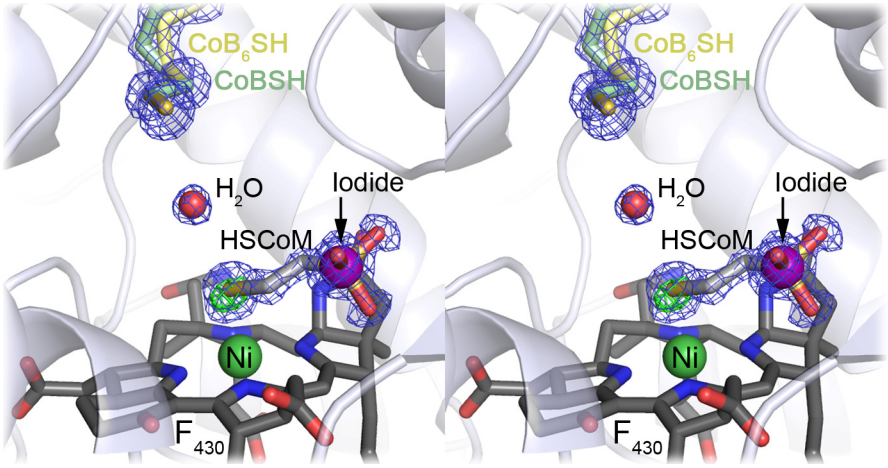

Electron paramagnetic resonance spectroscopy. X-band EPR spectra were recorded on a Bruker EMX spectrometer (Bruker Biospin Corp.), equipped with an Oxford ITC4 temperature controller, a Hewlett-Packard model 5340 automatic frequency counter, and Bruker gaussmeter. Two EPR samples were prepared after the addition of methyl iodide to MCR_{red1}. One of the samples was frozen right away and the other was left sitting in the anaerobic chamber at room temperature until the time of mounting the crystal (16 hours after the formation of MCR_{Me}). EPR parameters used were: microwave frequency, 9.384 GHz; microwave power, 10 mW; modulation frequency, 100 kHz; modulation amplitude, 10 G and temperature, 70°K.

X-ray dose calculation and photoreduction. The total X-ray dose absorbed by the crystals used in the X-ray diffraction and single crystal XAS experiments was calculated using RADDOSE (*61*).

1.3.2 Results

X-ray absorption spectroscopy. To confirm that MCR_{Me} could form *in crystallo*, a Ni K-edge XAS spectrum was obtained from a MCR_{red1} crystal treated anaerobically with methyl iodide (Figure 1.13). The XAS rising-edge region holds electronic structure information about the Ni center while the near-edge XAS region contains long distance (~10 Å) single and multiple-scattering information due to the large photoelectron mean free path at low energies. Therefore the rising-edge inflection point and the near-edge beat pattern uniquely define the geometric and electronic structure around the absorbing atom. The methyl iodide treated crystal has a beat pattern and rising-edge inflection point very similar to that of MCR_{Me} in solution, and dissimilar to that of MCR_{red1} and inactivated Ni(II)-$MCR_{red1\text{-}silent}$ state (Figure 1.13). Thus, the near-edge XAS data demonstrate formation of the MCR_{Me} state in the crystal.

Electron paramagnetic resonance spectroscopy. The spectra collected on the MCR_{Me} crystallization protein solution at the time the X-ray diffraction crystal was frozen indicated that a significant proportion of MCR_{Me} was still present (data not shown).

X-ray crystallography. The refinement of the final MCR model against the 1.2 Å resolution X-ray diffraction data collected with a radiation wavelength of 0.98 Å generates *R*-values of 13.2 and 15.6% for R_{work} and R_{free}, respectively. 98.0% of the residues are in the favored regions of the Ramachandran plot (1.9% are in allowed

Figure 1.13 X-ray absorption spectra. (A) Normalized Ni K-edge XAS spectra: $MCR_{red1\text{-}silent}$ (solution), black trace; MCR_{Me} (solution), red trace and MCR_{Me} (crystal), blue trace. (B) The 1st derivative spectra showing the shift in edge inflection point: MCR_{red1} (solution), green trace; $MCR_{red1\text{-}silent}$ (solution), black trace; MCR_{Me} (solution), red trace and MCR_{Me} (crystal), blue trace.

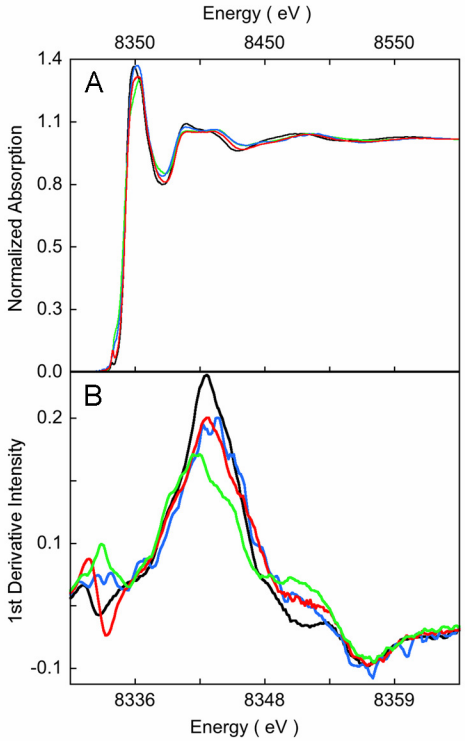

regions and 0.1% are outliers). Refinement statistics are shown in Table 1.4. The overall protein structure is very similar to previously solved crystal structures of MCR (*6-8, 55*). The electron density indicates the partial presence of HSCoM in the active site pocket. At wavelength 2.29 Å, sulfur has an anomalous signal (f″-value) of 1.14 electrons, and anomalous electron density peaks are observed for all well ordered sulfur atoms in the protein (Table 1.5). In the anomalous electron density map, the HSCoM thiol has an anomalous peak height lower than that of other sulfur peaks, as well as the peak of the Ni (f″-value of 1.03 electrons) in F_{430} (Figure 1.14A). This confirms that HSCoM is not

Table 1.5 Expected anomalous signals and observed peak heights

Wavelength (Å)	**0.98**	**1.51**	**2.29**
f'' for atom type (unit: electrons) [a]			
S	0.23	0.54	1.14
Ni	1.95	0.49	1.03
I	3.18	6.63	12.82
Peak height (unit: sigma) [b]			
methionine [c]	7.0±1.6	6.9±1.2	9.0±1.5
cystein [c]	7.6±1.3	6.8±1.1	8.7±1.2
thioglycine [d]	8.0/5.0	7.5/6.6	10.6/10.2
$CoB_{(6)}SH$ thiol [d]	6.4/5.1	7.5/6.3	12.1/10.4
HSCoM thiol [d]	N/A [e]	N/A [e]	7.0/5.3
Ni [d]	58.0/54.3	7.1/5.8	10.4/8.2
Iodide and HSCoM sulfonate [d]	32.3/30.2	41.2/39.7	50.7/46.9

[a] Values generated in the program crossec
[b] Peak list generated in the program FFT in the CCP4 program suite
[c] Arithmetic mean ± standard deviation. 0.98 Å: 58 Met peaks, 13 Cys peaks; 1.51 Å: 60 Met peaks, 12 Cys peaks; 2.29 Å: 61 Met peaks, 12 Cys peaks.
[d] Peaks in the two crystallographic independent molecules in the asymmetric unit
[e] No peak above noise level

present at 100% occupancy. Refinement supported a model containing 50% methyl and 50% HSCoM proximal to the nickel, with the latter at a Ni-S distance of 2.4 Å which is in line with the previous crystal structures containing HSCoM (*6-8, 55*) and the distance reported by XAS (*28*). Due to the background HSCoM, the Ni – C bond was restrained to 2.0 Å during refinement (the distance determined by XAS for MCR_{Me} in solution is 2.04 Å (*28*)) and the final model has a Ni – C distance of 2.07 Å and 2.10 Å in the two crystallographically independent active sites in the asymmetric unit. This model led to B-factors equivalent to those of surrounding atoms, and generated no Fo-Fc difference density proximal to the nickel (Figure 1.15). In contrast to the relatively weak anomalous peak at the thiol of HSCoM, the peak at the sulfonate sulfur position of HSCoM is much stronger than any other peak associated with a sulfur atom (Figure 1.14A). If HSCoM was the only species present the peak corresponding to the thiol and the sulfonate group

Figure 1.14 Anomalous electron density maps from X-ray diffraction data collected at: (A) wavelength 2.29 Å (contoured at 5σ) is shown as orange mesh (f″ (electrons): sulfur 1.14; nickel 1.03; iodine 12.82); (B) wavelength 0.98 Å (contoured at 5σ) is shown as magenta mesh (f″ (electrons): sulfur 0.23; nickel 1.95; iodine 3.18); (C) wavelength 1.51 Å (contoured at 5σ) is shown as cyan mesh (f″ (electrons): sulfur 0.54; nickel 0.49; iodine 6.63). Coenzymes are shown in stick colored by atom (carbon: CoB_6SH, pale yellow; CoBSH, pale green; HSCoM, light grey; coenzyme F_{430}, dark grey with the Ni atom shown as a green sphere). Methyl is displayed as a grey sphere, iodide as a purple sphere and a water molecule as a red sphere. Protein is shown as cartoon.

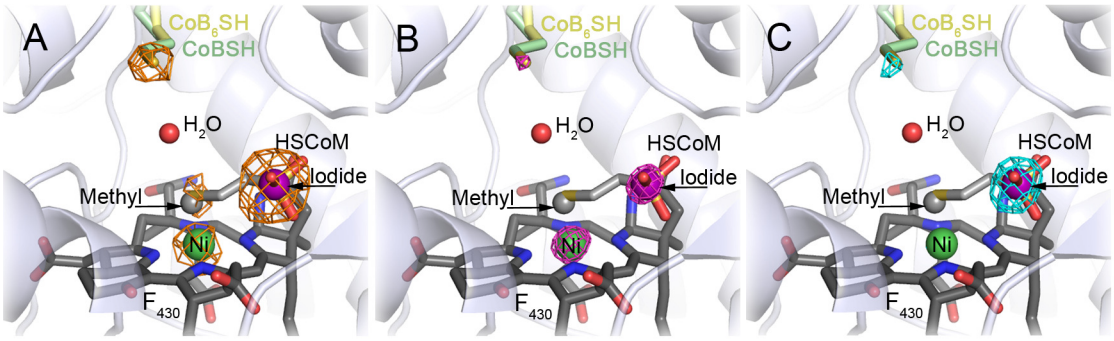

should be of equal height. It was suspected that the model needed to explain the electron density at the HSCoM sulfonate sulfur was an iodide ion remaining in the active site after the formation of MCR_{Me} from methyl iodide. The f″-value for I at wavelength 2.29 Å is 12.82 electrons, about twelve times the expected signal of Ni and S. To help define the atom identity of the missing model at the HSCoM sulfonate sulfur, two additional anomalous electron density maps generated from X-ray diffraction data collected at 0.98 Å (native) and 1.51 Å were used. The anomalous electron density map generated from data collected at wavelength 0.98 Å was consistent with the presence of an atom with an electron count comparable to that of Ni in F_{430} present at 100% occupancy (Figure 1.14B). For equivalent occupancies the expected anomalous signal for Ni would be ~60% of the signal expected for I at this wavelength (f''_{Ni}=1.95 *cf.* f''_{I}=3.18 electrons),

Figure 1.15 Final structural model and electron density. The final model contains a 60:40 mixture of coenzyme B_6 (CoB_6SH) and coenzyme B (CoBSH), 50% coenzyme M (HSCoM), 50% methyl and 35% iodide. Coenzymes are shown in stick colored by atom (carbon: CoB_6SH, pale yellow; CoBSH, pale green; HSCoM, light grey (faded); coenzyme F_{430}, dark grey with the Ni atom shown as green sphere). Methyl is displayed as a grey sphere, iodide as a purple sphere and a water molecule as a red sphere. Protein is shown as cartoon. 2Fo-Fc electron density (contoured at 1σ) is shown as blue mesh.

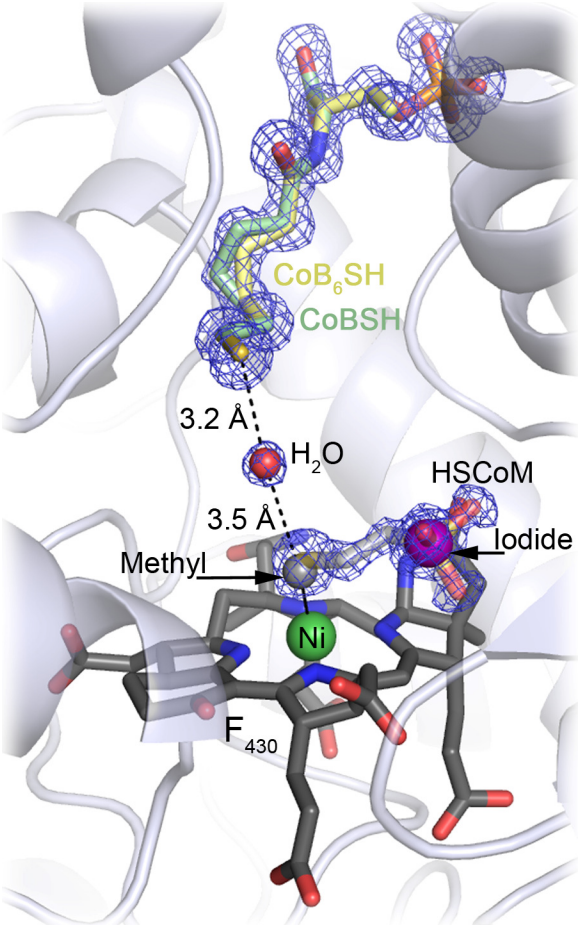

indicating a lower occupancy than Ni if the missing model is iodide. This is consistent with the anomalous data at wavelength 2.29 Å, which indicates that some HSCoM is present (modeled at 50% based on the proximal electron density to the Ni), and whose presence is incompatible with iodide. The anomalous electron density generated from

data collected at 1.51 Å suggests the presence of an atom with an f″-value larger than that of any other atom present in the active site (Figure 1.14C). The expected f″-value for I present at 100% occupancy at 1.51 Å is 6.63 electrons. This is about twelve times the expected signal of Ni and S, which both have f″-values close to 0.5 electrons. So even if iodide is only present at 50% or less occupancy due to the presence of 50% HSCoM, the expected anomalous peak height would be much larger than that of Ni and S at wavelengths 1.51 and 2.29 Å. Taken together, the trend seen in the anomalous electron density maps supports the missing model being iodide. The final model that leads to no interpretable Fo-Fc difference electron density, B-factors approximately equivalent on atoms throughout the active site and is consistent with the anomalous data contains 50% methyl, 50% HSCoM and 35% iodide.

To reduce turnover and prevent side reactions (i.e. formation of methylated CoBSH (*15*)) MCR was co-crystallized with an analogue of CoBSH (CoB_6SH) that is one carbon shorter than the CoBSH alkanoyl chain (Figure 1.2). The natural substrate, CoBSH follows the enzyme through the purification steps and, like HSCoM, cannot be completely removed even after multiple rounds of buffer exchange. Refinement supported a 60/40 mixture of CoB_6SH and CoBSH in the MCR substrate channel.

1.3.3 Discussion

The crystal structure of MCR_{Me} is the first structure resembling a postulated intermediate in one of the proposed mechanisms of MCR. The high resolution of the X-ray diffraction data, coupled with anomalous diffraction at several wavelengths, has enabled us to extract the relevant Ni-methyl structure from confounding species. The Ni – C distance refines to 2.07 Å and 2.10 Å in the two crystallographically independent active sites in the asymmetric unit (the distance determined by XAS for MCR_{Me} in solution is 2.04 Å (*28*)). The trend that the methyl position refined towards a longer Ni – C distance than determined by solution XAS could be an indication of partial photoreduction to Ni(II). While there is little or no evidence of photoreduction in the single crystal XAS measurement, photoreduction of Ni(III) to Ni(II) cannot be ruled out in the X-ray diffraction experiment due to the higher dose of X-rays that are absorbed. The absorbed X-ray dose is a 100-fold higher in the native X-ray diffraction experiment (at a fixed energy of 12,674 eV) compared to the single crystal XAS experiment (scanning from 8,300 eV to 8,600 eV). It should be noted that the comparison is a rough approximation since the X-ray beam at the beamline used for single crystal XAS is not as focused as at a typical X-ray diffraction beamline. Also, the temperature was ~50°K lower in the single crystal XAS experiment compared to the X-ray diffraction experiment at a wavelength of 0.98 Å.

While considering photoreduction, the possibility that the electron density assigned to methyl was actually a water molecule bound to photoreduced Ni(II) was explored.

The crystal structure of Ni(II)-MCR containing only 50% HSCoM has been solved to 1.4 Å resolution with 50% CoBSH and 50% CoB_6SH (PDB ID 3M2U) (*55*), which is very analogous to the Ni(III)-methyl crystal structure presented here. In this structure a proximal water lies ~2.0 Å from the Ni(II), and is hydrogen bonded to a "bridging" water that sits in the area between the thiols of $CoB_{(6)}SH$ and HSCoM. In the Ni-methyl crystal structure reported herein, the methyl carbon is 3.5 Å from the bridging water (Figure 1.15) rather than the 2.9 Å observed for water ligated to Ni(II).

Interestingly, MCR is also implicated in "reverse" methanogenesis in the anaerobic oxidation of methane within microbial mats found at methane seeps in the deep ocean (*62, 63*). The dissociation energy of the C – H bond (+439 kJ/mol) is larger than in any other organic compound except benzene. Thauer and Shima have proposed that in "reverse" methanogenesis only the strong electrophile F_{430}-Ni(III) of MCR is capable of breaking the C – H bond in a modified "reversed" version of the Ni(III)-methyl mechanism proposed for methanogenesis (Scheme 1.3A) (*3*). Since no catalytic intermediates of MCR have been observed thus far by fast spectroscopic techniques, any Ni(III)-methyl catalytic intermediate formed from the native substrates must be fleeting during turnover. Recently, transient kinetic methods using the natural substrate methyl-SCoM and the slow substrate analogue CoB_6SH enabled observation of a short-lived Ni(III)-alkyl intermediate and its subsequent decay at catalytically competent rates (*57*). In contrast, when Ni(III)-methyl is artificially generated using methyl iodide, as in this study, it is relatively stable enabling spectroscopic and biochemical characterization (*16, 31*).

The presented crystallographic model contains a mixture of coenzyme B analogue (CoB_6SH, added in crystallization) and CoBSH (co-purifies with the enzyme) that binds in the substrate channel of the enzyme. The respective thiols of CoB_6SH and CoBSH are coincident and situated ~8.7 Å away from the Ni in F_{430} (*55*). As CoBSH is a substrate, the long distance between the thiol and Ni(II) in the previous inactive MCR crystal structures has been puzzling (*6-8, 55*). Thus, a conformational change has been proposed that would bring the CoBSH closer to the Ni (*64*), which is consistent with recent transient kinetic studies revealing substrate-triggered conformational changes in the catalytic resting state MCR_{red1} (*57*). Our data suggest that if Ni(III)-methyl is an intermediate in methane formation, its presence alone does not affect the architecture of the MCR substrate channel, which appears unchanged compared to the structure of the channel in the Ni(II) structures. The active Ni(I) enzyme, its complex with methyl-SCoM, substrate channel conformational changes and true catalytic intermediates trapped during turnover still wait to be structurally defined.

Chapter 2

Hydroxylamine oxidoreductase

The contents of this chapter are reprinted (adapted) with permission from:

Cedervall, P. E., Hooper, A. B. and Wilmot, C. M. (2009) "Crystallization and preliminary X-ray crystallographic analysis of a new crystal form of hydroxylamine oxidoreductase from *Nitrosomonas europaea*", *Acta Crystallogr. Sect. F 65*, 1296-1298.

Cedervall, P. E., Hooper, A. B. and Wilmot, C. M. (*in preparation)* "Structural studies of hydroxylamine oxidoreductase from *Nitrosomonas europaea* reveal a unique heme cofactor and a previously unidentified interaction partner"

2.1 Introduction

The biological oxidation of ammonia is carried out by the anaerobic ammonia-oxidizing (anammox) bacteria ($NH_3 + HNO_2 \rightarrow N_2 + 2H_2O$) and chemolitho-autotrophic ammonia-oxidizing (nitrifying) bacteria ($NH_3 + ½\ O_2 \rightarrow HNO_2 + H_2O$) that have independently evolved ammonia oxidation capabilities (reviewed in (*65, 66*)). Ammonia activation in the absence of molecular oxygen is difficult. Therefore, how the anammox bacteria are able to oxidize ammonia through coupling to nitrite (NO_2^-) reduction, which ultimately leads to the formation of the N_2 triple bond, has long eluded researchers. However, a recent study by Strous and co-workers showed that the initial nitrogen-to-nitrogen bond is formed from ammonia and NO (produced from the reduction of nitrite) in the form of the hydrazine single bond (N_2H_4), which is then oxidized to N≡N (N_2) (*67*). In the aerobic nitrifying bacteria, ammonia is first oxidized to hydroxylamine (NH_2OH) by the enzyme ammonia monooxygenase (AMO) (Scheme 2.1). Hydroxylamine is subsequently oxidized to nitrite through the catalytic action of hydroxylamine oxidoreductase (HAO). Each turnover of HAO yields four electrons which are transferred to the electron transport protein cytochrome c_{554} (Cyt c_{554}) (*68, 69*). Two of HAO's product electrons are substrate electrons for AMO and the other two electrons contribute to the electrochemical gradient through transfer to a terminal oxidase. Ammonia oxidation is rate-limiting in the nitrification process in many diverse environments, making it an important component of global inorganic nitrogen cycling (*70*).

Scheme 2.1 Ammonia oxidation in nitrifying bacteria.

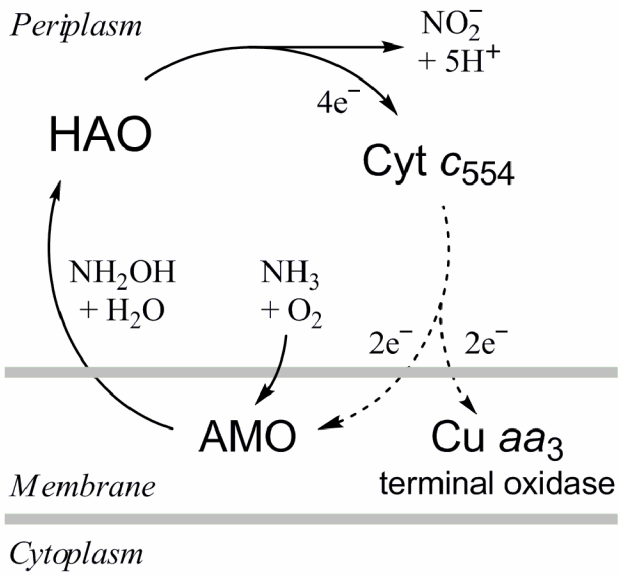

The crystal structure of HAO from *Nitrosomonas europaea* to 2.8 Å resolution showed a predominantly α-helical protein that forms a homotrimer with eight heme cofactors (I − VIII) in each 67.1 kDa [2] monomer, giving a total of 24 hemes in the enzyme (Figure 2.1) (*71*). This makes HAO one of the most complex heme proteins known. Heme cofactors are involved in a range of biological functions, including oxygen transport and storage, gas sensing, gene regulation, catalysis and electron transport (*72, 73*). The heme cofactor consists of a single iron ion bound to an organic component based on the porphyrin macrocycle (Figure 2.2A). The most common type of heme is heme *b* (iron-protoporphyrin IX). This type of heme has methyl groups attached to positions 2, 7, 12 and 18 (following the IUPAC-IUB nomenclature (*74*)), two vinyl

[2] This monomer mass assumes that HAO is the predicted 546 amino acids in length with eight *c*-type hemes attached to the peptide.

Figure 2.1 2.8 Å resolution crystal structure of *N. europaea* HAO (PDB ID 1FGJ). HAO trimer colored by subunit (green, blue and pink) is shown in faded cartoon. Hemes are shown as stick colored by atom (carbon: *c*-type hemes (I – III and V – VIII), light gray; catalytic heme P460 (IV), dark gray). Heme numbering in black is from one subunit and in gray (denoted with ') for neighboring subunits. Fe atoms of hemes are shown as spheres. For simplicity the thioether linkages are not shown.

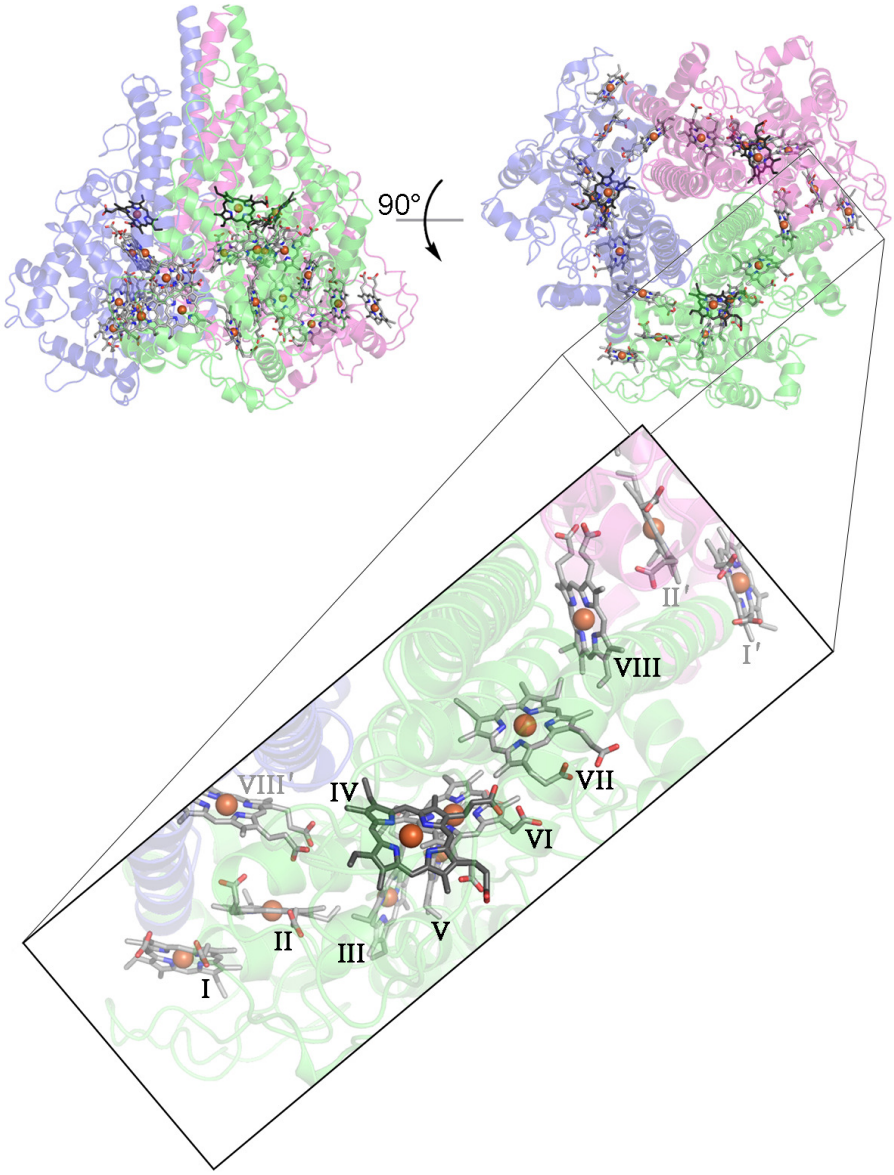

groups at positions 3 and 8, and two propionate groups at positions 13 and 17 (Figure 2.2B). The placement and conformation of heme *b* within proteins is determined solely

Figure 2.2 Drawing of (A) Fe containing porphyrin macrocycle, (B) heme *b* and (C) heme *c*.

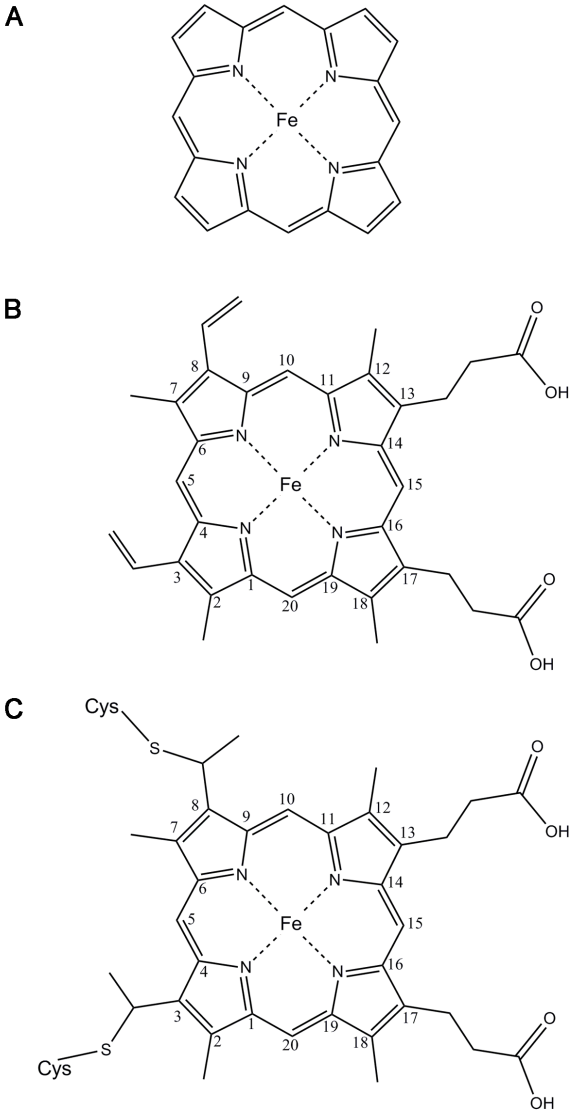

by non-covalent hydrophobic interactions and hydrogen bonds to the surrounding residues. In contrast, heme *c* is covalently attached to the protein through two (or rarely one) thioether bonds involving the sulfhydryl group of two Cys residues (Figure 2.2C). The heme *c* attachment site in proteins is, in most cases, identified by the peptide

sequence Cys-Xaa-Xaa-Cys-His (CXXCH). All commonly occurring amino acids except Cys have been found in the 'XX' segment (*72*). The His residue in the CXXCH motif is almost exclusively the axial (proximal) ligand to the heme Fe, but variations do occur. One such variation is found in octaheme tetrathionate reductase (OTR), where a lysine (Lys56) ligates in preference to the histidine (His78) found in the CXXCH heme attachment motif (*75*). Lys is also found to be a heme ligand in pentaheme nitrite reductase (NrfA) (*76*). However, unlike OTR, NfrA contains an unconventional heme *c* binding motif consisting of a Cys-Xaa-Xaa-Cys-Lys segment, where the Lys serves as the axial heme ligand. Other variants with three (CXXXCH), four (CXXXXCH) and fifteen ($CX_{15}CH$) residues separating the two Cys of the heme binding motif have also been identified (*77, 78*). While unassisted heme *c* incorporation has been reported, incorporation normally requires a specialized biosynthetic system (*79, 80*). Three very different heme *c* incorporating biosynthetic systems have been identified, suggesting a strong evolutionary need for thioether tethered hemes.

Heme *b* is more commonly found in heme enzyme active sites than heme *c* is. Heme *c* is more often associated with electron transfer, with the Fe cycling between the oxidized (ferric) +3 and reduced (ferrous) +2 oxidation states in single electron transfer events. Heme *c* proteins span a significantly larger range of reduction potentials than heme *b* proteins do, enabling them to form a greater redox gradient within the cell. Due to the extensive electronic delocalization of the porphyrin, a heme favors planarity in aqueous solution, but significant deviation often occurs in proteins. The distortion of the porphyrin has influence over the electronic structure of the central Fe atom, and thus also

on the reduction potential of the heme. The normal-coordinate structural decomposition method (NSD), developed by Shelnutt and co-workers (*81, 82*), can be used to analyze the displacement along lowest-frequency normal coordinates, described as *saddling*, *ruffling*, *doming*, *waving* and *propellering* (Figure 2.3). Due to many other factors that can affect the reduction potential of the heme Fe, there is not a clear correlation between the degree of heme distortion and reduction potential. Nevertheless, the attachment of the heme to the polypeptide provides a means by which the reduction potential of the heme can be tuned. The larger reduction potential range of heme *c* could be one evolutionary reason for the need for covalent attachment, while other reasons

Figure 2.3 Illustrations of the lowest-frequency normal coordinates used in describing the nonplanar distortions of the porphyrin macrocycle, described as *saddling*, *ruffling*, *doming*, *waving* ((x) and (y)) and *propellering*. Static displacements representing a 1Å deformation along each lowest-frequency normal coordinate are shown. Reprinted (adapted) with permission from (*81*). Copyright © 1998, Elsevier.

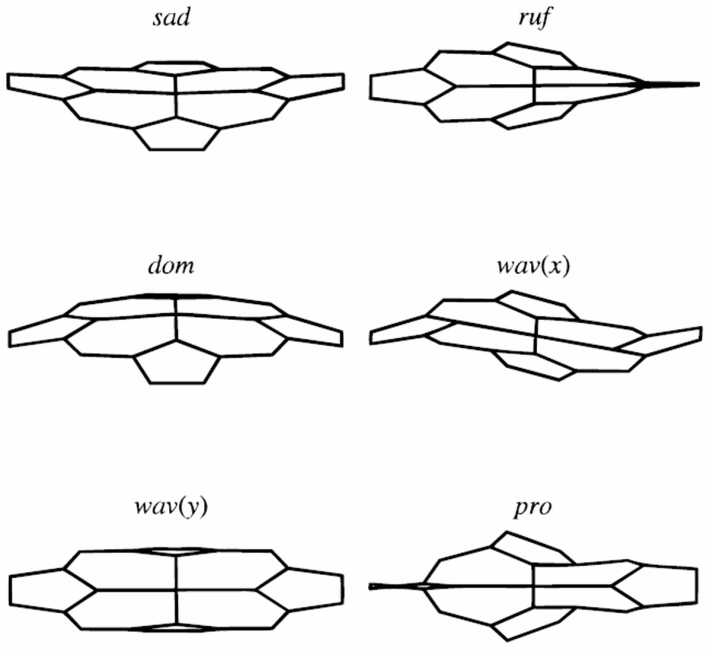

include increased protein stability, enabling a higher ratio of heme groups per unit length of polypeptide chain, and prevention of heme dissociation (*72, 80, 83*). Besides heme *b* and *c*, other iron-porphyrin varieties differing in the number and type of peripheral substituent groups to the porphyrin do exist. These are denoted heme *a*, *d*, d_1, *o*, siroheme and heme P460.

Heme P460 is found in the active site of HAO (*73*). It is notable that the reaction of HAO is the only known biological example of electron removal from a substrate bound to a heme iron (*65*). The other seven of the eight hemes per HAO subunit are *bis*-His coordinated *c*-type hemes, and are involved in transferring the product electrons from the catalytic heme P460 to the physiological electron acceptor protein Cyt c_{554} (*71*). The hemes within each subunit can be divided into clusters (Figure 2.4A) (*71*). The active site heme IV (heme P460) along with hemes VI and VII make up a three-heme cluster. The three hemes are in a parallel stacking arrangement with the plane-to-plane distance between IV – VI and VI – VII close to 4 Å. Heme IV is also hydrogen bonded though its propionate groups to those of heme VI. Heme III and V belong to one out of two double-heme clusters, the other containing heme I and II. In both of these double-heme clusters the two hemes are essentially in a parallel stacking arrangement, again with plane-to-plane distances of about 4 Å. Heme III and V are also hydrogen bonded through one of their propionate groups. The double-heme cluster with heme III and V is closest to the triple-heme cluster, where heme V is interacting with heme VI at a closest distance of 3.7 Å. The two double-heme clusters interact through hemes II and III at a closest contact of 3.5 Å. Heme VIII is considered as the fourth 'cluster' and is essentially perpendicular to

heme VII of the triple-cluster and parallel to heme II' of an adjacent subunit (where ' denotes a heme from an adjacent subunit, Figure 2.1). The closest distance between heme VII and VIII is 3.5 Å. The plane-to-plane distance between heme VIII and II' is 10 Å, but a Trp residue is perpendicularly stacked in between the two hemes and could be aiding in the transfer of electrons between subunits. The distance from the Trp to both heme VIII' and II is about 3.6 Å. Also, the propionate groups of hemes I and II are involved in trimer formation by hydrogen bonding to the peptide of an adjacent subunit, and one of the propionates of heme II is hydrogen bonding to the proximal His of heme VIII'. It is also interesting to note that the hemes within the double- and triple-clusters have a methyl carbon only 3.2-3.9 Å away from the side chain of the proximal His of the other heme(s) within the cluster, and that the highest numbered heme from one cluster has an ethyl carbon only 3.4-4.1 Å from the distal His of the lowest numbered heme of the next cluster. Clearly, the arrangement of the hemes in HAO is set up for facile electron transfer within and between subunits (*84*).

Besides the active site heme P460, heme I is the only heme exposed to solvent. Therefore, heme I has been proposed as the electron exit site. This is also supported by an HAO − Cyt c_{554} complex docking model reported by Rees and co-workers that solved the crystal structure of Cyt c_{554} (*85, 86*). Cyt c_{554} contains four *c*-type hemes: heme 1-4. Heme 1, 3 and 4 are *bis*-His coordinated and heme 2 is penta-coordinate, with the His in the heme binding motif as the proximal ligand. It is noteworthy that heme 1 in Cyt c_{554} is the only known example of where the His is coordinated to the Fe atom through N_δ rather than through N_ε. The surface geometry and vacuum electrostatics in the region of hemes

I of HAO are complementary to that of Cyt c_{554}, suggesting that each HAO molecule forms a complex with three Cyt c_{554} molecules, and that the electrons are transferred to Cyt c_{554} through heme I. In the HAO − Cyt c_{554} complex model, the intermolecular Fe − Fe distance from heme I of HAO and heme 1 of Cyt c_{554} is close to 20 Å, and a closest distance of 8 Å between the heme porphyrins (*86*). Within the theoretical model, these are the two hemes that approach closest between the two proteins.

It is proposed that the hydroxylamine oxidation pathway evolved from a nitrite reduction pathway found in anaerobic respiration (denitrification), and that the HAO enzyme evolved from the pentaheme cytochrome *c* nitrite reductase (NrfA) (*87, 88*). The three dimentional arrangement of the five hemes in NrfA are very similar to that of hemes IV-VIII of HAO, with the NrfA active site heme corresponding to heme P460 (Figure 2.4B). As an octaheme nitrite reductase (ONR) exists today, it has been suggested that the three additional hemes were acquired prior to the change in function in the evolution of HAO (*88*). All eight hemes of ONR can be superimposed on the hemes of HAO (Figure 2.4C). Another octaheme enzyme that is proposed to have evolved from NrfA is octaheme tetrathionate reductase (OTR) (*87, 88*). In three dimensions, there are two ways to align the hemes of OTR with those of HAO. One possibility is to align hemes 1 and 3-8 with that of hemes I-III and V-VIII of HAO (Figure 2.4D). In this orientation, the active site heme 2 of OTR is on the opposite side of the string of hemes to that of the HAO active site heme P460. Hemes 1-6 of ONR can also be aligned with hemes III-VIII of HAO (Figure 2.4E). This orientation is a better functional and sequential fit to HAO, as it leaves the order in heme numbering (which is based on

position in the primary structure) the same as that of HAO, with the OTR active site heme 2 now corresponding to heme P460 (heme IV) of HAO.

Respiratory nitrite ammonification by NrfA is found in the γ- δ- and ε-subclass of the protobacteria (*89*). In the γ-protobacteria, such as *Escherichia coli*, NrfA exist as a soluble homodimer that forms a transient complex with two molecules of the pentaheme electron donor protein NrfB (*90, 91*). A model for the NrfA – NrfB interaction has been proposed, and in this model hemes 3-5 of NrfB and the five hemes of NrfA completely account for all eight hemes in HAO (Figure 2.5A). The five hemes of NrfB can also be superimposed on hemes I-III, V and VI (Figure 2.5B), or alternatively hemes III and V-VIII, of HAO (Figure 2.5C). In the δ- and ε-protobacteria, NrfA interacts with the membrane anchored tetraheme electron donor protein NrfH (*89*). The stable $NrfA_4$ – $NrfH_2$ complex crystal structure has been solved, and the NrfH interaction site is different from that proposed for NrfB (*92*). The four hemes of NrfH can be superimposed on hemes III and V-VII of HAO (Figure 2.5D). The hemes of Cyt c_{554} can also be superimposed on HAO, with Cyt c_{554}, hemes 1-4 corresponding to hemes III-VI of HAO (Figure 2.5E). Interestingly, penta-coordinate heme 1 of Cyt c_{554} is in the equivalent spatial position of the active site hemes of HAO and NrfA. Heme 1 of NrfH is also a penta-coordinate heme, but unlike in Cyt c_{554}, this site does not correspond to the active sites of HAO and NrfA (Figure 2.5D). Despite this, 93 of the 158 residues in NrfH can be structurally aligned with Cyt c_{554} (16% identity). There is an insertion of 56 residues in Cyt c_{554} that binds heme 2, which corresponds to the heme IV of HAO (Figure 2.6 and

Figure 2.4 Monomer heme arrangement in (A) HAO, (B) NrfA, (C) ONR, (D) OTR (conformation 1) and (E) OTR (conformation 2).

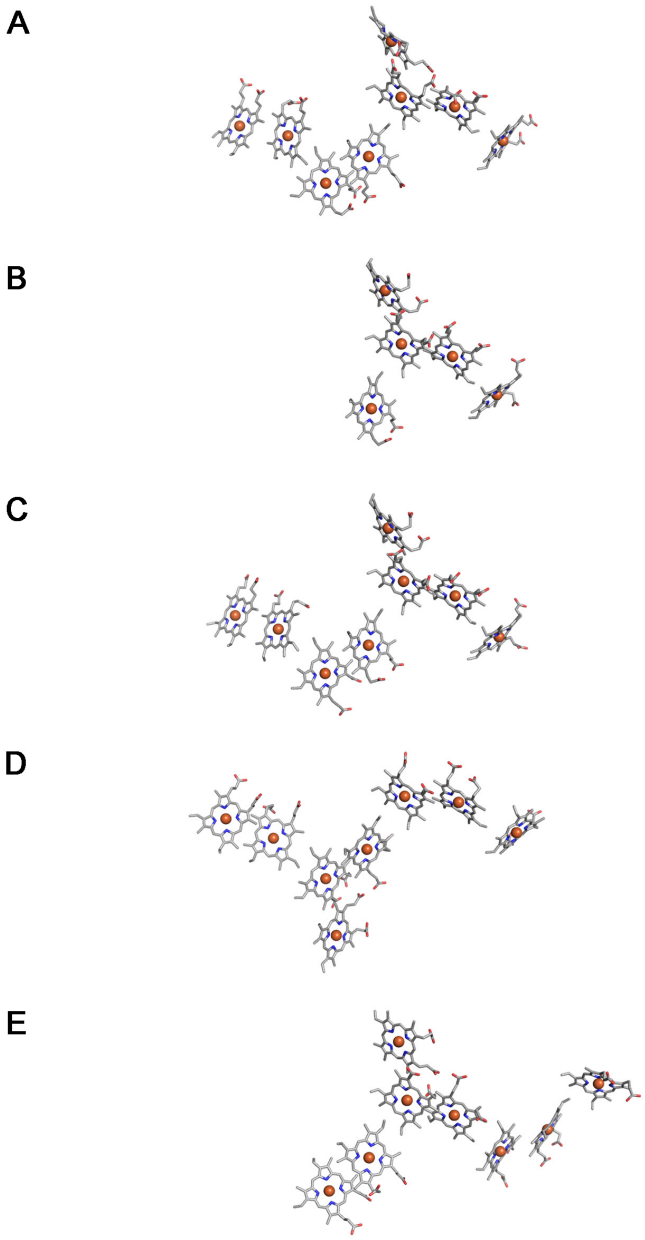

Figure 2.5 Monomer heme arrangement in (A) HAO, (B) proposed NrfAB complex (C) NrfB (conformation 1), (D) NrfB (conformation 2), (E) NrfH and (F) Cyt c_{554}.

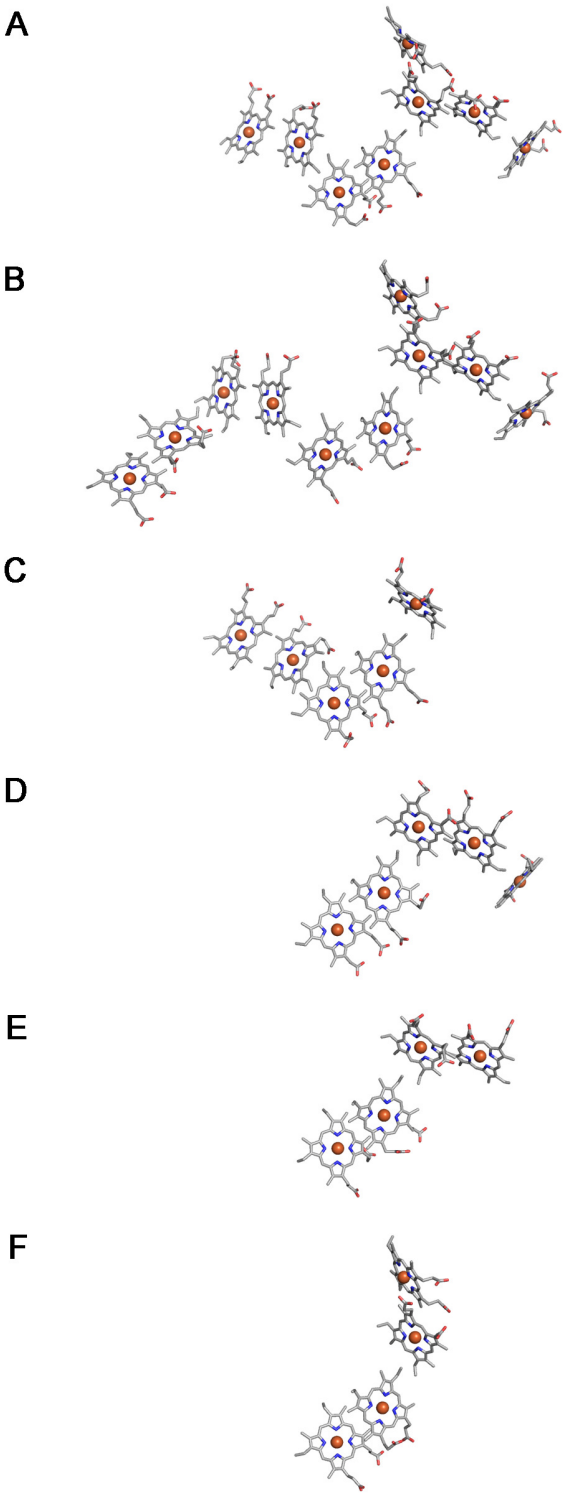

Figure 2.7). The structure is conserved around the binding site of heme 4 of NrfH, but the Cyt c_{554} lacks the CXXCH motif and therefore the heme in this location (Figure 2.7). Although a possible evolutionary relationship exists amongst the proteins discussed above, the near perpendicular stacking of heme clusters have been found to be conserved in other multi-heme cytochromes highly diverse in function. This so-called 'heme elbow motif' may reflect the most favorable heme – heme interactions suited to electron transfer between hemes, and may have evolved independently multiple times (*86*).

Figure 2.6 Cyt c_{554} (yellow) and NrfH (green) overlay. The proteins are shown as faded cartoons (termini indicated by spheres). Hemes are shown in stick format with the Fe atom as a sphere in the same color as the respective protein. The top green heme is heme 4 in NrfH. The far left yellow heme is heme 2 in Cyt c_{554}.

Figure 2.7 Sequence representation of structural alignment of Cyt c_{554} and NrfH. The insertion that holds heme 2 in Cyt c_{554} is in bold (heme binding motif underscored) and the heme binding motif of heme 4 in NrfH is underscored and highlighted in green.

```
DSSP    ----------------lLLLL--LLHHHHHH--LHHHHHHHLLLLHHhllhhhlllllhh
Cyt c554 ----------------dAPFE--GRKKCSSC--HKAQAQSWKDTAHA**kameslkpnvkke**   40
ident                          |  | ||          |   ||
NrfH    vlggatlgvvalatvafGMKYtdQRPFCTSChiMNPVGVTHKLSGHA-------------   47
DSSP    llllhhhhllhhhhhhhHHHHllLHHHHLLLhhHHHHHHHHHHLLLL-------------


DSSP    hhhhlllllllllllllllhhhlllllllllllllllllhhhlLLLHHHHHL--------
Cyt c554 **akqkakldpakdytqdkd<u>cvgch</u>vdgfgqkggytiespkpmlt**GVGCESCHG--------   92
ident                                                  |  ||
NrfH    ---------------------------------------------NISCNDCHAphnllakl   64
DSSP    ---------------------------------------------LLLLHHHHLlllhhhhh


DSSP    -lLLLLHHHHHHHHHHHHhhllleehhhhhhllLLLL-LHHHHHHHHLL-LLLLLLllll
Cyt c554 -pGRNFRGDHRKSGQAFEksgkktprkdlakkgQDFH-FEERCSACHLN-YEGSPWkgak  149
ident                                              | |||
NrfH    pfKAIAGARDVYMNTLGH------pgdlilagmETKEvVNANCKACHTMtNVEVAS----  114
DSSP    hhHHHHHHHHHHHHHLLL------llllllllhHHHHhHHHHHHHHHHHhHLLLLL----


DSSP    lllllllllllhhhllLHHHhLLLLlLLLLLlllllleellllllhhhhhhlLLLL-LL
Cyt c554 apytpftpevdakytfKFDEmVKEVkAMHEHyklegvfegepkfkfhdefqasAKPA-KK  208
ident                          |
NrfH    ----------meakkY<u>CTD-CH</u>RN-VQHMR---------------------mKPIStRE  140
DSSP    ----------llllLHHH-LLHH-HLLLL---------------------lLLHHhLL
```

The catalytic heme IV in HAO is named heme P460 based on the λ_{max} of its ferrous UV-visible absorption Soret band (*93*). Although heme P460 has unique and unexplained resonance Raman, EPR and Mössbauer properties, these data support the ferric state as being high-spin (*94, 95*). Resonance Raman spectroscopy was consistent with either a model in which two of the pyrroles are reduced, or alternatively a model with an additional ring and 1-2 reduced pyrroles. The Mössbauer spectrum of reduced heme P460 exhibits a quadrupole splitting (ΔE_Q) of 4.21 mm/s, which is unusually large for a ferrous heme protein. Based on mass spectrometry and nuclear magnetic resonance (NMR) spectroscopy of proteolyzed HAO fragments, the unusual spectral properties of

heme P460 were assigned to be the result of a third crosslink between the porphyrin and the protein (*93*). The mass spectrometry data indicated that there was a net loss of two protons from the connected peptides. Based on the NMR data, it was concluded that one of the two protons originated from an aromatic carbon of the tyrosyl ring, and the other proton from C5 of the porphyrin ring. When the crystal structure of HAO was solved, this single additional crosslink was modeled between the Tyr-C3 and porphyrin-C5 positions (Figure 2.8) (*71*). The crystal structure also revealed that this Tyr residue was from the adjacent subunit, thereby covalently linking the three monomers of HAO together (*71*). However, a closer examination of the X-ray crystallographic model reveals a serious steric clash between the hydroxyl group of the crosslinked Tyr and atoms of the porphyrin ring. Also, the porphyrin-C5 is sp^2 hybridized in the model put forth based on proteolysis mass spectrometry and NMR data (*93*), whereas the

Figure 2.8 Single crosslink heme P460 model. (A) Drawing of heme P460 and (B) structural model of heme P460 from the 2.8 Å resolution crystal structure of *N. europaea* HAO (PDB ID 1FGJ) protein is shown as faded cartoon colored by subunit (green and blue). Hemes and amino acids are shown as stick colored by atom (carbon: amino acids, as subunit; *c*-type hemes (VI and VIII'), light grey; catalytic heme P460 (IV), dark grey).

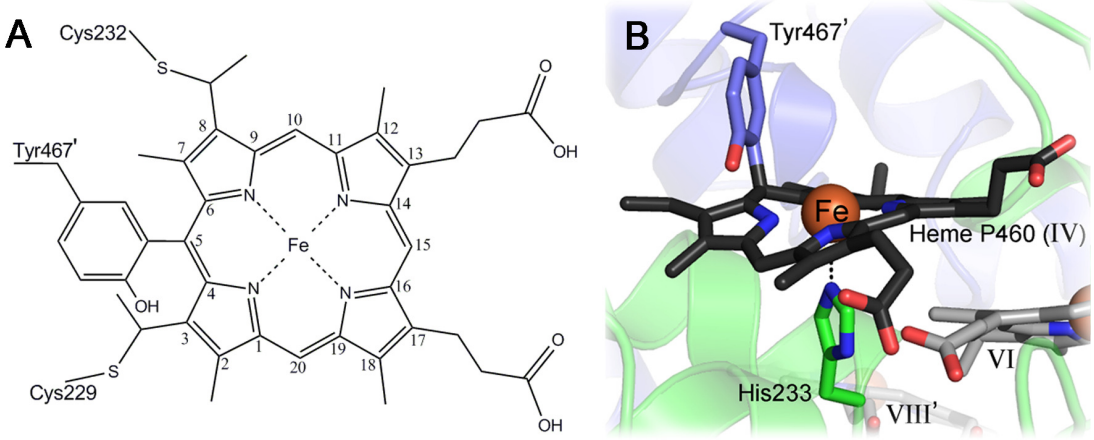

crystallographic model is indicative of C5 being a sp^3 hybridized center (PDB ID 1FGJ (*71*)). This prompted us to reassess the current model, using a new HAO crystal form, to help resolve the identity of the crosslink found in heme P460 of HAO (Chapter 2.2). The new crystal form also revealed that HAO forms a complex with a protein that was identified as NE1300 within the *Nitrosomonas europaea* genome. This chapter also describes a crystal structure of HAO in complex with the hydroxylamine substrate (Chapter 2.3).

2.2 Structural studies of hydroxylamine oxidoreductase from *Nitrosomonas europaea* reveal a unique heme cofactor and a previously unidentified interaction partner

Ammonia oxidation is rate-limiting in nitrification, making it an important component of global inorganic nitrogen cycling. In aerobic environments, ammonia oxidation is carried out by autotrophic ammonia oxidizing (nitrifying) bacteria. Within this group of bacteria the enzyme hydroxylamine oxidoreductase (HAO) catalyzes the second step of ammonia oxidation: the four-electron oxidation of hydroxylamine to nitrite. Each subunit in the homotrimeric HAO molecule contains seven regular *c*-type heme cofactors and one highly unusual heme P460 that is the site of catalysis. Analysis by mass spectrometry and NMR proposed heme P460 to be a *c*-type heme with an additional protein crosslink to the porphyrin from a Tyr. Until now, only a single X-ray crystallographic structure of HAO (to 2.8 Å resolution) had been reported. The heme P460 crystal structure model was built such that it emulated the proposed chemical model, despite the fact that there were structural indications that this model was incorrect. To resolve this discrepancy, we have produced a new crystal form of HAO and collected data to 2.1 Å resolution. The data indicate that the heme P460 crosslink is indeed different from the original proposal in that it contains two crosslinks to the Tyr. Additionally, the HAO had been purified from source (*Nitrosomonas europaea*), and a small polypeptide was found bound to each subunit. The identity of this peptide was determined by N-terminal sequencing and mass spectrometry to be a hypothetical protein

of unknown function in the *N. europaea* genome.

The contents of this section are reprinted (adapted) with permission from:

Cedervall, P. E., Hooper, A. B. and Wilmot, C. M. (2009) "Crystallization and preliminary X-ray crystallographic analysis of a new crystal form of hydroxylamine oxidoreductase from *Nitrosomonas europaea*", *Acta Crystallogr. Sect. F 65*, 1296-1298.

Cedervall, P. E., Hooper, A. B. and Wilmot, C. M. (*in preparation)* "Structural studies of hydroxylamine oxidoreductase from *Nitrosomonas europaea* reveal a unique heme cofactor and a previously unidentified interaction partner"

2.2.1 Methods

Expression, purification and crystallization. The expression and purification of HAO from *Nitrosomonas europaea* was carried out as previously described (*96*). Briefly, *N. europaea* cells were disrupted by freeze–thawing (from -10°C to 4°C). The resulting cell homogenate was centrifuged at 20,000×g for 20 min and the supernatant was fractionated with ammonium sulfate. The 60-80% saturated ammonium sulfate precipitate was re-suspended in 50 mM potassium phosphate pH 7.5, and then dialyzed against 10 mM potassium phosphate pH 7.5. This was then subjected to a Sephadex G-100 column, equilibrated with 200 mM potassium chloride, 50 mM potassium phosphate pH 7.5. The fractions containing HAO were concentrated by ultracentrifugation and loaded onto a Sepharose CL-6B column, equilibrated with 200 mM potassium chloride, 50 mM potassium phosphate pH 7.5. The second gel-filtration chromatography step was followed by ion exchange chromatography on a DEAE-Sephacel column equilibrated with 20 mM Tris-Cl, pH 8.1. Homogeneous HAO was eluted with a 0-300 mM sodium chloride gradient. The protein was stored at -80°C for 13 years before being thawed and used for crystallization. Before crystallization, the protein was buffer exchanged into 20 mM Hepes-Na pH 7.0 using an Amicon Ultra Centrifugal Device (Millipore) with a cut-off of 100 kDa. After buffer exchange the protein was concentrated to 28 mg/ml, as determined with Bradford reagent (Sigma).

High throughput crystallization trials were done through the Hauptman-Woodward Medical Research Institute. The initial screen contained 1536 unique

conditions, using the crystallization method microbatch-under-oil, with equal amounts (0.2 µl) of protein and crystallization cocktail, at room temperature. The crystallization condition that was chosen for later optimization contained 0.1 M potassium nitrate (KNO_3), 0.1 M MES pH 6.0 and 40% (v/v) PEG 400. Optimization of pH and PEG 400 concentration around this condition was done at 20°C in Microbatch 72 Well Plates (Hampton Research), with equal amounts (2 µl) of protein and crystallization cocktail, under 10 µl of paraffin oil. A single crystal was washed in two successive 8 µl drops of the crystallization solution, and then flash frozen in liquid nitrogen in a 0.2-0.3 mm CryoLoop mounted on a CrystalCap Magnetic base (both from Hampton Research). No additional cryoprotectant was needed.

X-ray diffraction data collection, processing and analysis. X-ray diffraction data collection was carried out at the Structural Biology Center (SBC) beamline 19-ID-D at the Advanced Photon Source (APS), Argonne National Laboratory. 120 degrees of data were collected from a single crystal using an ADSC-CCD detector and a 100 x 100 µm beam. Data collection was done at cryogenic temperatures (100°K). The data were processed with HKL2000 (*51*).

Data analysis, model building and refinement. Analysis of the scaled diffraction data was carried out using programs in the Collaborative Computational Project Number 4 (CCP4) suite (*97*). Initial phases were generated with Phaser, using one monomer from the previously determined crystal structure (PDB ID 1FGJ) as the search model, but with

all non-polypeptide molecules removed (*71*). The X-ray diffraction data used in Phaser were scaled as P222, and all space groups in this point group were tested by the program. The diffraction images were then re-processed to the space group of the best solution ($P2_12_12$). To minimize model bias, Tyr467' (where ' denotes the Tyr being from an adjacent subunit) involved in the protein − heme P460 crosslink was truncated to Ala. In the early stages of refinement, the seven regular *c*-type hemes per subunit were included in the model with the thioether links restrained to 1.84 Å. Once refinement of the HAO model was almost complete, regular *c*-type hemes were placed in the electron density at the expected heme P460 sites and residue 467' converted back to Tyr. The heme P460 library file for use in refinement was created using Library Monomer Sketcher in the CCP4 suite. Tyr467′-C3 – porphyrin-C5 and Tyr467′-O – porphyrin-C4 links were restrained to 1.47 Å and 1.50 Å, respectively. The protein − heme P460 thioether links were restrained to 1.84 Å, as expected for regular *c*-type hemes. Model building and generation of non-crystallographic symmetry (NCS) maps were done in the Crystallographic Object-Oriented Toolkit (COOT) (*53*). For refinement, REFMAC in the CCP4 suite was used (*59*). A random sample of 5% of the data across all resolution shells was chosen as an unbiased check to track refinement through calculation of an R_{free}. The remaining 95% of the reflections were used in refinement (R_{work}). At the later stages of refinement TLS refinement (with two TLS groups) was introduced (*98*).

Model analysis. Structural alignments were done in PyMOL (*60*). The displacements along the lowest-frequency normal coordinates of the porphyrin macrocycle of heme

P460 were analyzed using the on-line normal-coordinate structure decomposition (NSD) engine, version 3.0, at http://jasheln.unm.edu/jasheln/content/nsd/NSDengine/start.htm (*81, 82*). Heme P460 was, as recommended for all protoporphyrin IX (*b*-type heme) related molecules, oriented so the substituent ethyl groups are in quadrants I and II in the Structure Window in the NSD program. The surface area of NE1300 in the NE1300 − HAO interface (area of NE1300 within 4 Å of HAO) was calculated using PyMOL (*60*). The type of inter-molecular interactions present at the interface was established using the protein interactions calculator (PIC) server at http://crick.mbu.iisc.ernet.in/PIC/cgi/submit_job.cgi (*99*).

N-terminal sequencing and mass spectrometry. N-terminal sequencing was done at the Oligonucleotide & Peptide Synthesis Facility, BioMedical Genomics Center at the University of Minnesota. The sample was separated in a 12% Bis-Tris SDS-PAGE gel, and blotted onto a Sequi-Blot PVDF membrane. The membrane was stained using a solution of 0.1% Amido Black, 40% methanol and dH_2O. The band on the PVDF membrane thought to correspond to the HAO binding partner observed in the electron density, was cut out and analyzed through 10 cycles of Edman degradation, followed by reverse-phase HPLC. In-gel proteolysis (trypsin), followed by mass spectrometric analysis, was carried out at Taplin Biological Mass Spectrometry Facility, Harvard Medical School. The bands sent for in-gel proteolysis / mass spectrometry were generated in a 4-12% Bis-Tris SDS-PAGE gel for the HAO trimer, and a 12% Bis-Tris

SDS-PAGE gel for the HAO binding partner. The gels were stained with SimplyBlue™ SafeStain (Invitrogen).

Primary sequence analysis. Transmembrane helix prediction in HAO was done using TopPred at http://mobyle.pasteur.fr/cgi-bin/portal.py?form=toppred (*100, 101*). To identify the protein binding partner to HAO, the results from the N-terminal sequencing and mass spectrometry were analyzed using blastp (protein-protein BLAST) at http://blast.ncbi.nlm.nih.gov/Blast.cgi.

2.2.2 Results

The crystallization condition that produced crystals used for X-ray diffraction data collection contained 0.1 M potassium nitrate (KNO_3), 0.1 M MES pH 7.5 and 46% (v/v) PEG 400. Small plate-shaped crystals appeared in a matter of days and grew to a final size of ~200 μm in length within two weeks (Figure 2.9). The data were indexed as orthorhombic with unit cell parameters a = 140.7, b = 142.6 and c = 107.4 Å. Unlike the previously reported HAO crystal form in space group $P6_3$, no merohedral twinning was detected for the $P2_12_12$ crystal form. The average B-factor derived from a Wilson plot of the scaled data is 32.7 $Å^2$ (*102*). The X-ray data collection and processing statistics are summarized in Table 2.1.

Figure 2.9 Picture of HAO crystals grown in 0.1 M potassium nitrate (KNO_3), 0.1 M MES pH 7.5 and 46% (v/v) PEG 400.

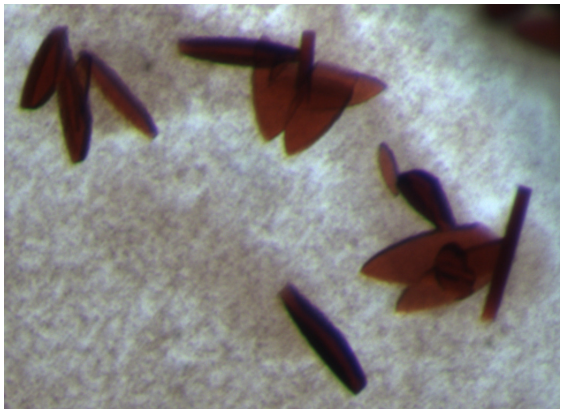

Table 2.1 X-ray diffraction data collection, processing and refinement statistics

Data collection and processing statistics	
unique reflections	109103
Redundancy [a]	4.6
resolution (Å) [a]	50.0-2.10 (2.14-2.10)
completeness (%) [a]	86.7 (69.3)
R_{merge} (%) [a, b]	12.7 (57.4)
I/σI [a]	9.6 (2.0)
space group	$P2_12_12$
Refinement and model building statistics	
resolution (Å)	42.9-2.10 (2.16-2.10)
no. of reflections in working set	95555 (4625)
no. of reflections in test set	5071 (248)
R_{work} (%) [c]	16.5
R_{work} (%) [d]	20.6
ESU (Å) R_{work}/R_{free}	0.251/0.189
no. protein atoms	13133
no. ligand atoms	1279
no. water molecules	785
RMS	
bond length (Å)	0.023
bond angle (deg.)	2.102
Ramachandran plot (%)	
favored	96.7
allowed	3.3
average B-factor (Å^2)	
protein	37.3
ligands	56.4
waters	40.3
overall	37.3

[a] Values in parentheses correspond to the highest resolution shell.
[b] $R_{merge} = \Sigma_{hkl}\Sigma^{N}_{j=1}|I_{hkl}-I_{hkl}(j)|/\Sigma_{hkl}N*I_{hkl}$, sum over all reflections and all observations N, with $I_{hkl}(j)$ intensity of the j^{th} observation of reflection hkl and I_{hkl} mean intensity of the reflection hkl.
[c] $R_{work} = \Sigma||F_o| - |F_c||/ \Sigma|F_o|$, where $|F_o|$ = observed structure factor amplitude and $|F_c|$ = calculated structure factor amplitude.
[d] R_{free}, R-factor based on 5% of the data excluded from refinement.

Cell content analysis (Matthews) indicated that three monomers (one HAO homotrimer) were present in the asymmetric unit with a solvent content of 54% (*103*). The strongest solution found for the automated search was for space group $P2_12_12$, placing three monomers in the asymmetric unit (ASU). Rigid body refinement using the homotrimeric model located by Phaser gave initial *R*-values of 29% for both R_{work} and R_{free}. All the expected heme binding sites showed strong positive Fo-Fc electron density,

signifying the correctness of the solution.

Electron density that could not be explained by the HAO molecule was detected next to the HAO trimer (Figure 2.10). The electron density was clearly protein derived, and a poly-Ala model of 42 amino acids was built into the electron density. SDS-PAGE of both the protein sample and dissolved crystals revealed the presence of a small polypeptide with an estimated molecular weight of ~7 kDa, in addition to that of the 189 kDa HAO (Figure 2.11). The 7 kDa band was excised from the SDS-PAGE gel and subjected to N-terminal sequencing, which gave the sequence *SGNLESSLAP*. A primary sequence database search indicated that the protein sequence belongs to a 69 residue hypothetical protein NE1300 in *N. europaea* (RefSeq protein accession number:

Figure 2.10 Unexplained electron density around the HAO trimer. HAO trimer is shown as faded cartoon and colored by subunit (pale green, light blue and light pink). Hemes are shown as stick colored by atom (carbon: *c*-type hemes, light gray; catalytic heme IV (heme P460), dark gray). 2Fo-Fc electron density contoured at 1σ is shown as blue mesh, Fo-Fc electron density contoured at 5σ is shown as green mesh.

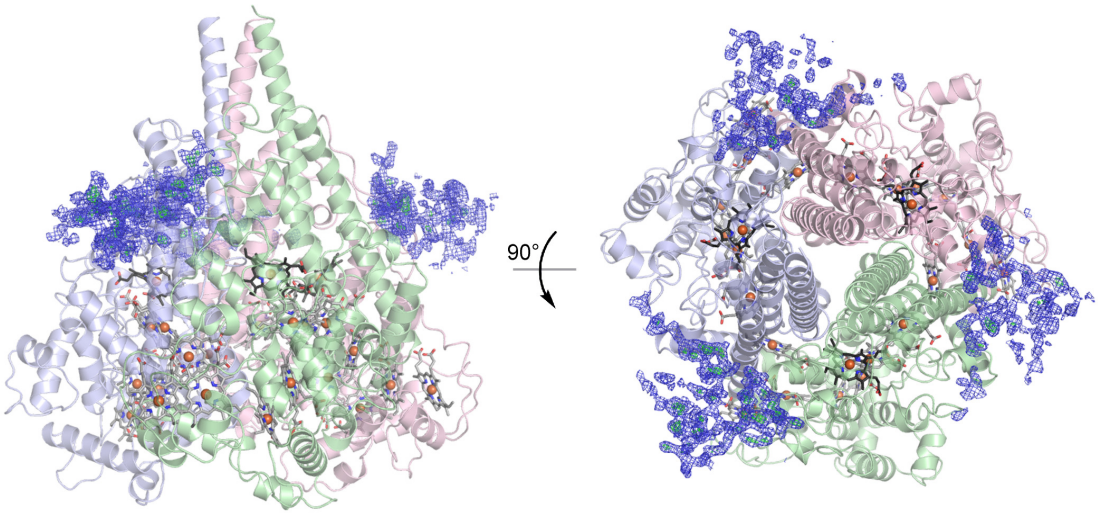

Figure 2.11 SDS-PAGE gel of sample used for crystallization and dissolved HAO crystals.

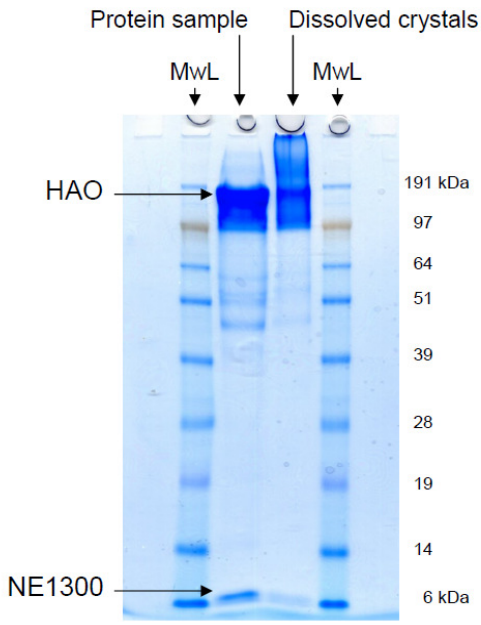

NP_841349). The gel-band was also analyzed through proteolysis coupled to mass spectrometry, which confirmed the candidate protein as NE1300. Peptide fragment coverage was ~50% of the NE1300 protein sequence (residues 33-69) (Table 2.2 and Figure 2.12). As well as N-terminal sequencing and proteolysis / mass spectrometry of the ~7 kDa gel-band, the identity of NE1300 as the HAO binding partner was additionally corroborated by proteolysis / mass spectrometry of the HAO gel-band. Despite the denaturing conditions of SDS-PAGE, NE1300 was also detected in the HAO gel-band, consistent with a tight binding interaction between the two proteins (Table 2.3 and Figure 2.13). The N-terminal sequencing, along with the peptide coverage from the mass spectrometry, indicates that it is the mature full-length NE1300 that is present in the sample. Once the primary sequence was known, it could be matched to the order of the

Table 2.2 Peptide fragments belonging to NE1300 (RefSeq protein accession number: NP_841349) detected in proteolysis mass spectrometry of SDS-PAGE band thought to contain the identified binding partner. Position numbering includes predicted leader sequence.

MH+	Position	Sequence
1198.1906	81-91	EQSGDAWQGGY
1273.5768	67-78	VKCGDIVALVQK
1369.5205	55-66	SHTEVENGKIVR
1425.4569	79-91	AREQSGDAWQGGY

Figure 2.12 Sequence coverage of fragments detected in proteolysis mass spectrometry of the SDS-PAGE band thought to contain the identified binding partner. The NE1300 (RefSeq protein accession number: NP_841349) sequence covered by the detected peptide fragments is underscored and highlighted in green. The predicted leader sequence is highlighted in red.

MNKVIVAAFV SAFVLGSTAT FASGNLESSL APISAKDMLD YLACKDKKPT
DVVKSHTEVE NGKIVRVKCG DIVALVQKAR EQSGDAWQGG Y

Table 2.3 Peptide fragments belonging to NE1300 (RefSeq protein accession number: NP_841349) detected in proteolysis mass spectrometry of HAO SDS-PAGE band. Position numbering includes predicted leader sequence.

MH+	Position	Sequence
786.9470	48-54	KPTDVVK
1001.0410	55-63	SHTEVENGK
1030.2097	46-54	DKKPTDVVK
1046.2701	69-78	CGDIVALVQK
1072.2795	37-45	DMLDYLACK
1374.5338	23-36	SGNLESSLAPISAK

Figure 2.13 Sequence coverage of NE1300 fragments detected in proteolysis mass spectrometry of the HAO SDS-PAGE band. NE1300 (RefSeq protein accession number: NP_841349) sequence covered by the detected peptide fragments is underscored and highlighted in green. The predicted leader sequence is highlighted in red.

MNKVIVAAFV SAFVLGSTAT FASGNLESSL APISAKDMLD YLACKDKKPT
DVVKSHTEVE NGKIVRVKCG DIVALVQKAR EQSGDAWQGG Y

side chains observable in the electron density, giving final confirmation that NE1300 was the additional protein in the crystal. Using NCS averaged electron density maps, 49 out of the 69 residues (residues 7-55) could be modeled in the three equivalent copies of NE1300. The protein – protein interface between HAO and NE1300 is mainly hydrophobic in nature, with an interaction surface of about 1000 $Å^2$; close to 25% of the total surface area of NE1300 visible in the electron density.

The final HAO – NE1300 model refined with R_{work} and R_{free} of 16.5 and 20.6%, respectively. All amino acids were in allowed regions of the Ramachandran plot (favored 96.7%, allowed 3.3%). Model refinement statistics are shown in Table 2.1. The atomic coordinates and the structure factors have been deposited in the Protein Data Bank as PDB ID 4FAS.

The higher resolution crystal structure of this study confirms the presence of a crosslink between Tyr467′-C3 – porphyrin-C5, but also the presence of an additional carbon − oxygen bond between the Tyr467′-O of the side-chain and C4 of the porphyrin (Figure 2.14). The Tyr467′-C3 – porphyrin-C5 and hydroxyl Tyr467′-O – porphyrin-C4 links refine to a average distance of 1.5 Å across the three NCS-related active sites in the ASU. The model that best fits the electron density has sp^3 hybridization at the C4 and C5 atoms of the porphyrin, leading to disruption of the aromaticity. The new model for heme P460 shows a severe distortion of the porphyrin ring, even more so than the previously proposed single crosslink model (*71, 104*). Quantitative analysis using the NSD engine revealed that the main contribution to the deformation is *ruffling* (Figure 2.3) with an average distortion of 2.2 Å (old model, 1.5 Å). The other deformation modes,

saddling, doming, waving (*x* and *y*) and *propellering*, (Figure 2.3) all have minor distortion contributions (±0.1-0.4 Å).

Figure 2.14 HAO active site heme P460 double crosslink model. A) Stereo view of heme P460 seen from the entrance to the active site pocket. B) Close-up view of the heme P460 – Tyr double crosslink. Protein is shown as faded cartoon colored by subunit (pale green and light blue). Hemes and amino acids are shown as stick colored by atom (carbon: amino acid side chains, as subunit (green and blue); heme VI, light gray; heme P460 (IV), dark gray). Fe of hemes are shown as brown spheres. Fe coordinating water molecule is represented by a red sphere. 2Fo−Fc electron density contoured at 1σ is shown as blue mesh. C) Drawing of heme P460 (IV).

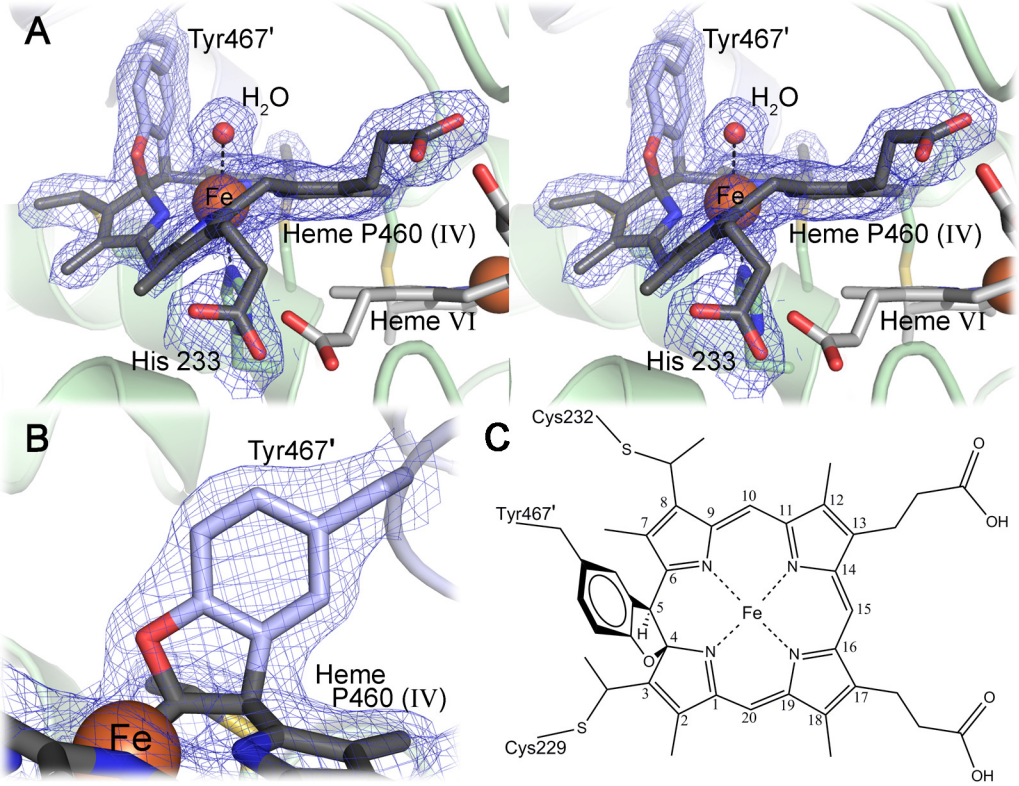

The proteolysis / mass spectrometric analysis of the HAO SDS-PAGE band detected no peptides containing residues beyond residue Ser507 in the HAO sequence (expected C-terminus at residue 546; Table 2.4 and Figure 2.15).

Table 2.4 Peptide fragments belonging to HAO (Swiss-Prot accession number: Q50925) detected in proteolysis mass spectrometry of HAO SDS-PAGE band. Position numbering includes predicted leader sequence.

MH+	Position	Sequence
567.6195	322-326	DAFSK
733.8608	306-311	LAEMNR
752.8051	59-66	DPAHGAGK
787.9346	522-528	VNKLEGK
788.9193	403-410	GTLEGLAK
808.9530	320-326	LKDAFSK
814.8736	180-186	DKADHTK
850.0209	154-161	SMGKLGEK
885.9523	121-128	STHANLDK
953.0802	48-55	ETYEALVK
985.1401	395-402	SYLDLMDK
1001.0808	134-141	SDDPLYYK
1034.0734	270-278	HEFSAAESR
1042.1398	120-128	RSTHANLDK
1043.1648	456-465	GNNPASLELK
1044.1552	57-66	YKDPAHGAGK
1104.2486	522-531	VNKLEGKQTS
1116.2162	145-153	LEEVENNLR
1129.2549	134-142	SDDPLYYKK
1133.2517	312-319	DKWNWEVR
1147.3348	512-521	MQELSALQAR
1155.2992	121-130	STHANLDKIR
1173.3140	411-420	YQEANAIVHK
1200.3427	56-66	RYKDPAHGAGK
1232.4375	466-476	VLEMAENNLAK
1243.3741	421-431	MYEDGTLTGQK
1279.3953	432-442	TNRPNPPEPEK
1301.4422	143-153	GKLEEVENNLR
1350.5549	44-55	ATPKETYEALVK
1359.4755	501-511	AYVEIQDEYTK
1528.7936	443-455	PGFGIFTQLFWSK
1567.6899	25-38	DISTVPDETYDALK
1615.8065	212-225	DTMVWPNGQWPAGR
1704.9390	143-157	GKLEEVENNLRSMGK
1755.0362	395-410	SYLDLMDKGTLEGLAK
1952.1254	25-41	DISTVPDETYDALKLDR
2117.3032	208-225	ESERDTMVWPNGQWPAGR
2256.5791	456-476	GNNPASLELKVLEMAENNLAK
2473.7657	226-247	PSHALDYTANIETTVWAAMPQR
2524.7515	355-376	WANYPFVPGIAENITSDWSEAR
2782.0441	353-376	TRWANYPFVPGIAENITSDWSEAR
2789.1657	432-455	TNRPNPPEPEKPGFGIFTQLFWSK
3319.8144	67-95	GTMGDYWEPIAISIYMDPNTFYKPPVSPK

Figure 2.15 Sequence coverage of fragments detected in proteolysis mass spectrometry of the HAO SDS-PAGE. The HAO (RefSeq protein accession number: NP_841349) sequence covered by the detected peptide fragments is underscored and highlighted in green. The predicted leader sequence is highlighted in red.

MRIGEWMRGL LLCAGLMMCG VVHADISTVP DETYDALKLD RGKATPKETY
EALVKRYKDP AHGAGKGTMG DYWEPIAISI YMDPNTFYKP PVSPKEVAER
KDCVECHSDE TPVWVRAWKR STHANLDKIR NLKSDDPLYY KKGKLEEVEN
NLRSMGKLGE KETLKEVGCI DCHVDVNKKD KADHTKDIRM PTADTCGTCH
LREFAERESE RDTMVWPNGQ WPAGRPSHAL DYTANIETTV WAAMPQREVA
EGCTMCHTNQ NKCDNCHTRH EFSAAESRKP EACATCHSGV DHNNWEAYTM
SKHGKLAEMN RDKWNWEVRL KDAFSKGGQN APTCAACHME YEGEYTHNIT
RKTRWANYPF VPGIAENITS DWSEARLDSW VLTCTQCHSE RFARSYLDLM
DKGTLEGLAK YQEANAIVHK MYEDGTLTGQ KTNRPNPPEP EKPGFGIFTQ
LFWSKGNNPA SLELKVLEMA ENNLAKMHVG LAHVNPGGWT YTEGWGPMNR
AYVEIQDEYT KMQELSALQA RVNKLEGKQT SLLDLKGTGE KISLGGLGGG
MLLAGALALI GWRKRKQTRA

2.2.3 Discussion

The HAO monomer derived from the 2.1 Å resolution $P2_12_12$ HAO crystal form (one trimer in the ASU) is very similar to the previously published $P6_3$ structural model to 2.8 Å resolution (two monomers in the ASU) (Figure 2.1 and 2.16) (*71*). A structural alignment of a single monomer from each of the two models results in a C_α root mean square deviation (r.m.s.d) of 0.41 Å. In the HAO model presented here, 502 residues

Figure 2.16 HAO – NE1300 model. The protein is shown as a cartoon. The HAO trimer is faded and colored by subunit (pale green, light blue and light pink), NE1300 is colored in red. Hemes are shown as stick colored by atom (carbon: *c*-type hemes, light gray; catalytic heme IV (heme P460), dark gray). Fe atoms of hemes are shown as spheres. Straight arrows indicate the position of the active site pocket in one of the three subunits. The cylinders colored by subunit represent the C-terminal putative transmembrane part that is absent from the HAO sample.

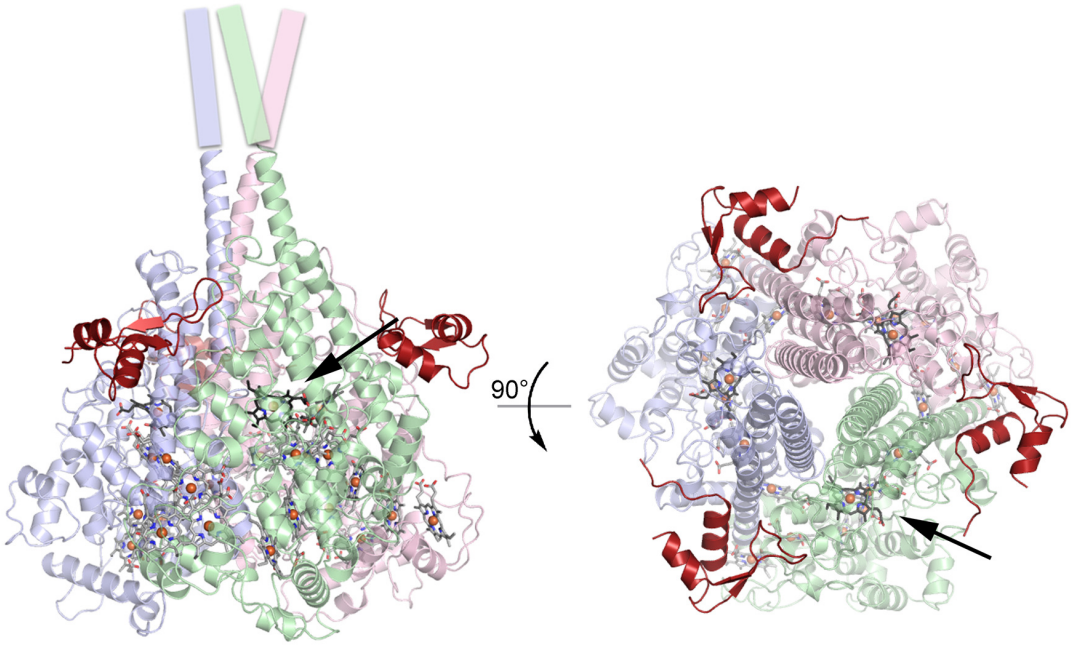

could be modeled into the electron density for each subunit in the trimer, only three more residues per monomer than in the model based on 2.8 Å resolution data. According to the open reading frame for the HAO gene, full length HAO should contain 546 residues. The lack of electron density for the missing C-terminal residues could be due to high mobility, as suggested by Tanaka and co-workers (*71*). However, it could also be due to a truncation of the HAO molecule, which is suggested by the limited space in the crystal packing C-terminal of the trimer. The latter is confirmed by the proteolysis / mass spectrometric analysis in this study. As the sample was treated with trypsin (primarily cleaving C-terminal of Lys and Arg), the truncation at Ser507 is not a product of trypsin proteolysis, and is therefore the likely C-terminus of the HAO polypeptide. Although the vast majority of HAO is present in a soluble form *in vivo*, under certain growth conditions (low Fe/low Cu) some HAO appears to be associated with the membrane (*105*). A transmembrane helix is predicted at residues 518-538 in the HAO sequence, which lies in the C-terminal part that is missing in the sample used in this study (Figure 2.17) (*88*). This suggests that HAO may be post-translationally cleaved *in vivo* to yield the soluble form. As pointed out in McTavish *et al.*, limiting metals during growth might restrict the maturation of HAO, and the membrane-bound form may actually represent incompletely processed enzyme (*105*).

Since the HAO sample used in this study was purified from source (i.e. not recombinant) the small protein that was identified as NE1300, is almost certainly an interaction partner to HAO *in vivo*. The binding between HAO and NE1300 must have a small K_d, as NE1300 remained bound throughout purification, and even to some extent in

Figure 2.17 Transmembrane prediction result. The hydrophobicity *vs.* residue plot indicates that a transmembrane section (residues 518-538) is present in HAO (Swiss-Prot accession number: Q50925). Prediction was done with TopPred at http://mobyle.pasteur.fr/cgi-bin/portal.py?form=toppred (*100, 101*).

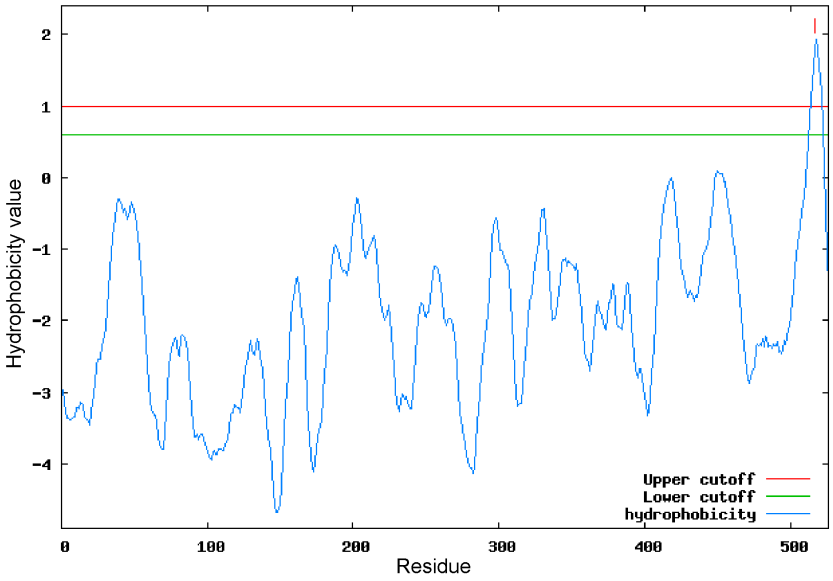

the SDS-PAGE gel-band of HAO. At present, the biological function of NE1300 is unknown. Homologs to NE1300 do exist in two other bacteria, which also belong to the *Nitrosomonas* genus (*N. eutropha* and *N. sp.*; 90 and 41% sequence identity, respectively). Unsurprisingly, the homologs are also classified as hypothetical proteins. The NE1300 gene is 400 kb away from the closest of the three *hao* gene clusters present in the *N. europaea* genome (*106, 107*). In the other two species, the NE1300 homologous genes are also distant from any *hao* gene cluster. In addition, the genes surrounding NE1300 in the three species do not have any obvious connection to ammonia oxidation and are different in each species. Interestingly, NE1300 lies adjacent to the electron acceptor protein in the proposed HAO – Cyt c_{554} complex model (*86*) (Figure

2.18). This observation invites the speculation that perhaps NE1300 is involved in recruiting Cyt c_{554} to HAO and stabilizing the electron transfer complex. Although not defined by the electron density map, the mass spectrometry shows that the HAO sample

Figure 2.18 HAO – Cyt c_{554} – NE1300 complex. Peptide is shown as surface. (A) HAO trimer is colored by subunit (pale green, light blue and light pink). Cyt c_{554} is colored in yellow and NE1300 in red. (B) Vacuum electrostatics with one of the three Cyt c_{554} molecules separated from the complex. The complex was generated based on illustrations in Iverson *et al.* (*55*) and Rosetta protein-protein docking server (http://rosettadock.graylab.jhu.edu/) results.

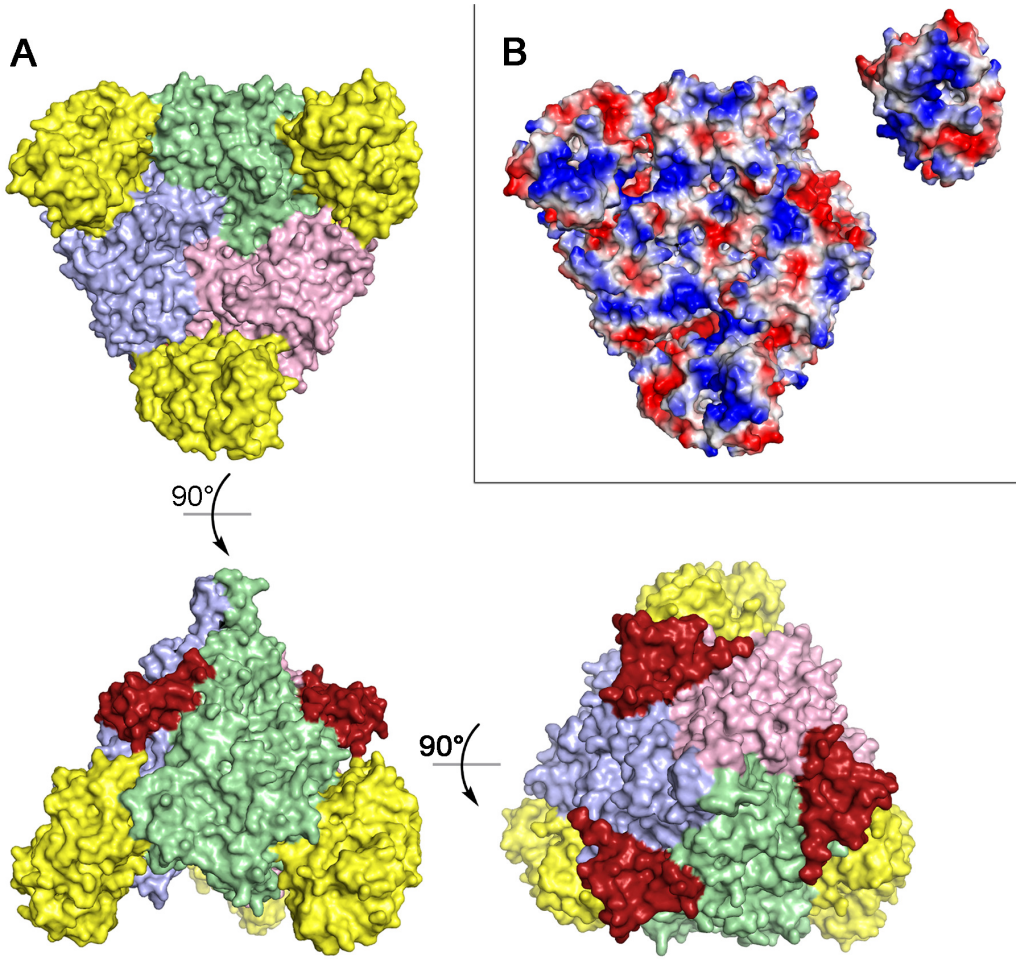

used for crystallization contained the mature full-length NE1300. The last ordered C-terminal residue in NE1300 is in close proximity to the modeled Cyt c_{554} and the 14 amino acids of NE1300 not defined by the electron density may be a key component in mediating the binding of Cyt c_{554} to HAO, becoming ordered only upon formation of the electron transfer complex.

The presented double crosslinked heme P460 model agrees with the mass spectrometry data that demonstrated the loss of two protons: one being the C3 proton of the Tyr467′ ring and the other being the Tyr467′ hydroxyl proton (*93*). This means that all four porhyrin *meso* carbons retain their proton upon crosslink formation, although the earlier NMR data indicated that only three porphyrin *meso* protons were present in the aromatic region of the spectra (*93*). This assignment assumed that the *meso* carbon remained part of an aromatic system, and so was referenced to NMR data obtained for phenylhydrazine treated porphyrin d_1 of *cytochrome* cd_1. In the reference system, a phenyl radical is formed that regiospecifically replaces the porphyrin-C5 proton, and thus the porphyrin-C5 remains sp^2 hybridized (*108*). As such, the additional complexity of C4 and C5 becoming sp^3 hybridized was not anticipated, and a fully characterized reference model was not available to help deconvolute the porphyrin proton chemical shifts. The Tyr hydroxyl proton undergoes solvent exchange, so no conclusion could be drawn about its presence/absence in the NMR study, complicating matters further. Therefore, it is not surprising that some misinterpretation of the NMR data occurred. In hindsight, this model of heme P460 in HAO was also supported in the earlier X-ray crystal structure, as the side chain oxygen of Tyr467' is only 1.5 Å and 2.1 Å away from C4 of the porphyrin

in the two NCS-related subunits (*71*). Furthermore, the porphyrin-C5 geometry is more compatible with sp^3, rather than the sp^2 hybridization required to satisfy the experimentally determined mass difference of the single crosslink model (Figure 2.8) (*93*).

The proximal ligand to the hemes P460 is His233, and the distal side is occupied by a water molecule (Figure 2.14). The Fe – His distance is unusually long, and refines to 2.5 Å in the three crystallographically independent active sites in the ASU. The Fe – O distance of the axial water refines to 2.3, 2.4 and 2.6 Å, respectively. Computational modeling suggests the probable formation of a bidentate hydrogen bond between the water molecule of the ferric aquo complex and the side chain of Asp267 in the active site pocket (*109*). The 2.1 Å electron density map, on the other hand, supports a monodentate interaction between the axial water molecule and Asp267 (Figure 2.14A). However, it should be noted that photo-induced reduction during X-ray diffraction data collection is a possibility and the crystal structure therefore might represent a non-physiological ferrous form of the enzyme**.**

Another protein found in *N. europaea* and other bacteria, cytochrome P460 (Cyt P460), also exhibits a ferrous optical absorption band at 460 nm (*110*). Cyt P460 is a *c*-type cytochrome unrelated to HAO with a predominantly β-sheet secondary structure (*104, 111, 112*). The protein exists as a homodimer in which each 19 kDa monomer contains a single heme that due to the ferrous absorption maxima was assumed to be similar to the catalytic heme in HAO. In *N. europaea* the heme of Cyt P460 indeed has a third crosslink to the protein. However, the crosslink is between the porphyrin-C15 to the

side-chain amine of a Lys residue (Figure 2.19) (*104, 113*). Expression of *N. europaea* Cyt P460 in *Pseudomonas aeruginosa* resulted in holo-Cyt P460 which closely resembled native Cyt P460, suggesting that the crosslink might form auto-catalytically (*114*). The physiological function of Cyt P460 has not been established although it has the ability to catalyze the oxidation of hydroxylamine (*115, 116*). Cyt P460 from *N. europaea* oxidizes hydroxylamine at a slower rate than HAO, but the enzyme from the obligate methylotroph *Methylococcus capsulatus* (Bath) has a turnover rate close to that of HAO (*116*). In methanotrophs, particulate methane monooxogenase (pMMO) produces significant amounts of hydroxylamine as a by-product due to its broad substrate specificity. Cyt P460 has been proposed to remove the resultant hydroxylamine that is toxic to the bacterium (*88*).

Figure 2.19 Drawing of heme P460 in Cyt P460.

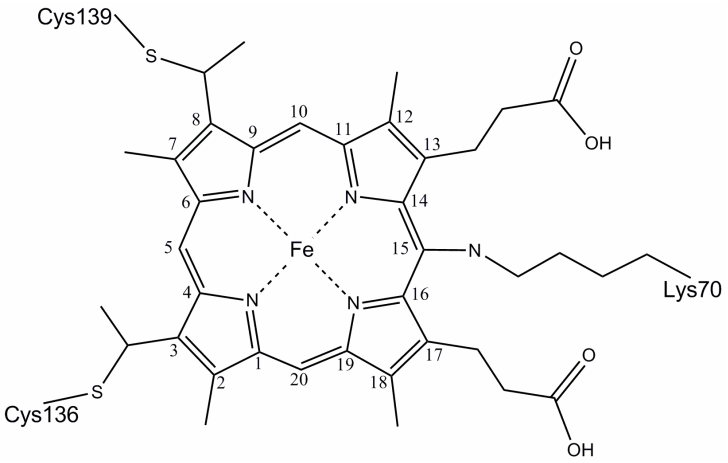

Figure 2.20 Proposed catalytic mechanism of HAO. Reprinted with permission from (*109*). Copyright © 2008, Elsevier.

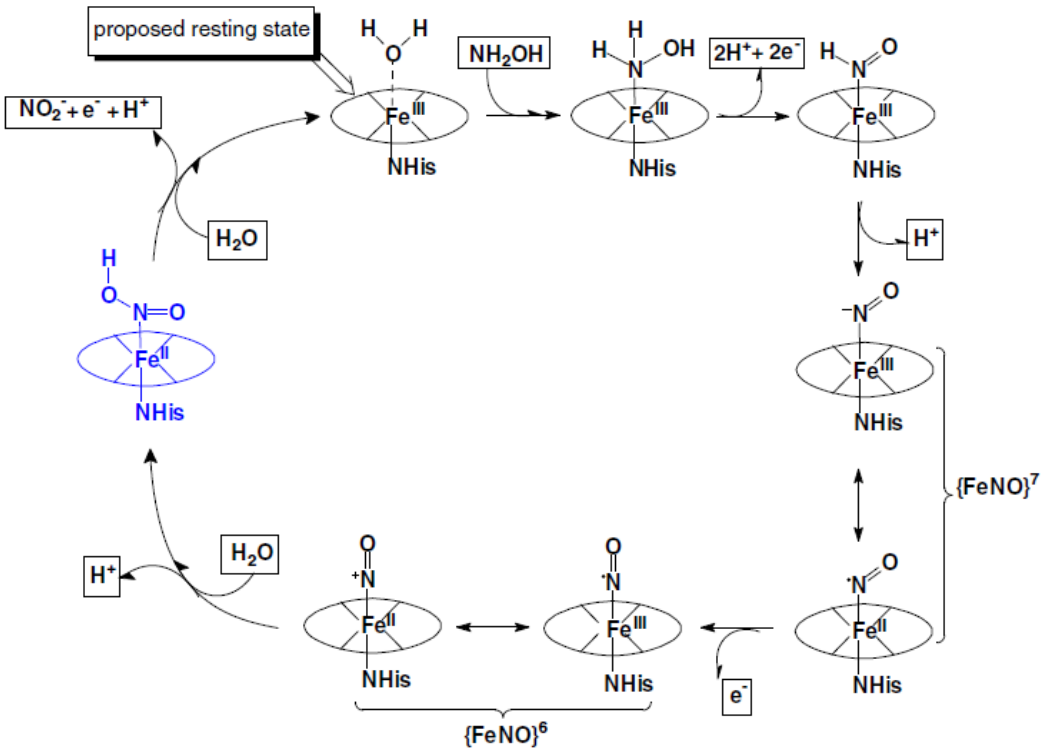

The extreme *ruffling* component of the HAO heme P460 (average 2.2 Å between the three hemes P460 in the ASU) has been suggested to be of catalytic importance in the reaction of hydroxylamine oxidation (*109*). In the proposed catalytic mechanism of HAO, the heme P460 bound water molecule is displaced upon substrate binding, yielding a Fe(III)-H_2NOH complex (Figure 2.20). A two electron oxidation accompanied by the removal of two protons results in a nitrosyl moiety (Fe(III)-HNO) that upon removal of another proton results in the $\{FeNO\}^7$ catalytic intermediate (Fe(III)-$^{-}$NO ↔ Fe(II)-$^{\bullet}$NO). Further oxidation by one electron produces the $\{FeNO\}^6$ intermediate (Fe(II)-$^{+}$NO ↔ Fe(III)-$^{\bullet}$NO) that is hydrolyzed by nucleophilic attack of a water molecule, yielding

nitrous acid (Fe(II)-NO_2H). The nitrous acid spontaneously deprotonates to form nitrite product (pKa = 3.4) following displacement from the iron by a water molecule to regenerate the resting state. Quantum mechanical calculations suggest that the *ruffling* stabilizes the proposed $\{FeNO\}^6$ catalytic intermediate, while destabilizing the preceding $\{FeNO\}^7$ intermediate enabling this unfavorable oxidation to occur at catalytic rates. It also was suggested that it increases the affinity of HAO for the hydroxylamine substrate. It is puzzling though that the *N. europaea* Cyt P460 crystallographic model shows a heme P460 with moderate distortion that can be decomposed into equal contributions from *saddling* and *ruffling* (0.8 Å) (*104*). However, dissolved Cyt P460 crystals revealed extensive oxidation and proteolysis of the protein. It is therefore possible that the native enzyme heme P460 adopts a different and possibly more ruffled conformation.

Mutation of the Lys involved in the crosslink in Cyt P460 to Ala, Arg, or a Tyr results in the loss of catalytic ability and altered ferrous optical absorption spectra (*114*). The mutant spectra closely resembled that of the related β-sheet cytochrome *c′* and the unrelated more widely distributed α-helical cytochrome *c′*. It was determined by MALDI-TOF that none of the mutations resulted in a crosslink to the heme. This suggests that the crosslink indeed is the reason for the 460 nm absorption maxima, and it also underscores the importance of the crosslink for hydroxylamine oxidation activity. The details of how the significantly different hemes P460 from Cyt P460 and HAO utilize the crosslink for hydroxylamine oxidation will have to await elucidation in future studies.

2.3 Structural analysis of hydroxylamine oxidoreductase reacted with hydroxylamine

The homotrimeric multi-heme enzyme hydroxylamine oxidoreductase (HAO) catalyzes the oxidation of hydroxylamine to nitrite. This reaction is a four-electron oxidation in which electrons are transferred from the active site heme P460 bound substrate, through a chain of *c*-type hemes, to the electron acceptor protein cytochrome c_{554}. The active site heme P460 is a *c*-type heme with an unprecedented double crosslink between the porphyrin and a Tyr from an adjacent subunit. The Tyr residue, along with an 'Asp-His' pair situated above the heme P460, are conserved among members of the HAO family. In the X-ray crystallographic model of HAO from *Nitrosomonas europaea*, there is also a second tyrosine present in the active site pocket that could be involved in catalysis. To investigate the possible roles these residues may play in stabilization of intermediates and identify potential proton acceptors, we have generated a crystal structure of *N. europaea* HAO treated with hydroxylamine substrate. The interaction of hydroxylamine with HAO *in crystallo* was confirmed by single crystal UV-visible microspectrophotometry.

2.3.1 Methods

Expression, purification and crystallization. The expression and purification of HAO from *Nitrosomonas europaea* was carried out as previously described (*96*). A brief description of the procedures can be found in Chapter 2.2.1. The protein was stored in -80°C for 17 years before being thawed and used for crystallization. The protein was buffer exchanged into 20 mM Hepes-Na pH 7.0 using an Amicon Ultra Centrifugal Device (Millipore) with a cut-off of 100 kDa. After buffer exchange the protein was concentrated to 15 mg/ml, as determined with Bradford reagent (Sigma). This sample was stored in -80°C for 6 months. The sample was concentrated to about 20 mg/ml before crystallization.

The HAO crystals were grown in 0.1 M potassium nitrate (KNO_3), 95 mM MES pH 7.5, 43% (v/v) PEG 400 and 5% (v/v) PEG 600 at 20°C in Microbatch 72 Well Plates (Hampton Research) with equal amounts (2 µl) of protein and crystallization cocktail under 10 µl of a 80/20 mixture of paraffin and immersion oil. A single crystal was soaked for 3.5 hours in crystallization solution with the addition of 20 mM hydroxylamine. A chemically reduced crystal was generated by soaking in crystallization solution with 2 mM of sodium dithionite for 2 min in N_2 atmosphere. The ferric HAO crystal was looped straight from the crystallization well. The crystals were flash frozen in liquid nitrogen, and no additional cryoprotectant was needed.

X-ray diffraction data collection and processing. X-ray diffraction data collection was carried out at the The National Institute of General Medical Sciences and National Cancer Institute Collaborative Access Team (GM/CA-CAT) beamline 23-ID-D at the Advanced Photon Source (APS), Argonne National Laboratory. 120 degrees of data were collected from a single crystal using a MAR 300 CCD detector. Data collection was done at cryogenic temperatures (100°K). The diffraction images were processed with HKL2000 (*51*).

Data analysis, model building and refinement. Initial phases were generated by difference Fourier using the previously determined $P2_12_12$ HAO – NE1300 model (PDB ID 4FAS) with all water molecules removed. Model building was done in Crystallographic Object-Oriented Toolkit (COOT) (*53*). The heme thioether links were restrained to 1.84 Å and the Tyr467′-C3 – porphyrin-C5 and Tyr467′-O – porphyrin-C4 links were restrained to 1.47 Å and 1.50 Å, respectively. The heme P460-Fe – N-hydroxylamine bond was restrained to 2.0 Å. Refinement was done with REFMAC (*59*) in the CCP4 suite using two TLS groups (*97, 98*). A random sample of 5% of the data across all resolution shells was chosen as an unbiased check to track refinement through calculation of an R_{free}. The remaining 95% of the reflections were used in refinement (R_{work}).

UV-visible microspectrophotometry. Single crystal spectra were collected on a microspectrophotometer from 4DX Systems AB, with a Zeiss CLX500 xenon lamp light

source, spectrograph (Thermo-Oriel) and a DV401A CCD detector (Andor Technology). The UV-visible absorption spectra were collected at the Kahlert Structural Biology Laboratory, University of Minnesota. An Oxford Instruments Cryojet was used to keep the crystals at 100°K. Solution spectra were collected using a Cary 50 UV-Visible spectrophotometer (Varian).

2.3.2 Results

The X-ray diffraction data were processed in the orthorhombic space group $P2_12_12$ with cell dimensions a = 141.0 Å, b = 142.5 Å , c = 107.7 Å. The resulting HAO – NE1300 peptide model is nearly identical to the previously generated 2.1 Å model, with a C_α r.m.s.d. of 0.130 Å between the two. The X-ray diffraction data processing and model refinement statistics are presented in Table 2.5. The 2Fo-Fc electron density map to 2.2 Å resolution clearly indicates the presence of a diatomic ligand in the distal binding site of the three NCS-related hemes P460 in the ASU (Figure 2.21). After modeling of all the other ligand atoms (i.e. water-, PEG- and MES-molecules), hydroxylamine was modeled into the electron density distal to the hemes P460. Based on the proposed substrate binding mode, the hydroxylamine was arranged with its nitrogen atom ligating to the heme P460 Fe atom (*109*). The Fe – N distance refined to 2.0 Å in all three monomers. The Fe – N – O angle refined to between 125-131degrees. The hydroxylamine is angled towards the side chain of His268 and the distance from the hydroxylamine-O – N_ε-His distance refines to 2.7-2.9 Å. One of the side chain oxygen atoms of Asp267 is 2.5-2.7 Å away from the oxygen atom of hydroxylamine. The distance between the hydroxylamine and the Tyr334-hydroxyl oxygen is 3.8-4.0 Å. Tyr334 is hydrogen bonding the oxygen atom of Asp267 that interacts with the substrate.

Single crystal UV-visible absorption in the 500-600 nm region showed that soaking the crystal in hydroxylamine solution generated a partially reduced HAO enzyme, consistent with HAO treated with hydroxylamine in solution (Figure 2.22)

(*117*). The UV-visible absorption spectrum of the crystal used for X-ray diffraction data collection showed that photo induced reduction had occurred. The spectrum resembled that of HAO crystals chemically reduced with sodium dithionite (Figure 2.22).

Table 2.5 X-ray data collection, processing and refinement statistics

Data collection and processing statistics	
unique reflections	113599
redundancy [a]	4.8
resolution (Å) [a]	50.0-2.20 (2.24-2.20)
completeness (%) [a]	99.8 (99.9)
R_{merge} (%) [a, b]	10.9 (63.7)
I/σI [a]	14.9 (2.8)
space group	$P2_12_12$
Refinement and model building statistics	
resolution (Å) [a]	107.65-2.16 (2.22-2.16)
no. of reflections in working set [a]	107775 (5688)
no. of reflections in test set [a]	5743 (298)
R_{work} (%) [c]	15.0
R_{work} (%) [d]	19.4
ESU (Å) R_{work}/R_{free}	
no. protein atoms	13136
no. ligand atoms	1235
no. water molecules	677
RMS	
bond length (Å)	0.021
bond angle (deg.)	2.249
Ramachandran plot (%)	
favored	96.7
allowed	3.2
disallowed	0.1
average B-factor (Å^2)	
protein	27.1
ligands	34.1
waters	42.3
overall	28.4

[a] Values in parentheses correspond to the highest resolution shell.

[b] $R_{merge} = \Sigma_{hkl}\Sigma^{N}_{j=1}|I_{hkl}-I_{hkl}(j)|/\Sigma_{hkl}N*I_{hkl}$, sum over all reflections and all observations N, with $I_{hkl}(j)$ intensity of the j^{th} observation of reflection hkl and I_{hkl} mean intensity of the reflection hkl.

[c] $R_{work} = \Sigma||F_o| - |F_c||/ \Sigma|F_o|$, where $|F_o|$ = observed structure factor amplitude and $|F_c|$ = calculated structure factor amplitude.

[d] R_{free}, R-factor based on 5% of the data excluded from refinement.

Figure 2.21 Hydroxylamine bound to heme P460. View of one of the three active sites in the ASU in two different orientations (A) and (B). Side chains and hemes are shown in stick colored by atom with carbon colored by subunit (pale green and light blue). Fe atoms are displayed as brown spheres and water molecules as red spheres. Protein is shown as cartoon. 2Fo-Fc electron density (contoured at 1σ) is shown as blue mesh. Dashed lines illustrate the interactions mentioned in the text.

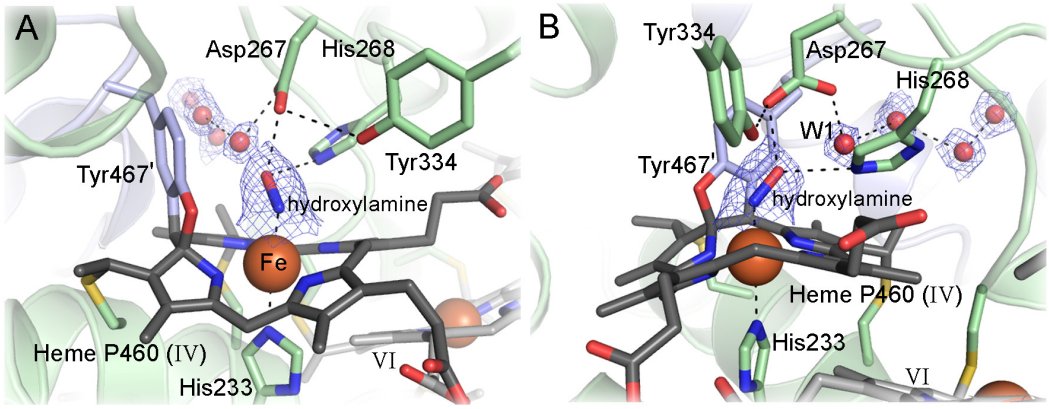

Figure 2.22 UV-visible absorption spectra of HAO: in ferric form, red trace; hydroxylamine treated, blue trace and dithionite reduced, black trace. The inset on the left is a zoomed-in view of the 480-600 nm region. The inset on the right shows single crystal UV-visible spectra of HAO crystals in: ferric form, red trace; hydroxylamine reduced no X-ray radiation exposure, blue trace and post X-ray data collection, black trace.

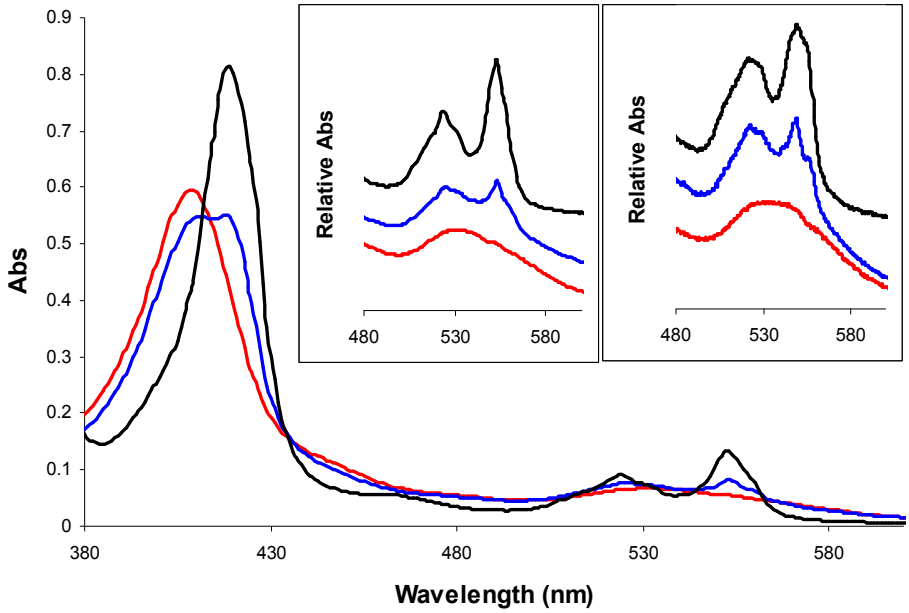

2.3.3 Discussion

The crystal structure model of HAO in complex with hydroxylamine indicates that both residues of the 'Asp-His' pair are involved in substrate interactions. In the catalytic mechanism proposed for HAO, the hydroxylamine substrate first loses two protons and two electrons yielding a Fe(III) – HN=O species (Figure 2.20) (*109*). It is unclear what facilitates the loss of the two protons from the iron bound nitrogen during turnover, as there are no specific interactions between the protein and this atom. Based on the structural model, the base that accepts the hydroxyl proton is most likely the N_ε of His268. The N_δ of His268 appears to form a hydrogen bond with the carbonyl oxygen of Ser264, making the N_ε of His268 more receptive to protonation. The Asp267 side chain oxygen atom that is not hydrogen bonded to the hydroxylamine oxygen atom is positioned only ~3 Å away from the N_ε of His268, perpendicular to the imidazole plane. The negatively charged Asp267 side chain can therefore aid in stabilizing the positively charged imidazolium ion upon proton abstraction from the substrate hydroxyl.

A water molecule (W1) is situated within hydrogen bonding distance to both the Asp267 oxygen atom and the N_ε of His268 (Figure 2.21). The water molecule is closest to the active site in a chain of hydrogen bonded water molecules that stretches from the solvent accessible inner cavity of the HAO trimer. This water chain could function as a 'proton wire', enabling deprotonation of His268 later in the HAO catalytic cycle to regenerate the base for another round of catalysis.

In the structural model, Tyr334 is outside hydrogen bonding distance of the

hydroxylamine molecule, and is therefore probably not instrumental in substrate coordination. The Tyr334 is not conserved among the members of the HAO family. However, a protein blast search suggests that the position of Tyr334 is occupied by either an Asn or a Glu. Since these residues also are capable of hydrogen bonding to a water molecule, the function of this residue might be to poise a water molecule for nucleophilic attack on the heme bound nitrosyl intermediate to generate nitrite (the final step in the proposed HAO catalyzed reaction (Figure 2.20) (*109*)).

2.4 Future directions

A recombinant expression system for HAO would advance mechanistic studies significantly. Heterologous expression would address whether the heme P460 crosslink is formed autocatalytically, and enable mutation of Tyr467' involved in the heme P460 crosslink. Mutation of Asp267, His268 and Tyr334 would test the catalytic roles of these amino acids during HAO turnover.

Many gram-negative facultative or strictly anaerobic bacteria have the ability to respire on insoluble Fe(III)- and Mn(III/IV)-(hydr)oxides (*118*). To exploit these abundant electron sinks, electron transfer must occur from the quinone/quinol pool within the cytoplasmic membrane across the outer membrane to the extracellular insoluble Fe/Mn-(hydr)oxides. Some bacteria accomplish this by utilizing a network of multi-heme cytochromes. DNA sequencing of bacterial genomes has revealed that metal-reducing bacteria, such as *Shewanella oneidensis*, contain numerous *c*-type cytochromes (as defined by the number of *c*-type heme attachment motifs within the genome) (*119*). *S. oneidensis* is predicted to contain no less than 39 genes that code for *c*-type cytochromes, 14 of which contain 4 or more heme groups (*120*). In *S. oneidensis* the electron transfer mechanism involves proteins coded by the *mtrABCDEF-omcA* gene cluster (*118, 121*). MtrD, MtrE and MtrF are homologs of MtrA, MtrB and MtrC, respectively. The OmcA protein is a homolog of MtrC and MtrF. It is proposed that the decaheme protein MtrA in complex with the β-barrel porin MtrB form an electron transport complex that can transfer electrons across the outer membrane to MtrC (*122*). The decaheme protein MtrC

is suggested to be the extracellular terminus for this complex. The recent crystal structure of MtrF provided molecular insight into how reduction of insoluble minerals may occur *via* direct transfer of electrons to insoluble mineral substrates, indirect electron transfer mediated by flavin electron shuttles, and/or cytochrome redox partners, either singularly or in tandem, through binding to different sites on the MtrF molecular surface (*123*). In a study exploring the function of the possible combinations of Mtr proteins, different strains of *S. oneidensis* were created in which *mtr* paralogs and other genes had been eliminated from the genome (*121*). Restoration of function was tested in these mutant strains by recombinant expression of the different *mtr* genes. In this study, the broad host L-arabinose inducible vector pBBad22K was used (*124*). The proven concept of recombinant expression of such complex decaheme heme proteins should make the *S. oneidensis* – pBBad22K system a suitable vehicle for recombinant HAO expression. I have begun to test whether this is a viable option.

Since heme proteins need to be translocated into the periplasm, an unaltered leader sequence containing the signal peptide is desirable. Unfortunately the pBBad22K vector is designed such that a restriction-site downstream of the Shine-Dalgarno sequence contains the ATG start codon (*Nco*I, CCATGG) (Figure 2.23). Unless the second codon in the leader sequence starts with a G (compatible only with amino acids Val, Ala, Asp, Glu or Gly) a mutation of the G to the desired nucleotide has to be done after vector – gene ligation. This was achieved with the QuikChange® Site-Directed Mutagenesis Kit (Stratagene).

Figure 2.23 Multiple cloning site of the L-arabinose inducible broad host pBBad22K vector. Reprinted with permission from Sukchawalit, R. *et al. (124)*. Copyright © 2006, John Wiley and Sons.

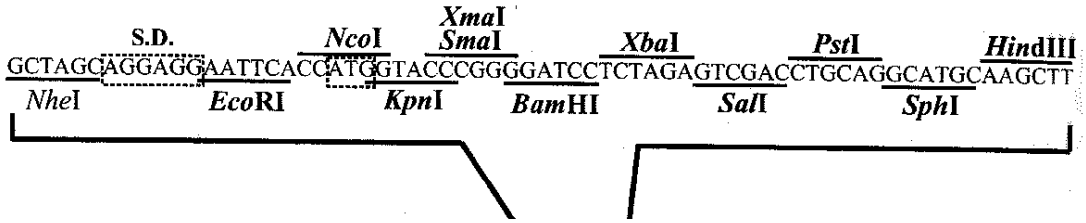

Three HAO – pBBad22K constructs have been made and one of these has been tested for expression. The HAO gene was amplified from *N. europaea* genomic DNA, with upstream primer 5' G AAG ATC TCC ATG GTA ATG AGA ATA GGG GAG TGG ATG 3' and downstream primer 5' TAA CCC GGG TCA AGC TCG GGT CTG C 3'. It should be pointed out that the upstream primer was designed differently from the strategy described above. Here two random bases were introduced (to keep the gene in-frame) followed by the HAO gene *including* the ATG site. After restriction digest with *Bgl*II (AGATCT) and *Xma*I (CCCGGG) this PCR product was ligated into p3xFLAG-CMV-7.1 vector (Sigma). The reason for going into p3xFLAG-CMV-7.1 was that the HAO gene contains an internal *Nco*I restriction site. Therefore, the HAO – p3XFLAG-CMV-7.1 construct was subjected to site-directed mutagenesis, in which the internal restriction site …ACC ATG GTC… was mutated to …ACT ATG GTC… (ACC and ACT both code for Thr). The HAO gene was subcloned into pBBad22K from HAO – p3XFLAG-CMV-7.1 using *Nco*I and *Xma*I. This construct was tested for HAO expression in wild type *S. oneidensis* and the Δ*mtrC*/Δ*omcA*/Δ*mtrF*/Δ*mtrA* /Δ*mtrD*/Δ*dmsE*/Δ*SO4360*/Δ*cctA* strain (both kindly provided by Dr. Jeffrey A. Gralnick

at the University of Minnesota), but no HAO expression was detected. The idea for using the deletion strain was that removal of endogenous *c*-type cytochromes would allow for more efficient processing of the overexpressed HAO polypeptide. Since no HAO expression was detected, the ATGGAT segment that alters the leader sequence (…CC ATG GAT ATG AGA…) was deleted from the plasmid using PCR. Using PCR, a stop codon was introduced into this construct at the equivalent position of amino acid 508. These constructs (unaltered leader sequence with full length and introduced stop codon) awaits expression trials in the two strains of *S. oneidensis*.

There is, however, the possibility that *S. oneidensis* does not recognize the leader sequence associated with the native *N. europaea hao* gene. Therefore, two other constructs (full length and introduced stop codon) are currently being made, where the *N. europaea* leader sequence is replaced with that of the endogenous *mtrA* leader sequence.

One way to test the hypothesis that NE1300 is involved in the interaction between HAO and Cyt c_{554} is to investigate the binding affinity of Cyt c_{554} to HAO with and without NE1300 by isothermal titration calorimetry (ITC) or differential scanning calorimetry (DSC). As NE1300 has remained bound to HAO following purification from the host organism and long-term storage, the binding affinity between the two proteins must be high. Therefore, removing NE1300 from the purified HAO might be hard to accomplish. Furthermore, the small size of NE1300 compared to HAO makes it difficult to effectively separate unbound HAO from HAO bound to 1, 2 or 3 NE1300, and thus it is impossible to know if a sample of HAO is truly free of NE1300 for experimental studies. Besides the possibility of conducting mutation studies on key amino acids, a

recombinant expression system would also allow the production of a NE1300-free HAO sample that could be used for ITC or DSC studies.

Another way to probe the effects of NE1300 is to produce a *N. europaea* NE1300 knockout strain and characterize the phenotype (unless NE1300 is vital for growth). If the Δ*ne1300* strain is viable, this would also be a source of HAO sample free of NE1300. A strategy for creating a knockout strain of *nirK* in *N. europaea* using the suicide vector pRVS3 has been reported by van Spanning and co-workers (*125*). Production of HAO in the absence of NE1300 would additionally address whether this small hypothetical protein is involved in HAO maturation and heme P460 generation.

References cited

1. Ragsdale, S. W. (2009) "Nickel-based enzyme systems", *J.Biol. Chem. 284*, 18571-18575.
2. Thauer, R. K. (1998) "Biochemistry of methanogenesis: a tribute to Marjory Stephenson", *Microbiology 144*, 2377-2406.
3. Thauer, R. K., and Shima, S. (2008) "Methane as fuel for anaerobic microorganisms", *Ann. N.Y. Acad. Sci. 1125*, 158-170.
4. Ellermann, J., Hedderich, R., Bocher, R., and Thauer, R. K. (1988) "The final step in methane formation. Investigations with highly purified methyl-CoM reductase (component C) from *Methanobacterium thermoautotrophicum* (strain Marburg)", *Eur. J. Biochem. 172*, 669-677.
5. Ellefson, W. L., and Wolfe, R. S. (1981) "Component C of the methylreductase system of *Methanobacterium*", *J. Biol. Chem. 256*, 4259-4262.
6. Ermler, U., Grabarse, W., Shima, S., Goubeaud, M., and Thauer, R. K. (1997) "Crystal structure of methyl-coenzyme M reductase: the key enzyme of biological methane formation", *Science 278*, 1457-1462.
7. Grabarse, W., Mahlert, F., Duin, E. C., Goubeaud, M., Shima, S., Thauer, R. K., Lamzin, V., and Ermler, U. (2001) "On the mechanism of biological methane formation: structural evidence for conformational changes in methyl-coenzyme M reductase upon substrate binding", *J. Mol. Biol. 309*, 315-330.
8. Grabarse, W., Mahlert, F., Shima, S., Thauer, R. K., and Ermler, U. (2000) "Comparison of three methyl-coenzyme M reductases from phylogenetically distant organisms: unusual amino acid modification, conservation and adaptation", *J. Mol. Biol. 303*, 329-344.
9. Horng, Y. C., Becker, D. F., and Ragsdale, S. W. (2001) "Mechanistic studies of methane biogenesis by methyl-coenzyme M reductase: evidence that coenzyme B participates in cleaving the C-S bond of methyl-coenzyme M", *Biochemistry 40*, 12875-12885.
10. Selmer, T., Kahnt, J., Goubeaud, M., Shima, S., Grabarse, W., Ermler, U., and Thauer, R. K. (2000) "The biosynthesis of methylated amino acids in the active site region of methyl-coenzyme M reductase", *J. Biol. Chem. 275*, 3755-3760.
11. Diekert, G., Gilles, H. H., Jaenchen, R., and Thauer, R. K. (1980) "Incorporation of 8 succinate per mol nickel into factors F_{430} by *Methanobacterium thermoautotrophicum*", *Arch. Microbiol. 128*, 256-262.
12. Diekert, G., Jaenchen, R., and Thauer, R. K. (1980) "Biosynthetic evidence for a nickel tetrapyrrole structure of factor F_{430} from *Methanobacterium thermoautotrophicum*", *FEBS Lett. 119*, 118-120.
13. Whitman, W. B., and Wolfe, R. S. (1980) "Presence of nickel in Factor F_{430} from *Methanobacterium bryantii*", *Biochem. Biophys. Res. Commun. 92*, 1196-1201.
14. Albracht, S. P. J., Ankel-Fuchs, D., Böcher, R., Ellermann, J., Moll, J., van der Zwann, J. W., and Thauer, R. K. (1988) "Five new EPR signals assigned to nickel in methyl-coenzyme M reductase from *Methanobacterium thermoautotrophicum*, strain Marburg", *Biochim. Biophys. Acta, 955*, 86-102.

15. Dey, M., Kunz, R. C., Lyons, D. M., and Ragsdale, S. W. (2007) "Characterization of alkyl-nickel adducts generated by reaction of methyl-coenzyme M reductase with brominated acids", *Biochemistry 46*, 11969-11978.
16. Dey, M., Telser, J., Kunz, R. C., Lees, N. S., Ragsdale, S. W., and Hoffman, B. M. (2007) "Biochemical and spectroscopic studies of the electronic structure and reactivity of a methyl-Ni species formed on methyl-coenzyme M reductase", *J. Am. Chem. Soc. 129*, 11030-11032.
17. Duin, E. C., Cosper, N. J., Mahlert, F., Thauer, R. K., and Scott, R. A. (2003) "Coordination and geometry of the nickel atom in active methyl-coenzyme M reductase from *Methanothermobacter marburgensis* as detected by X-ray absorption spectroscopy", *J. Biol. Inorg. Chem. 8*, 141-148.
18. Duin, E. C., Signor, L., Piskorski, R., Mahlert, F., Clay, M. D., Goenrich, M., Thauer, R. K., Jaun, B., and Johnson, M. K. (2004) "Spectroscopic investigation of the nickel-containing porphinoid cofactor F_{430}. Comparison of the free cofactor in the +1, +2 and +3 oxidation states with the cofactor bound to methyl-coenzyme M reductase in the silent, red and ox forms", *J. Biol. Inorg. Chem. 9*, 563-576.
19. Finazzo, C., Harmer, J., Bauer, C., Jaun, B., Duin, E. C., Mahlert, F., Goenrich, M., Thauer, R. K., Van Doorslaer, S., and Schweiger, A. (2003) "Coenzyme B induced coordination of coenzyme M via its thiol group to Ni(I) of F_{430} in active methyl-coenzyme M reductase", *J. Am. Chem. Soc. 125*, 4988-4989.
20. Finazzo, C., Harmer, J., Jaun, B., Duin, E. C., Mahlert, F., Thauer, R. K., Van Doorslaer, S., and Schweiger, A. (2003) "Characterization of the MCR_{red2} form of methyl-coenzyme M reductase: a pulse EPR and ENDOR study", *J. Biol. Inorg. Chem. 8*, 586-593.
21. Goubeaud, M., Schreiner, G., and Thauer, R. K. (1997) "Purified methyl-coenzyme-M reductase is activated when the enzyme-bound coenzyme F430 is reduced to the nickel(I) oxidation state by titanium(III) citrate", *Eur. J. Biochem. 243*, 110-114.
22. Harmer, J., Finazzo, C., Piskorski, R., Bauer, C., Jaun, B., Duin, E. C., Goenrich, M., Thauer, R. K., Van Doorslaer, S., and Schweiger, A. (2005) "Spin density and coenzyme M coordination geometry of the ox1 form of methyl-coenzyme M reductase: a pulse EPR study", *J. Am. Chem. Soc. 127*, 17744-17755.
23. Harmer, J., Finazzo, C., Piskorski, R., Ebner, S., Duin, E. C., Goenrich, M., Thauer, R. K., Reiher, M., Schweiger, A., Hinderberger, D., and Jaun, B. (2008) "A nickel hydride complex in the active site of methyl-coenzyme m reductase: implications for the catalytic cycle", *J. Am. Chem. Soc. 130*, 10907-10920.
24. Hinderberger, D., Ebner, S., Mayr, S., Jaun, B., Reiher, M., Goenrich, M., Thauer, R. K., and Harmer, J. (2008) "Coordination and binding geometry of methyl-coenzyme M in the red1m state of methyl-coenzyme M reductase", *J. Biol. Inorg. Chem. 13*, 1275-1289.
25. Kunz, R. C., Horng, Y. C., and Ragsdale, S. W. (2006) "Spectroscopic and kinetic studies of the reaction of bromopropanesulfonate with methyl-coenzyme M reductase", *J. Biol. Chem. 281*, 34663-34676.

26. Mahlert, F., Bauer, C., Jaun, B., Thauer, R. K., and Duin, E. C. (2002) "The nickel enzyme methyl-coenzyme M reductase from methanogenic archaea: In vitro induction of the nickel-based MCR-ox EPR signals from MCR-red2", *J. Biol. Inorg. Chem. 7*, 500-513.
27. Rospert, S., Voges, M., Berkessel, A., Albracht, S. P., and Thauer, R. K. (1992) "Substrate-analogue-induced changes in the nickel-EPR spectrum of active methyl-coenzyme-M reductase from *Methanobacterium thermoautotrophicum*", *Eur. J. Biochem. 210*, 101-107.
28. Sarangi, R., Dey, M., and Ragsdale, S. W. (2009) "Geometric and electronic structures of the Ni(I) and methyl-Ni(III) intermediates of methyl-coenzyme M reductase", *Biochemistry 48*, 3146-3156.
29. Tang, Q., Carrington, P. E., Horng, Y. C., Maroney, M. J., Ragsdale, S. W., and Bocian, D. F. (2002) "X-ray absorption and resonance Raman studies of methyl-coenzyme M reductase indicating that ligand exchange and macrocycle reduction accompany reductive activation", *J. Am. Chem. Soc. 124*, 13242-13256.
30. Telser, J., Davydov, R., Horng, Y. C., Ragsdale, S. W., and Hoffman, B. M. (2001) "Cryoreduction of methyl-coenzyme M reductase: EPR characterization of forms, MCR(ox1) and MCR(red1)", *J. Am. Chem. Soc. 123*, 5853-5860.
31. Yang, N., Reiher, M., Wang, M., Harmer, J., and Duin, E. C. (2007) "Formation of a nickel-methyl species in methyl-coenzyme M reductase, an enzyme catalyzing methane formation", *J. Am. Chem. Soc. 129*, 11028-11029.
32. Albracht, S. P. J., Ankelfuchs, D., van der Zwaan, J. W., Fontijn, R. D., and Thauer, R. K. (1986) "A new electron paramagnetic resonance signal of nickel in *Methanobacterium thermoautotrophicum*", *Biochim. Biophys. Acta 870*, 50-57.
33. Telser, J., Horng, Y. C., Becker, D. F., Hoffman, B. M., and Ragsdale, S. W. (2000) "On the assignment of nickel oxidation states of the ox1, ox2 forms of methyl-coenzyme M reductase", *J. Am. Chem. Soc. 122*, 182-183.
34. Hinderberger, D., Piskorski, R. R., Goenrich, M., Thauer, R. K., Schweiger, A., Harmer, J., and Jaun, B. (2006) "A nickel-alkyl bond in an inactivated state of the enzyme catalyzing methane formation", *Angew. Chem. Int. Ed. 45*, 3602-3607.
35. Kern, D. I., Goenrich, M., Jaun, B., Thauer, R. K., Harmer, J., and Hinderberger, D. (2007) "Two sub-states of the red2 state of methyl-coenzyme M reductase revealed by high-field EPR spectroscopy", *J. Biol. Inorg. Chem. 12*, 1097-1105.
36. Becker, D. F., and Ragsdale, S. W. (1998) "Activation of methyl-SCoM reductase to high specific activity after treatment of whole cells with sodium sulfide", *Biochemistry 37*, 2639-2647.
37. Berkessel, A. (1991) "Methyl-coenzyme M reductase - model studies on pentadentate nickel-complexes and a hypothetical mechanism", *Bioorg. Chem. 19*, 101-115.
38. Jaun, B. (1990) "Coenzyme-F430 from methanogenic bacteria - oxidation of F430 pentamethyl ester to the Ni(III) form", *Helv. Chim. Acta 73*, 2209-2217.
39. Signor, L., Knuppe, C., Hug, R., Schweizer, B., Pfaltz, A., and Jaun, B. (2000) "Methane formation by reaction of a methyl thioether with a photo-excited nickel

thiolate - a process mimicking methanogenesis in archaea", *Chem. Eur. J. 6*, 3508-3516.
40. Chen, S. L., Pelmenschikov, V., Blomberg, M. R., and Siegbahn, P. E. (2009) "Is there a Ni-methyl intermediate in the mechanism of methyl-coenzyme M reductase?", *J. Am. Chem. Soc. 131*, 9912-9913.
41. Pelmenschikov, V., Blomberg, M. R. A., Siegbahn, P. E. M., and Crabtree, R. H. (2002) "A mechanism from quantum chemical studies for methane formation in methanogenesis", *J. Am. Chem. Soc. 124*, 4039-4049.
42. Pelmenschikov, V., and Siegbahn, P. E. (2003) "Catalysis by methyl-coenzyme M reductase: a theoretical study for heterodisulfide product formation", *J. Biol. Inorg. Chem. 8*, 653-662.
43. Duin, E. C., and McKee, M. L. (2008) "A new mechanism for methane production from methyl-coenzyme M reductase as derived from density functional calculations", *J. Phys. Chem. B 112*, 2466-2482.
44. Bobik, T. A., and Wolfe, R. S. (1988) "Physiological importance of the heterodisulfide of coenzyme M and 7-mercaptoheptanoylthreonine phosphate in the reduction of carbon dioxide to methane in *Methanobacterium*", *Proc. Natl. Acad. Sci. U.S.A. 85*, 60-63.
45. Goenrich, M., Duin, E. C., Mahlert, F., and Thauer, R. K. (2005) "Temperature dependence of methyl-coenzyme M reductase activity and of the formation of the methyl-coenzyme M reductase red2 state induced by coenzyme B", *J. Biol. Inorg. Chem. 10*, 333-342.
46. Kunz, R. C., Dey, M., and Ragsdale, S. W. (2008) "Characterization of the thioether product formed from the thiolytic cleavage of the alkyl-nickel bond in methyl-Coenzyme M reductase", *Biochemistry 47*, 2661-2667.
47. Noll, K. M., Donnelly, M. I., and Wolfe, R. S. (1987) "Synthesis of 7-mercaptoheptanoylthreonine phosphate and its activity in the methylcoenzyme M methylreductase system", *J. Boil. Chem. 262*, 513-515.
48. Olson, K. D., McMahon, C. W., and Wolfe, R. S. (1991) "Photoactivation of the 2-(methylthio)ethanesulfonic acid reductase from *Methanobacterium*", *Proc. Natl. Acad. Sci. U.S.A. 88*, 4099-4103.
49. Zehnder, A. J., and Wuhrmann, K. (1976) "Titanium (III) citrate as a nontoxic oxidation-reduction buffering system for the culture of obligate anaerobes", *Science 194*, 1165-1166.
50. Gunsalus, R. P., Romesser, J. A., and Wolfe, R. S. (1978) "Preparation of coenzyme M analogues and their activity in the methyl coenzyme M reductase system of *Methanobacterium thermoautotrophicum*", *Biochemistry 17*, 2374-2377.
51. Otwinowski, Z., Minor, W. (1997) "Processing of X-ray Diffraction Data Collected in Oscillation Mode", *Methods Enzymol.: Macromol. Crystallogr., part A 276*, 307-326.
52. (1994) "The CCP4 suite: programs for protein crystallography", *Acta Crystallogr., Sect. D: Biol. Crystallogr. 50*, 760-763.

53. Emsley, P., and Cowtan, K. (2004) “Coot: model-building tools for molecular graphics”, *Acta Crystallogr., Sect. D: Biol. Crystallogr. 60*, 2126-2132.
54. Wilmot, C. M., Sjogren, T., Carlsson, G. H., Berglund, G. I., and Hajdu, J. (2002) “Defining redox state of X-ray crystal structures by single-crystal ultraviolet-visible microspectrophotometry”, *Methods Enzymol. 353*, 301-318.
55. Cedervall, P. E., Dey, M., Pearson, A. R., Ragsdale, S. W., and Wilmot, C. M. (2010) “Structural Insight into methyl-Coenzyme M reductase chemistry using coenzyme B analogues”, *Biochemistry 49*, 7683-7693.
56. Schlichting, I., Berendzen, J., Chu, K., Stock, A. M., Maves, S. A., Benson, D. E., Sweet, R. M., Ringe, D., Petsko, G. A., and Sligar, S. G. (2000) “The catalytic pathway of cytochrome P450cam at atomic resolution”, *Science 287*, 1615-1622.
57. Dey, M., Li, X., Kunz, R. C., and Ragsdale, S. W. (2010) “Detection of organometallic and radical intermediates in the catalytic mechanism of methyl-coenzyme M reductase using the natural substrate methyl-coenzyme M and a coenzyme B substrate analogue”, *Biochemistry 49*, 10902-10911.
58. Goenrich, M., Mahlert, F., Duin, E. C., Bauer, C., Jaun, B., and Thauer, R. K. (2004) “Probing the reactivity of Ni in the active site of methyl-coenzyme M reductase with substrate analogues”, *J. Biol. Inorg. Chem. 9*, 691-705.
59. Murshudov, G. N., Vagin, A. A., and Dodson, E. J. (1997) “Refinement of macromolecular structures by the maximum-likelihood method”, *Acta Crystallogr., Sect. D: Biol. Crystallogr. 53*, 240-255.
60. DeLano, W. L. (2002) “The PyMOL Molecular Graphics System”, San Carlos, CA, U.S.A.
61. Paithankar, K. S., Owen, R. L., and Garman, E. F. (2009) “Absorbed dose calculations for macromolecular crystals: improvements to RADDOSE”, *J. Synchrotron Radiat. 16*, 152-162.
62. Hallam, S. J., Girguis, P. R., Preston, C. M., Richardson, P. M., and DeLong, E. F. (2003) “Identification of methyl coenzyme M reductase A (mcrA) genes associated with methane-oxidizing archaea”, *Appl. Environ. Microbiol. 69*, 5483-5491.
63. Scheller, S., Goenrich, M., Boecher, R., Thauer, R. K., and Jaun, B. (2010) “The key nickel enzyme of methanogenesis catalyses the anaerobic oxidation of methane”, *Nature 465*, 606-608.
64. Ebner, S., Jaun, B., Goenrich, M., Thauer, R. K., and Harmer, J. (2010) “Binding of coenzyme B induces a major conformational change in the active site of methyl-coenzyme M reductase”, *J. Am. Chem. Soc. 132*, 567-575.
65. Govindjee (2005) “*Advances in photosynthesis and respiration*”, Vol. 16, Springer, Dordrecht, the Netherlands.
66. Jetten, M. S., Niftrik, L. V., Strous, M., Kartal, B., Keltjens, J. T., and Op den Camp, H. J. (2009) “Biochemistry and molecular biology of anammox bacteria”, *Crit. Rev. Biochem. Mol. Biol.*, 1-20.
67. Kartal, B., Maalcke, W. J., de Almeida, N. M., Cirpus, I., Gloerich, J., Geerts, W., Op den Camp, H. J., Harhangi, H. R., Janssen-Megens, E. M., Francoijs, K. J.,

Stunnenberg, H. G., Keltjens, J. T., Jetten, M. S., and Strous, M. "Molecular mechanism of anaerobic ammonium oxidation", *Nature 479*, 127-130.
68. Andersson, K. K., Lipscomb, J. D., Valentine, M., Munck, E., and Hooper, A. B. (1986) "Tetraheme cytochrome *c*-554 from *Nitrosomonas europaea*. Heme-heme interactions and ligand binding", *J. Biol. Chem. 261*, 1126-1138.
69. Yamanaka, T., and Shinra, M. (1974) "Cytochrome *c*-552 and cytochrome *c*-554 derived from *Nitrosomonas europaea*. Purification, properties, and their function in hydroxylamine oxidation", *J. Biochem. 75*, 1265-1273.
70. Kowalchuk, G. A., and Stephen, J. R. (2001) "Ammonia-oxidizing bacteria: a model for molecular microbial ecology", *Annu. Rev. Microbiol. 55*, 485-529.
71. Igarashi, N., Moriyama, H., Fujiwara, T., Fukumori, Y., and Tanaka, N. (1997) "The 2.8 Å structure of hydroxylamine oxidoreductase from a nitrifying chemoautotrophic bacterium, *Nitrosomonas europaea*", *Nat. Struct. Biol. 4*, 276-284.
72. Bowman, S. E., and Bren, K. L. (2008) "The chemistry and biochemistry of heme *c*: functional bases for covalent attachment", *Nat. Prod. Rep. 25*, 1118-1130.
73. Bertini, I., Gray, H. B., Stiefel, E. I., and Valentine, J. S. (2007) "*Biological Inorganic Chemistry: Structure and Reactivity*", University Science Books, Sausalito, U.S.A.
74. Moss, G. P. (1988) "Nomenclature of tetrapyrroles. Recommendations 1986 IUPAC-IUB Joint Commission on Biochemical Nomenclature (JCBN)", *Eur. J. Biochem. 178*, 277-328.
75. Mowat, C. G., Rothery, E., Miles, C. S., McIver, L., Doherty, M. K., Drewette, K., Taylor, P., Walkinshaw, M. D., Chapman, S. K., and Reid, G. A. (2004) "Octaheme tetrathionate reductase is a respiratory enzyme with novel heme ligation", *Nat. Struct. Mol. Biol. 11*, 1023-1024.
76. Einsle, O., Messerschmidt, A., Stach, P., Bourenkov, G. P., Bartunik, H. D., Huber, R., and Kroneck, P. M. (1999) "Structure of cytochrome *c* nitrite reductase", *Nature 400*, 476-480.
77. Aragao, D., Frazao, C., Sieker, L., Sheldrick, G. M., LeGall, J., and Carrondo, M. A. (2003) "Structure of dimeric cytochrome c_3 from *Desulfovibrio gigas* at 1.2 Å resolution", *Acta Crystallogr., Sect. D: Biol. Crystallogr. 59*, 644-653.
78. Hartshorne, R. S., Kern, M., Meyer, B., Clarke, T. A., Karas, M., Richardson, D. J., and Simon, J. (2007) "A dedicated haem lyase is required for the maturation of a novel bacterial cytochrome *c* with unconventional covalent haem binding", *Mol. Microbiol. 64*, 1049-1060.
79. Allen, J. W., Daltrop, O., Stevens, J. M., and Ferguson, S. J. (2003) "*C*-type cytochromes: diverse structures and biogenesis systems pose evolutionary problems", *Philos. Trans. R. Soc. Lond. B. Biol. Sci. 358*, 255-266.
80. Stevens, J. M., Daltrop, O., Allen, J. W., and Ferguson, S. J. (2004) "*C*-type cytochrome formation: chemical and biological enigmas", *Acc. Chem. Res. 37*, 999-1007.

81. Jentzen, W., Ma, J. G., and Shelnutt, J. A. (1998) "Conservation of the conformation of the porphyrin macrocycle in hemoproteins", *Biophys. J. 74*, 753-763.
82. Jentzen, W., Song, X. Z., and Shelnutt, J. A. (1997) "Structural characterization of synthetic and protein-bound porphyrins in terms of the lowest-frequency normal coordinates of the macrocycle", *J. Phys. Chem. B 101*, 1684-1699.
83. Wood, P. M. (1983) "Why do c-type cytochromes exist?", *FEBS Lett. 164*, 223-226.
84. Hooper, A. B., Tran, V. M., and Balny, C. (1984) "Kinetics of reduction by substrate or dithionite and heme-heme electron transfer in the multiheme hydroxylamine oxidoreductase", *Eur. J. Biochem. 141*, 565-571.
85. Iverson, T. M., Arciero, D. M., Hooper, A. B., and Rees, D. C. (2001) "High-resolution structures of the oxidized and reduced states of cytochrome *c*554 from *Nitrosomonas europaea*", *J. Biol. Inorg. Chem. 6*, 390-397.
86. Iverson, T. M., Arciero, D. M., Hsu, B. T., Logan, M. S., Hooper, A. B., and Rees, D. C. (1998) "Heme packing motifs revealed by the crystal structure of the tetra-heme cytochrome c554 from *Nitrosomonas europaea*", *Nat. Struct. Biol 5*, 1005-1012.
87. Bergmann, D. J., Hooper, A. B., and Klotz, M. G. (2005) "Structure and sequence conservation of *hao* cluster genes of autotrophic ammonia-oxidizing bacteria: evidence for their evolutionary history", *Appl. Env. Microbiol. 71*, 5371-5382.
88. Klotz, M. G., Schmid, M. C., Strous, M., op den Camp, H. J., Jetten, M. S., and Hooper, A. B. (2008) "Evolution of an octahaem cytochrome *c* protein family that is key to aerobic and anaerobic ammonia oxidation by bacteria", *Env. Microbiol. 10*, 3150-3163.
89. Simon, J. (2002) "Enzymology and bioenergetics of respiratory nitrite ammonification", *FEMS Microbiol. Rev. 26*, 285-309.
90. Clarke, T. A., Cole, J. A., Richardson, D. J., and Hemmings, A. M. (2007) "The crystal structure of the pentahaem *c*-type cytochrome NrfB and characterization of its solution-state interaction with the pentahaem nitrite reductase NrfA", *Biochem. J. 406*, 19-30.
91. Clarke, T. A., Dennison, V., Seward, H. E., Burlat, B., Cole, J. A., Hemmings, A. M., and Richardson, D. J. (2004) "Purification and spectropotentiometric characterization of *Escherichia coli* NrfB, a decaheme homodimer that transfers electrons to the decaheme periplasmic nitrite reductase complex", *J. Biol. Chem. 279*, 41333-41339.
92. Rodrigues, M. L., Oliveira, T. F., Pereira, I. A., and Archer, M. (2006) "X-ray structure of the membrane-bound cytochrome *c* quinol dehydrogenase NrfH reveals novel haem coordination", *EMBO J. 25*, 5951-5960.
93. Arciero, D. M., Hooper, A. B., Cai, M., and Timkovich, R. (1993) "Evidence for the structure of the active site heme P460 in hydroxylamine oxidoreductase of *Nitrosomonas*", *Biochemistry 32*, 9370-9378.
94. Andersson, K. K., Babcock, G. T., and Hooper, A. B. (1991) "P460 of hydroxylamine oxidoreductase of *Nitrosomonas europaea*: Soret resonance

Raman evidence for a novel heme-like structure", *Biochem. Biophys. Res. Commun. 174*, 358-363.
95. Andersson, K. K., Kent, T. A., Lipscomb, J. D., Hooper, A. B., and Munck, E. (1984) "Mössbauer, EPR, and optical studies of the P-460 center of hydroxylamine oxidoreductase from *Nitrosomonas*. A ferrous heme with an unusually large quadrupole splitting", *J. Biol. Chem. 259*, 6833-6840.
96. Arciero, D. M., Balny, C., and Hooper, A. B. (1991) "Spectroscopic and rapid kinetic studies of reduction of cytochrome *c*554 by hydroxylamine oxidoreductase from *Nitrosomonas europaea*", *Biochemistry 30*, 11466-11472.
97. Collaborative Computational Project, number 4 (1994) "The CCP4 suite: programs for protein crystallography", *Acta Crystallogr., Sect. D: Biol. Crystallogr. 50*, 760-763.
98. Winn, M. D., Isupov, M. N., and Murshudov, G. N. (2001) "Use of TLS parameters to model anisotropic displacements in macromolecular refinement", *Acta Crystallogr., Sect. D: Biol. Crystallogr. 57*, 122-133.
99. Tina, K. G., Bhadra, R., and Srinivasan, N. (2007) "PIC: Protein Interactions Calculator", *Nucleic Acids Res. 35*, W473-476.
100. Claros, M. G., and von Heijne, G. (1994) "TopPred II: an improved software for membrane protein structure predictions", *Comput. Appl. Biosci. 10*, 685-686.
101. von Heijne, G. (1992) "Membrane protein structure prediction. Hydrophobicity analysis and the positive-inside rule", *J. Mol. Biol. 225*, 487-494.
102. French, S., and Wilson, K. S. (1978) "On the treatment of negative intensity observations", *Acta Cryst. Sect. A 34*, 517–525.
103. Matthews, B. W. (1968) "Solvent content of protein crystals", *J. Mol. Biol. 33*, 491-497.
104. Pearson, A. R., Elmore, B. O., Yang, C., Ferrara, J. D., Hooper, A. B., and Wilmot, C. M. (2007) "The crystal structure of cytochrome P460 of *Nitrosomonas europaea* reveals a novel cytochrome fold and heme-protein cross-link", *Biochemistry 46*, 8340-8349.
105. McTavish, H., Arciero, D. M., and Hooper, A. B. (1995) "Interaction with membranes of cytochrome *c*554 from *Nitrosomonas europaea*", *Arch. Biochem. Biophys. 324*, 53-58.
106. Chain, P., Lamerdin, J., Larimer, F., Regala, W., Lao, V., Land, M., Hauser, L., Hooper, A., Klotz, M., Norton, J., Sayavedra-Soto, L., Arciero, D., Hommes, N., Whittaker, M., and Arp, D. (2003) "Complete genome sequence of the ammonia-oxidizing bacterium and obligate chemolithoautotroph *Nitrosomonas europaea*", *J. Bact. 185*, 2759-2773.
107. McTavish, H., LaQuier, F., Arciero, D., Logan, M., Mundfrom, G., Fuchs, J. A., and Hooper, A. B. (1993) "Multiple copies of genes coding for electron transport proteins in the bacterium *Nitrosomonas europaea*", *J. Bact. 175*, 2445-2447.
108. Yap-Bondoc, F., and Timkovich, R. (1990) "Inactivation of cytochrome cd_1 by hydrazines", *J. Biol. Chem. 265*, 4247-4253.

109. Fernandez, M. L., Estrin, D. A., and Bari, S. E. (2008) "Theoretical insight into the hydroxylamine oxidoreductase mechanism", *J. Inorg. Biochem. 102*, 1523-1530.
110. Erickson, R. H., and Hooper, A. B. (1972) "Preliminary characterization of a variant co-binding heme protein from *Nitrosomonas*", *Biochim. Biophys. Acta 275*, 231-244.
111. Bergmann, D. J., and Hooper, A. B. (1994) "The primary structure of cytochrome P460 of *Nitrosomonas europaea*: presence of a *c*-heme binding motif", *FEBS Lett. 353*, 324-326.
112. Bergmann, D. J., Zahn, J. A., Hooper, A. B., and DiSpirito, A. A. (1998) "Cytochrome P460 genes from the methanotroph *Methylococcus capsulatus* Bath", *J. Bact. 180*, 6440-6445.
113. Arciero, D. M., and Hooper, A. B. (1997) "Evidence for a crosslink between *c*-heme and a lysine residue in cytochrome P460 of *Nitrosomonas europaea*", *FEBS Lett. 410*, 457-460.
114. Bergmann, D. J., and Hooper, A. B. (2003) "Cytochrome P460 of *Nitrosomonas europaea*. Formation of the heme-lysine cross-link in a heterologous host and mutagenic conversion to a non-cross-linked cytochrome *c*"', *Eur. J. Biochem. 270*, 1935-1941.
115. Numata, M., Saito, T., Yamazaki, T., Fukumori, Y., and Yamanaka, T. (1990) "Cytochrome P-460 of *Nitrosomonas europaea*: further purification and further characterization", *J. Biochem. 108*, 1016-1021.
116. Zahn, J. A., Duncan, C., and DiSpirito, A. A. (1994) "Oxidation of hydroxylamine by cytochrome P-460 of the obligate methylotroph *Methylococcus capsulatus* Bath", *J. Bact. 176*, 5879-5887.
117. Hooper, A. B., and Terry, K. R. (1977) "Hydroxylamine oxidoreductase from *Nitrosomonas*: inactivation by hydrogen peroxide", *Biochemistry 16*, 455-459.
118. Shi, L., Squier, T. C., Zachara, J. M., and Fredrickson, J. K. (2007) "Respiration of metal (hydr)oxides by *Shewanella* and *Geobacter*: a key role for multihaem *c*-type cytochromes", *Mol. Microbiol. 65*, 12-20.
119. Heidelberg, J. F., Paulsen, I. T., Nelson, K. E., Gaidos, E. J., Nelson, W. C., Read, T. D., Eisen, J. A., Seshadri, R., Ward, N., Methe, B., Clayton, R. A., Meyer, T., Tsapin, A., Scott, J., Beanan, M., Brinkac, L., Daugherty, S., DeBoy, R. T., Dodson, R. J., Durkin, A. S., Haft, D. H., Kolonay, J. F., Madupu, R., Peterson, J. D., Umayam, L. A., White, O., Wolf, A. M., Vamathevan, J., Weidman, J., Impraim, M., Lee, K., Berry, K., Lee, C., Mueller, J., Khouri, H., Gill, J., Utterback, T. R., McDonald, L. A., Feldblyum, T. V., Smith, H. O., Venter, J. C., Nealson, K. H., and Fraser, C. M. (2002) "Genome sequence of the dissimilatory metal ion-reducing bacterium *Shewanella oneidensis*", *Nat. Biotechnol. 20*, 1118-1123.
120. Mowat, C. G., and Chapman, S. K. (2005) "Multi-heme cytochromes-new structures, new chemistry", *Dalton Trans.*, 3381-3389.

121. Coursolle, D., and Gralnick, J. A. “Reconstruction of extracellular respiratory pathways for iron(III) reduction in *Shewanella Oneidensis* strain MR-1”, *Front. Microbiol. 3*, 56.
122. Hartshorne, R. S., Reardon, C. L., Ross, D., Nuester, J., Clarke, T. A., Gates, A. J., Mills, P. C., Fredrickson, J. K., Zachara, J. M., Shi, L., Beliaev, A. S., Marshall, M. J., Tien, M., Brantley, S., Butt, J. N., and Richardson, D. J. (2009) “Characterization of an electron conduit between bacteria and the extracellular environment”, *Proc. Natl. Acad. Sci. U.S.A. 106*, 22169-22174.
123. Clarke, T. A., Edwards, M. J., Gates, A. J., Hall, A., White, G. F., Bradley, J., Reardon, C. L., Shi, L., Beliaev, A. S., Marshall, M. J., Wang, Z., Watmough, N. J., Fredrickson, J. K., Zachara, J. M., Butt, J. N., and Richardson, D. J. “Structure of a bacterial cell surface decaheme electron conduit”, *Proc. Natl. Acad. Sci. U.S.A. 108*, 9384-9389.
124. Sukchawalit, R., Vattanaviboon, P., Sallabhan, R., and Mongkolsuk, S. (1999) “Construction and characterization of regulated L-arabinose-inducible broad host range expression vectors in *Xanthomonas*”, *FEMS Microbiol. Lett. 181*, 217-223.
125. Beaumont, H. J., Hommes, N. G., Sayavedra-Soto, L. A., Arp, D. J., Arciero, D. M., Hooper, A. B., Westerhoff, H. V., and van Spanning, R. J. (2002) “Nitrite reductase of *Nitrosomonas europaea* is not essential for production of gaseous nitrogen oxides and confers tolerance to nitrite”, *J. Bact. 184*, 2557-2560.